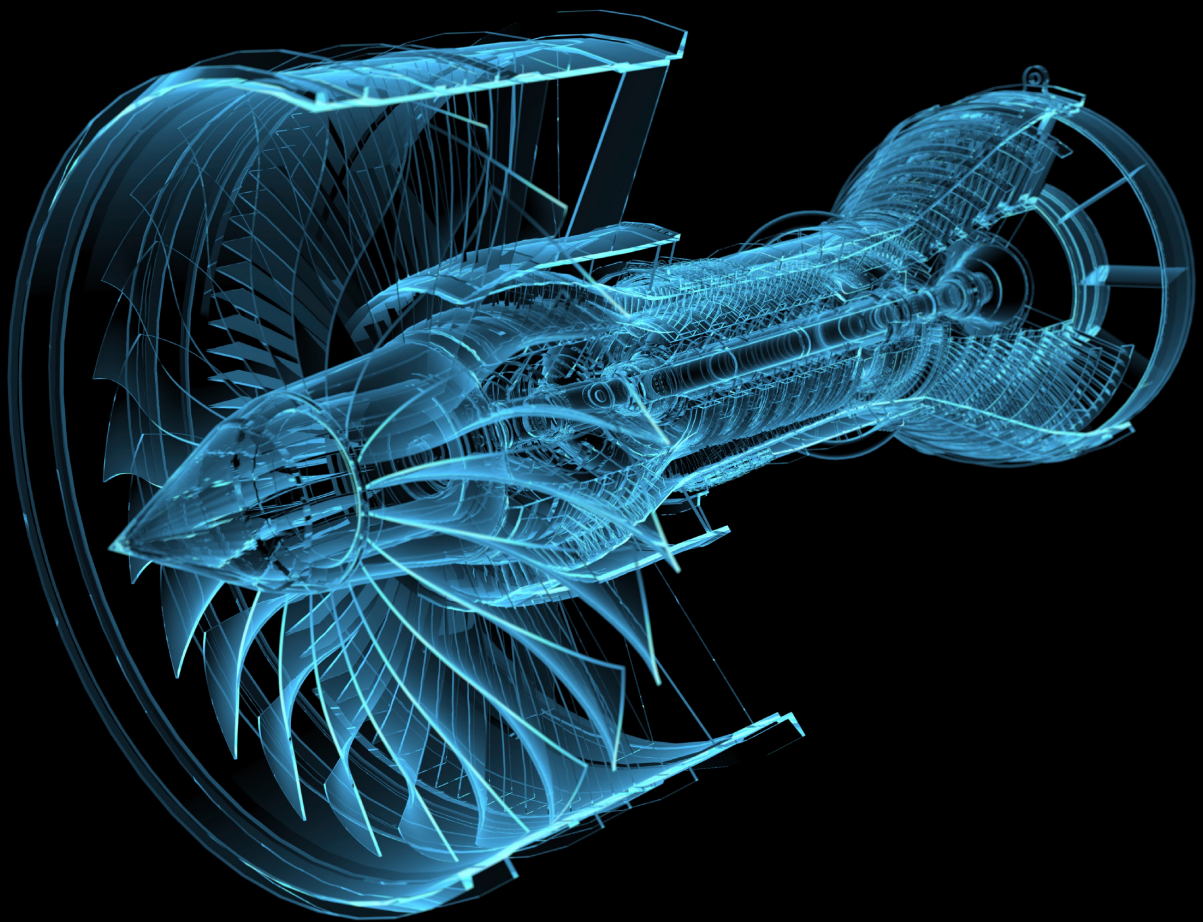


On the Conceptual Engine Design and Sizing Tool

MSc Thesis

J.C. Tiemstra

Technische Universiteit Delft



On the Conceptual Engine Design and Sizing Tool

MSc Thesis

by

J.C. Tiemstra

in partial fulfillment of the requirements for the degree of

Master of Science
in Aerospace Engineering

at the Delft University of Technology,
to be defended publicly on Friday February 2, 2017 at 2:00 PM.

Student number: 4012569
Project duration: September 15, 2015 – February 3, 2016
Supervisor: Dr. A. G. Rao
Thesis committee: Dr. A. G. Rao, TU Delft (FPP),
Dr. ir. C. Lettieri, TU Delft (FPP),
Dr. R. Pecnik, TU Delft (3ME)

An electronic version of this thesis is available at <http://repository.tudelft.nl/>.

Extensive summary

Air travel has been an advancing branch in the transportation market and has proven to be resilient to external financial shocks over the years. A recent market study by Airbus showed that the aviation market has been steadily growing at an approximate rate of 5% each year for the past two decades. It is expected that this growth will be sustained for at least another 20 years. Consequently, the Advisory Council for Aeronautics Research in Europe (ACARE) presented a report on the environmental impact of the aviation industry and concluded that large improvements are needed with respect to reducing emissions from the aviation industry in order to comply with international standards. ACARE has set several (non-binding) goals for the years 2020 and 2050, which will be primarily focussed on the reduction of three types of aircraft emissions: noise production, CO_2 emissions, and NO_x , CO & UHC emissions. These goals are referred to as “extremely challenging” by ACARE, requiring revolutionary change in the aviation industry.

Incorporating the environmental aspect has increased the complexity of the engine design process, while performance targets are evermore demanding. The envisioned improvements proposed by ACARE require fast paced advancements in engine technology that reach beyond the capabilities of current engine design methods. Therefore, new methods that allow for quick investigation of engine conceptual designs are needed. Current design tools usually focus on optimizing the aerothermodynamic performance of the engine, while another important factor for aircraft propulsion systems, the engine weight, is often not integrated into this design process. It is important to already make accurate weight estimates of engine components in the conceptual design phase, as inaccuracies may lead to compulsory design changes in later design phases. Weight estimations early on in the design cycle of the engine may result in an overall more fuel efficient engine design and thus help reaching the goals set by ACARE.

The engine conceptual design and sizing tool developed in this thesis focuses on the fan stage and low pressure compressor of a twin-spool high-bypass ratio turbofan engine. The tool will be used to determine the effect of increasing the fan tip diameter on the aerodynamic performance, its total weight and the noise production of the engine. Three separate modules are designed for this purpose. An aerodynamic module is used for the aero- and thermodynamic design and analysis of the components. In the module, the fan stage is designed using a Blade-Element Method (BEM), while a mean-line design is chosen for the design of the low pressure compressor. Secondly, a weight estimation module is integrated that focusses on the structural design of all components, including component fatigue behaviour, and determines the weight of each component. Finally, a noise prediction module is used to determine the noise spectrum of the engine. According to the International Civil Aviation Organization (ICAO) regulations, the noise performance of the engine is determined as measured by an observer on the ground using a fly-over simulation. All modules are first validated using available engine data from a General Electric CF6-80C2/B6F engine, after which the research question is answered.

Since only the low pressure compressor components are considered in this research, further investigation is needed to integrate other engine components in the design cycle and arrive at a full-scale conceptual engine design and sizing tool.

Acknowledgements

Over the past few months I received help and support from many people, and all of them have contributed to where I am today. I must say that the journey has been more intense than I suspected, and it is the people that were there for me repeatedly along the road that I want to address here with a special word of thanks.

First I would like to thank my thesis advisor and daily supervisor, Dr. Arvind Gangoli Rao, for creating the opportunity to undertake this project with him. During the Master's programme, Arvind has raised my interest for the field of aeroengine propulsion by his passionate lecturing on engine related topics. Working together on this project has been a very positive experience for me and I want to thank him for his positive attitude, everlasting patience and valuable advice throughout the project. I appreciate it how I was consistently allowed to let this thesis be my own work, with you steering me in the right direction whenever necessary.

I would also like to thank all people that helped me with the validation survey of this thesis project. Without their passionate participation and hospitality of receiving me on-site, this validation survey could not have been conducted. Unfortunately I cannot mention any names as the source of the data has to remain anonymous, but their help is really appreciated.

Furthermore, I want to thank my friends for their emotional support in the process of making this thesis. I want to thank my girlfriend Amaya for all her love and support these past few months. Also my friends, with whom I shared good times and somehow made this long project feel like passed in no-time.

Last but not least, I would like to thank my family for their loving support throughout the whole process. A special word of thanks goes out to my parents, who have always been there for me, who always trusted in me and had no doubt I would succeed even in times when I was going through moral slumps. Their motivational words have always kept me on track and helped me to put things in perspective.

Contents

List of Figures	iii
List of Tables	v
1 Introduction	1
1.1 Problem statement	1
1.2 Thesis objective	2
1.3 Report outline	4
2 General Considerations	5
2.1 Turbofan configuration & lay-out	5
2.1.1 Spool configurations	5
2.1.2 Compressor types	6
2.1.3 Flow mixing configurations	6
2.1.4 Chosen configuration	6
2.2 Turbofan components	6
2.3 Design Point	8
2.4 Modules	8
2.4.1 Aerothermodynamic performance	9
2.4.2 Weight estimation	9
2.4.3 Noise prediction	10
2.5 Validation	11
3 Aerodynamics	13
3.1 Governing equations and assumptions	13
3.2 Non-dimensional performance parameters	14
3.3 Gas path analysis	16
3.3.1 Design methods	16
3.3.2 Annulus geometry	16
3.3.3 Cascade design	17
3.3.4 Velocity triangles	18
3.3.5 Vortex design	18
3.3.6 Incidence angle	20
3.3.7 Deviation angle	21
3.3.8 Loss sources	22
3.4 Fan Analysis & Design	23
3.4.1 Design methodology	23
3.4.2 Inlet calculations	25
3.4.3 Pressure losses	28
3.5 LPC analysis & design	30
3.5.1 Design methodology	30
3.5.2 Inlet calculations	31
3.5.3 Pressure losses	32
4 Structural analysis & Weight	37
4.1 Materials	37
4.2 Fatigue life	38
4.2.1 Design methodology	38
4.2.2 Estimated stress-life	40

4.3	Blades	42
4.4	Disks	44
4.5	Casing	46
4.5.1	Pressure containment	46
4.5.2	Blade containment	47
4.6	Shaft.	47
4.7	Spinner cone	47
5	Noise Estimation	49
5.1	Noise prediction methods	49
5.2	Heidmann's method	49
5.2.1	Broadband noise	50
5.2.2	Discrete tone noise	51
5.2.3	Combination tone noise	51
5.3	Improved Heidmann's method	51
5.4	ESDU method	52
5.5	Take-off simulation	52
5.6	Noise descriptors	53
6	Module validation	55
6.1	Aerodynamic module	55
6.2	Structural analysis & weight estimation module	60
6.3	Noise module	62
7	Results & Conclusions	67
7.1	Effect of increasing fan tip diameter	67
7.2	Effect of spool speed	68
8	Recommendations	73
8.1	Aerodynamics module	73
8.2	Structural & analysis module	73
8.3	Noise module	74
A	Loss coefficient correlations	75
	Bibliography	77

List of Figures

1.1	Main goals for reduction in emissions as set by ACARE for the years 2020 and 2050 as compared to the capabilities of a typical new aircraft from the year 2000.	2
1.2	Schematic CO_2 emissions reduction roadmap. <i>Source:[1]</i>	3
2.1	CF6-80C2 Sectional Drawing. <i>Source: [2]</i>	7
2.2	Typical mission profile for civil aircraft. <i>Source: [3]</i>	8
2.3	Engine weight component break-down.	10
2.4	Comparison of noise sources and magnitudes for low- and high-BPR turbofan engines. <i>Source: [4]</i>	10
2.5	CF6-80C2 engine. <i>Source: GE Aviation</i>	11
2.6	CFM56-7B engine. <i>Source: CFM International</i>	11
3.1	Flowpath geometry designs.	17
3.2	Three popular compressor cascades.	18
3.3	Fan blade angle nomenclature. <i>Source: [5]</i>	19
3.4	Velocity triangle nomenclature. <i>Source: [5]</i>	19
3.5	Optimum incidence angle and stall boundaries on the cascade loss curve. <i>Source: [6]</i>	20
3.6	Comparison of rotor incidence angle prediction methods using NASA rotor data (table 3.4).	21
3.7	Comparison of stator incidence angle prediction methods using NASA rotor data (table 3.4).	21
3.8	Comparison of rotor deviation angle prediction methods using NASA rotor data (table 3.4).	22
3.9	Comparison of stator deviation angle prediction methods using NASA rotor data (table 3.4).	22
3.10	Iterative solving method for blade angles.	22
3.11	Development of tip, hub and endwall vortices in fan rotor and stator blade channels. <i>Source: [7]</i>	23
3.12	Flow fields in a compressor cascade with loss sources indicated. <i>Source: [8]</i>	23
3.13	Fan stage. <i>Source: GrabCAD</i>	24
3.14	Fan design	26
3.15	Iterative solving method for fan rotor design.	27
3.16	Iterative solving method for inlet axial velocity, C_{ax}	28
3.17	Low pressure compressor stage. <i>Source: GrabCAD</i>	30
3.18	Low pressure compressor design map.	31
3.19	Inlet specific flow vs. Mach number with typical LPC inlet conditions indicated.	32
4.1	Temperature effect on yield and ultimate strength.	38
4.2	Stress amplitude ratio.	39
4.3	Fatigue safety margin methods.	39
4.4	Modified S-N curves for steel component. <i>Source: [9]</i>	40
4.5	S-N data curve fitting vs. fatigue life estimation	42
4.6	Blade build up. <i>Source: [10]</i>	43
4.7	Rotating disk stress analysis. <i>Source: [11]</i>	44
5.1	Rotor-stator interaction discrete tone harmonic levels and fundamental tone level cut-off. <i>Source: [5]</i>	51
5.2	Take-off procedure. <i>Source: [5]</i>	53
5.3	Lateral noise measurement location. <i>Source: [5]</i>	53

5.4	Distance history for 767-300ER take-off procedure.	53
5.5	Angle history for 767-300ER take-off procedure.	53
6.1	Optimized fan results for CFM56-7B engine at take-off design point.	56
6.2	Optimized fan blade shape of a CFM56-7B engine at take-off design point, with section cuts along the streamline at hub, splitter and tip radii.	57
6.3	Optimized fan results for CFM56-7B engine at take-off design point, with alternative DeHaller design limit of 0.6.	58
6.4	Optimized fan blade shape of a CFM56-7B engine at take-off design point, with alternative DeHaller design limit of $DH \geq 0.6$. Section cuts shown along the streamline at hub, splitter, and tip radii, and horizontal projected section cut at the splitter.	59
6.5	CFM56-7B fan blade validation section at approximately one-third of blade height.	59
6.6	Fan rotor blade off-design performance with design point indicated.	60
6.7	Disk stress analysis validation using T-AXI Disk	61
6.8	Disk stress analysis validation using T-AXI Disk	61
6.9	CFM56-7 Sectional drawing overlay. <i>Source: [12]</i>	62
6.10	CFM56-7 LPC components exported to 3D output.	63
6.11	Fan inlet and exhaust noise spectral comparison of different noise prediction methods for a range of directivity angles measured from engine inlet axis at a 150 ft (45.27 m) radius.	64
6.12	Take-off fly-over simulation vs. certified engine data. <i>Source: [13]</i>	66
6.13	Take-off lateral simulation vs. certified engine data. <i>Source: [13]</i>	66
7.1	Rotor adiabatic performance	67
7.2	Relative total engine weight	67
7.3	Tip diameter effect on the fly-over lateral measurement EPNL.	68
7.4	Tip diameter effect on the fly-over longitudinal measurement EPNL.	68
7.5	The effect of spool speed on the bypass and core adiabatic efficiency η_{ad} for a range of bypass ratios.	69
7.6	Effect of spool speed on total mass m_{tot} for a range of bypass ratios.	69
7.7	Component mass break-down for varying spool speed at design BPR.	70
7.8	Effect of spool speed on the aerodynamic efficiency and component mass.	70
7.9	Effect of bypass ratio on the flow path geometry and component mass sizes at design spool speed.	71
A.1	Shock loss coefficient, ζ_{sh} , as a function of immersion ratio, H , and modified diffusion parameter, D_m	75
A.2	Profile loss coefficient, ζ_p , as a function of immersion ratio, H , and modified diffusion parameter, D_m	75

List of Tables

2.1	Typical component sizing conditions. <i>Source: [14]</i>	8
2.2	Overview of aerothermodynamic performance optimisation codes. <i>Source: [15]</i>	9
2.3	Overview of component based weight estimation methods.	9
2.4	Overview of implemented noise prediction methods in Soprano. <i>Source: [16]</i>	11
2.5	Characteristic data for validation engines CF6-80C2/B6 (Roux [17]) and CFM56-7B24 (engine testrun data).	12
3.1	Blockage factor. [18]	17
3.2	Airfoil and velocity triangle nomenclature.	18
3.3	Special cases for general vortex design.	20
3.4	Experimental data used for validation of incidence angle and deviation angle prediction methods.	21
3.5	Fan inlet input parameters.	24
3.6	LPC inlet input parameters.	31
3.7	Constants K_i as mentioned in the diffusion factor calculations	34
4.1	Aeroengine material properties. <i>Source: [19-21]</i>	38
4.2	Baseline fatigue strength, S_{1000} , and loading factor, C_L , based on the material and loading conditions.	41
4.3	Reliability factor, C_R	41
4.4	Baseline bending fatigue limit, S_{be} , and cycle limit, N_{be}	41
4.5	Component materials and fatigue design input parameters.	42
5.1	Take-off simulation input parameters.	52
6.1	Input for noise spectrum level calculations of the CF6-80C2 engine.	63

Nomenclature

Symbols

Symbol	Units	Description
α	1/K	Coefficient of thermal expansion
α	deg	Absolute flow angle
β	deg	Relative flow angle
Γ^*	-	Blade dimensionless circulation parameter
γ	deg	Stagger angle
γ	-	Ratio of specific heats
δ	deg	Deviation angle
δ_0	deg	Deviation angle for zero incidence angle
δ^*	m	Boundary layer displacement thickness
ϵ	-	Polytropic efficiency
ζ	-	Loss parameter
ζ_t	-	Total loss parameter
ζ_M	-	Mach number correction factor
ζ_H	-	Flow area contraction correction factor
ζ_{Re}	-	Reynold's number correction factor
η	-	Isentropic efficiency
θ	deg	Camber angle
θ	m	Boundary layer momentum thickness
ι	deg	Incidence angle
κ	deg	Metal angle
κ	m	Peak-to-valley surface roughness
μ	-	Axial velocity ratio
μ_w	-	Weinig mu-factor
ν	-	Rotational velocity ratio
ν	-	Poisson's ratio
ξ_M	-	Mach number correction factor
ξ_H	-	Flow area contraction correction factor
ξ_{Re}	-	Reynold's number correction factor
π	-	Total pressure ratio
ρ	kg/m ³	Density
σ	-	Blade cascade solidity ratio
σ_θ	MPa	Hoop stress
$\sigma_{0.2}$	MPa	Yield strength
σ_r	MPa	Radial stress
σ_{ult}	MPa	Ultimate tensile strength
σ_{VM}	MPa	Von Mises stress
σ_y	MPa	Yield strength
τ	-	Total temperature ratio
τ	m	Blades clearance gap
Φ	-	Stage flow coefficient
Ψ	-	Stage loading coefficient
Ω	rad/s	Angular velocity
a	m	Blade chamber
A	m ²	Area
(a/c)	-	Blade chamber to chord ratio
b	-	Tuning factor

c, C	m/s	Absolute flow speed
c	m	Blade chord
(c/κ)	-	Blade chord to surface roughness
(c/h)	-	Blade aspect ratio
c_p	J/(kg.K)	Specific heat capacity
C_L	-	Blade lift coefficient
D	-	Diffusion factor
D	m	Diameter
D_{eq}	-	Equivalent diffusion factor
D_m	-	Modified diffusion factor
dH	-	“De Haller”-number
E	GPa	Young’s modulus
E_{kin}	J	Blade kinetic energy
$EPNL$	dB	Equivalent Perceived Noise Level
F	N	Thrust force
FHV	J	Fuel heating value
h	m	Height
h	J/(kg.K)	Enthalpy
h_0	J/(kg.K)	Total enthalpy
H	-	Immersion factor
H_{TE}	-	Boundary layer trailing edge shape factor
$(\Delta H/nU^2)$	-	Mean stage loading
i	deg	Incidence angle
$i_{0,10}$	deg	Incidence angle based on 10% blade thickness
$(K_\delta)_c$	-	Thickness correction factor
K_{bk}	-	Blockage factor
K_c	-	Compressibility correction factor
K_{it}	-	Thickness correction factor
K_{sh}	-	Shape correction factor
K_t	-	Thickness correction factor
l	-	Specific mechanical energy
l_i	m	Total stage length
LHV	J	Lower heating value
m	kg	Mass
m	-	Slope of linear relation between deviation angle and camber angle
$m_{\sigma=1}$	-	Slope of linear relation between deviation angle and camber angle for solidity ratio of 1
\dot{m}	kg/s	Mass flow
M	-	Mach number
MFP	-	Mass flow parameter
n_b	-	Number of blades
n_{stages}	-	Number of stages
P	Pa	Pressure
r	m	Radius
r_h	m	Hub radius
r_t	m	Tip radius
R	J/(kg.K)	Specific gas constant
Re	-	Reynold’s number
s	J/(kg.K)	Entropy
s	m	Blade spacing
(S/c)	-	Pitch chord ratio
SM	%	Surge margin
SPL	dB	Sound Pressure Level
t	m	Blade thickness
(t/c)	-	Blade thickness to chord ratio
T	K	Temperature

T_{max}	K	Maximum operational temperature
T_0	K	Total temperature
U	m/s	Rotor tangential speed
v, V	m/s	Velocity
V	m ³	Volume
w	-	Pressure loss coefficient
w	deg	Relative flow speed
W	kg/s	Mass flow
Z	-	Loss factor

Subscripts/Superscripts

Subscript	Description
0	Nominal conditions
θ	Tangential direction
$0, t$	Total
$1, i$	In
$2, ii$	Out
af	Airfoil
avg	Average
b, bl	Blade
$bypass$	Engine bypass stream
$core$	Engine core stream
cg	Center of gravity
cr	Critical
end	End-wall
f	Fuel
$firtree$	Firtree
h	Hub
i	Element i
o	Overall
opt	Optimal
m	Mean
max	Maximum
min	Minimum
$neck$	Neck
p	Propulsive
$platform$	Platform
$post$	Post
pro	Profile
r	Radial direction
ref	Reference
sec	Secondary
$shock$	Shock
srd	Shroud
t	Tip
tc	Tip clearance
th	Thermal
TO	Take-off
$trans$	Transmission
z	Axial direction

Abbreviations

Abbreviation	Description
ACARE	Advisory Council for Aeronautics Research in Europe
ANOPP	The Aircraft Noise Prediction Program
ATAG	Air Transport Action Group
AVR	Axial velocity ratio
BEM	Blade-element method
BPR	Bypass ratio
BS	Burst speed
CAD	Computer-aided design
CC	Combustion chamber
DCA	Double circular-arc
DM	Design margin
EPNL	Equivalent Perceived Noise Level
ESDU	Engineering Sciences Data Unit
FPR	Fan pressure ratio
HP	High pressure
HPC	High pressure compressor
HPT	High pressure turbine
HTR	Hub-to-tip ratio
IATA	International Air Transport Association
IP	Intermediate pressure
KBE	Knowledge-based engineering
LE	Leading edge
LHV	Lower heating value
LP	Low pressure
LPC	Low pressure compressor
LPT	Low pressure turbine
MFP	Mass flow parameter
NACA	National Advisory Committee for Aeronautics
NASA	National Aeronautics and Space Administration
ODE	Ordinary differential equation
OPR	Overall pressure ratio
PDE	Partial differential equation
PS	Pressure side
SAE	Society of Automotive Engineers
SFC	Specific fuel consumption
SM	Surge margin
SPF	Superplastic forming
SPL	Sound pressure level
SS	Suction side
STOL	Short take-off and landing
TE	Trailing edge
TIT	Turbine inlet temperature
TO	Take-off
UHC	Unburned hydrocarbons
VTOL	Vertical take-off and landing

1

Introduction

In 1905, the Wright brothers were the first to achieve manned, powered flight with a heavier-than-air machine. The main contributor to their success was a better understanding of the aerodynamic behaviour of an airflow over a lifting surface and the resulting reaction forces. Based on the results of their own wind-tunnel experiments, they discovered large discrepancies between existing lift and drag estimations, which were provided at the time by look-up tables as well as their experimental test results. With years of expertise in glider building, they were able to develop an aircraft with a tri-axial system for flight control, a system that is still used today, immortalizing themselves as the first to accomplish manned flight.

After their successful attempt, the Wright brothers continued to improve their design over the next few years. Although the main airframe remained approximately the same, the generation of sufficient thrust to a sustained flight remained a problem, thus encouraging improvements in the engine design. The worlds first industrial gas turbine was tested, marking a historical breakthrough in the field of engine development. At the time, critics did not believe in the potential for aeronautical applications due to the weight restrictions for aircraft propulsion systems. However, the development of this type of internal combustion engine boosted after 1940 and nowadays gas turbine propulsion systems dominate the domain of aircraft propulsion.

Over the years, the focus of aircraft design has shifted, and the question is no longer whether the aircraft flies, but rather how to optimize the economic potential on a predefined mission. Although the current understanding of the complex aerodynamic flow field through an engine extends way beyond the level of knowledge at the beginning of the 20th century, the propulsive system design still remains one the most challenging tasks in the aircraft design process.

1.1. Problem statement

From an economical perspective, the aviation market has historically proven to be resilient to external financial shocks by repeatedly showing quick recovery after multiple economic recessions and oil crisis throughout history. Recent market study by Airbus shows that over the past two decades, air transportation industry has been steadily growing at approximately 5% each year. It is expected for this growth to be sustained for at least another 20 years [22].

While the market is constantly growing, the environmental footprint of air transportation is increasing as well. The Advisory Council for Aeronautics Research in Europe (ACARE) has set several (non-binding) goals to reduce the environmental impact of the aviation industry [23] [24]. The main focus lies on the reduction of emissions in three separate categories: noise production, CO_2 emissions, and NO_x , CO & UHC emissions. The aimed reductions in emissions are described as a percentage of the baseline value, which represents the capabilities of a typical new aircraft from the year 2000.

A visualization of the targeted reduction of emissions for the years 2020 and 2050 is shown in figure 1.1. In 2020 both CO_2 emissions and noise production should be reduced by at least 50%, while an 80% decrease in NO_x , CO & UHC emissions is desired. By the year 2050, CO_2 emissions should be decreased by a total 75%, which is coherent with the future aviation targets as described by the Air Transport Action Group (ATAG) [25]. The noise production should be decreased by 65%, and finally a large

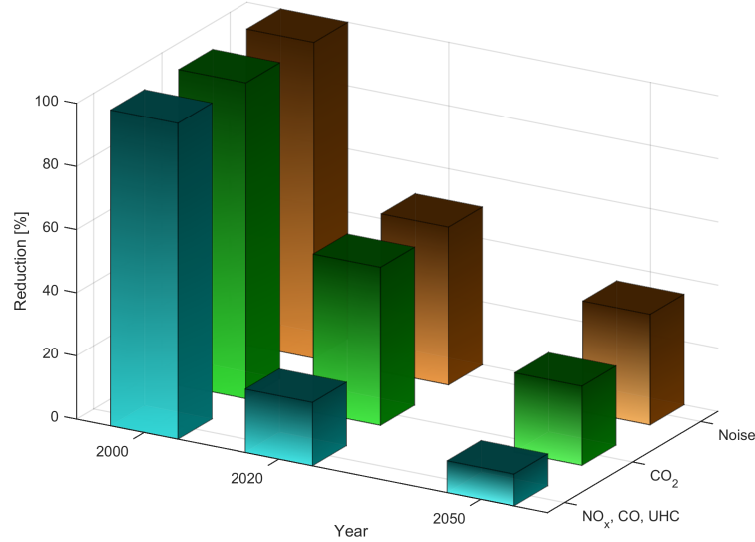


Figure 1.1: Main goals for reduction in emissions as set by ACARE for the years 2020 and 2050 as compared to the capabilities of a typical new aircraft from the year 2000.

cutback on the NO_x , CO & UHC pollutants should result in a relative emission of 10% compared to the baseline value. These goals have been referred to as "extremely challenging" by ACARE, and require revolutionary change in the aviation industry.

The International Air Transport Association (IATA) has created a roadmap, which describes a possible route to achieve the envisioned reduction of emissions. IATA states that there are four main contributors that can lead to the required improvement: technology, operations, infrastructure and economic measures [1]. Figure 1.2 shows the envisioned route by IATA to achieve the goal of CO_2 emissions reduction by the year 2050. The annual growth of global air traffic demand causes a rapid increase of gross emissions when current technology is not improved. Compared to the desired gross emissions curve, there is a large discrepancy in the predicted emissions path, as seen in 1.2. IATA states that improved engine technology and operations are quickly implementable and dominate the gross emissions decrease in the first few decades. The use of biofuels and implementation of radical new technologies in the aviation industry are expected to be main contributors to lowering emissions in the long term.

Including the environmental aspects in the engine design process further tightens the constraints on the design space, while performance targets are ever more demanding. The radical advancements in engine technology as envisioned by IATA require new design methods that allow for quick investigation of conceptual engine designs. Current design tools often focus on optimizing the aerothermodynamics of the engine while other important factors such as the engine weight and size are not taken into account. However, accurately predicting component weights early on in the design cycle is important, as errors in the initial weight estimates may lead to compulsory design changes in later design phases, which always goes at an increased cost compared to earlier adoptions. Therefore, this thesis focusses on the development of an engine design and sizing tool in the conceptual design phase.

1.2. Thesis objective

In aeroengine design, predicting the effects of design parameters on total engine performance is extremely difficult since the coupling of engine components is possible. This results in a chain reaction of changes throughout the engine, and often the redesign of more than one component to ensure optimal performance for the new design configuration. Proper investigation of parameter changes in engine design is often conducted with engine design tools, which provides the designer with more insight on the design process. This thesis contributes to the development of such an engine design and sizing tool.

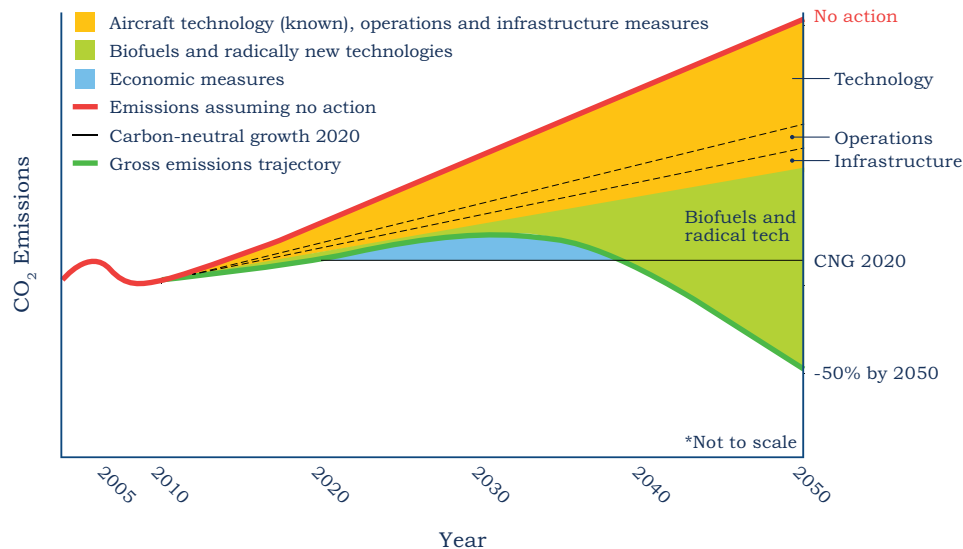


Figure 1.2: Schematic CO_2 emissions reduction roadmap. *Source:[1]*

In this work, fan and booster stages of a high bypass-ratio twin-spool turbofan engine in the conceptual design phase are considered. The component design is completed using three separate modules:

- **Aerothermodynamic module**
Analyzes the gas path through the component and estimates component aerodynamic efficiency based on empirical loss models.
- **Structural analysis & weight estimation module**
Conducts a structural analysis on the load carrying components, generates component geometries and ultimately calculates the component weight.
- **Noise prediction module**
Generates the noise spectrum of the fan stage, and performs a fly-over simulation to calculate the perceived noise levels on the ground.

The engine conceptual design and sizing tool optimizes the aerodynamic performance, then determines the engine component weights and predicts the noise generated by the fan stage.

Each module is first validated separately before the research question is addressed. The aerodynamics module is validated using existing engine data and data from NASA rotor experiments from the Lewis Research Center in Cleveland, Ohio. The gas path analysis is compared to the data gathered from an engine test-run with a CFM56-7 engine. Structural analysis and design of the compressor disks is compared to the results from T-AXI Disk.

After all modules are validated, the effects of increasing fan tip diameter on the total engine performance is investigated. The total engine performance is defined by the output of the three modules, and the aerodynamic efficiency, component weight and noise production are considered. It should be noted that fan tip Mach number is fixed in the analysis, as fan tip Mach number is often considered the limiting factor in high bypass-ratio turbofan engine design. Furthermore, the effects of spool speed on the total engine performance are investigated. In this analysis the tip diameter is fixed, and hence the Mach number will vary. For both cases the flow conditions at the fan face are assumed to be constant throughout the analysis.

It is expected that increasing tip diameter results in higher efficiencies, decreased noise propagation, and increased engine weight. The fixed hub-to-tip ratio (HTR) pushes the annulus area outwards and the inlet face area increases, which in term results in a larger mass flow rate. Fan casing weight is increasing as a result of the outwards shifted annulus area. A thicker blade containment casing is required to maintain the larger shaped fan blades in case of a blade release.

The fixed tip Mach number limits the rotational spool speed, causing higher stage loading in the low-pressure compressor, or more compressor stages are required to achieve the design pressure ratio. Hence,

either the compressor efficiency decreases or the compressor weight increases, and since the compressor design routine designs for minimum number of stages with a maximum stage loading parameter, the outcome is uncertain.

Finally, the total engine noise generated decreases as a result of the larger bypass mass flow rate. The larger mass flow rate through the bypass duct decreases the average exit stream velocity, and since jet noise scales to the exit velocity via V^8 , large decrease in jet noise is expected. Fan noise, however, increases due to the larger mass flow which is the main contributor to the normalized sound pressure level.

For the increasing spool speed analysis, the aerodynamic efficiency of the fan is expected to decrease, as large parts of the fan blade will operate in the supersonic region. This causes an increase of pressure losses over the fan blade due to larger shock losses. The spool speed causes higher centrifugal stresses at the blade root, hence larger fan and LPC disks are required. The LPC system might need less stages since more work per stage can be done due to the larger rotational velocity. Furthermore, the fan blade containment casing is increased in thickness as the blade release kinetic energy increases due to the larger rotational blade speed. Hence the fan mass is expected to increase, while the effect on the LPC remains undetermined at this point. Regarding noise, it is expected that with increasing spool speed the noise performance of the fan stage is worse, due to the increased tip Mach number.

1.3. Report outline

The conceptual design and sizing tool is capable of determining the performance in terms of aerothermodynamic stage performance, component weight calculations and noise predictions. In the report, these three modules are treated in separate chapters; however, first some general considerations with respect to turbofan engine design are treated in chapter 2. The chapter elaborates on the design choices, states general assumptions and provides an overview of readily available research in the subjects of aerothermodynamic design tools, weight estimation and noise prediction methods. After that, the aerodynamic analysis and design of the fan and compressor stages is treated in chapter 3. The structural design and weight estimation of the components of the low pressure compressor stages is then considered in chapter 4. The noise module including the calculation of the noise spectrum of the engine and determination of the perceived noise levels, is then explained in chapter 5. The modules are then validated using existing engine data in chapter 6. After all modules have been treated and are validated, the effects of increasing the fan tip diameter and varying spool speed are determined. Results to this analysis are presented in chapter 7, including conclusions drawn from these effects. Finally, recommendations regarding future research will be addressed in chapter 8.

2

General Considerations

During the conceptual design phase of turbofan engines a large number of designs is analysed to investigate the effects of design input parameters on the total engine performance. Ultimately, the best designs from the conceptual design phase are used as input for the next, more detailed, "preliminary design" or "detailed design" phase.

2.1. Turbofan configuration & lay-out

There are many different propulsion system types that can be used on aircraft for thrust generation. In the early ages of aircraft design, the propulsion systems mainly relied on state-of-the-art car piston engines, modified for light weight for aircraft applications. Nowadays, a wide range of propulsion system types exists: piston-props, turboprops, turbofans, turbojets, ramjets and rockets. The type of propulsion system that is used for the design mission, can easily be determined, since each of these engine types has its limits and its ideal operating conditions.

For most commercial aircraft applications, the turbofan engine allows for the best coverage of a typical flight mission. The majority of current commercial aircraft in operation are equipped with high-bypass turbofan engines, as they provide high thrust, have good reliability and high fuel efficiency. The conceptual design and sizing tool described in this thesis is based on the turbofan engine type.

Within the family of turbofan engines, a variety of engine configurations exist. This section will shortly present the different options available in terms of spool configurations and compressor types for turbofan engines. Other design choices such as intercooling and/or reciprocating systems are not considered here, as they further increase the design complexity which extends beyond the scope of this thesis.

2.1.1. Spool configurations

The fan and compressor stages in front of the combustion chamber are driven by the turbine stages behind it. The power of the turbine is transferred to the compressor by means of a spool, which is the physical connection between the two components. The number of turbine and compressor stages can vary from engine to engine, but also the connection between these stages can vary, by driving different stages on different spools. The main advantage is that the spools can turn on different speeds, which can also be achieved using a gearbox. The following types of spool configurations are considered: single spool, multi-spool and geared.

The single spool is the most basic configuration for a turbofan engine, as the fan and compressor stages are all driven by the turbine stage. Since there is only one spool, the design complexity is minimal, and therefore a reliable design. However, in practice with such a configuration stable operation conditions are hardly established at off-design conditions, such as part-throttle settings. Therefore, this configuration is not commonly used.

In a two-spool design, the high pressure compressor (HPC) is connected to the high pressure turbine (HPT) with a high pressure (HP) spool, while the fan is driven directly by the low pressure turbine (LPT) on the low pressure (LP) spool.

The two-spool configuration is often equipped with an extra compressor stage between the fan and HPC stage. This design is called the boosted two-spool configurations, and higher overall pressure ratios can be achieved by placing such an intermediate compressor stage between the fan and HPC component. The low pressure compressor (LPC) or booster stage, boosts the fan exit air by pressurizing the flow before entering the HPC stage. This is one of the most common configurations in the turbofan engine family.

In modern high-bypass turbofan engines, the booster diameter is limited in size, to allow for sufficient bypass area. Since the rotational speed of the LP spool in a boosted two-spool configuration is often limited by the fan tip speed, the decreased diameter of the booster stage causes a lower IP compressor pressure ratio, and hence more stages are required to achieve the same pressure ratio. However, a three-spool configuration allows the fan stage to be driven by the LP spool, while the IP compressor is driven by a separate IP spool, connected to a separate turbine stage; the IP turbine. The HPC and HPT are still directly connected via the HP spool.

Another approach to counteract the problem of limited booster stage rotational speed as described above, is to use the boosted two-spool configuration with a gearbox between the LP spool and the fan stage, allowing the fan to turn at a lower speed than the LPT and IP compressor stage. However, this increases the design complexity.

2.1.2. Compressor types

The designer also has to make a choice of the type of compressor that will be used in the engine. There are compressors available of the axial, axial-radial and centrifugal type [26].

The axial compressor type has large mass flow capacity and allows for stage stacking. Therefore, it is capable of achieving high overall pressure ratio by increasing the number of axial compressor stages, without increasing the frontal area, but at cost of total compressor length.

Centrifugal compressors are the most robust type of compressors, although they are limited in the achievable pressure ratio. Also, for aircraft application, the centrifugal compressor is not ideal, as for increasing pressure ratio the diameter of the compressor increases.

The axial-radial compressor is mainly seen in smaller aircraft engines in the HPC. As for small engines, the core size is smaller, the last stages of the HPC become very small, complicating the process of achieving the required pressure ratio due to increasing tip clearance effects. Therefore, axial-radial compressor is usually an ordinary axial compressor with a radial compressor stage at the end.

2.1.3. Flow mixing configurations

The last configuration discussed here is the difference between mixed and unmixed flow turbofan engines. Mixed turbofan engines combine the bypass and core flow before the exhaust, which lowers the temperature gradient between the ambient and the exhaust stream, and lowers the jet exhaust velocity and thus the jet exhaust noise. Although there are some advantages to the mixed turbofan engine configuration, the additional casing material needed for the bypass duct drastically increases the total engine weight.

2.1.4. Chosen configuration

The conceptual engine design tool will be limited to one specific turbofan configuration. A boosted two-spool configuration is chosen for its design simplicity as compared to the geared and three-spool configurations. Due to the ability of stage stacking and the lower frontal area, the axial compressors type is used. Finally, an unmixed flow configuration is used for weight reduction purposes. In conclusion, the turbofan engine configuration that will be considered throughout this thesis is a boosted two-spool unmixed turbofan engine, with axial flow compressor stages.

A sectional drawing of a typical two-spool, unmixed high bypass ratio turbofan engine is shown in figure 2.1.

2.2. Turbofan components

Following the gas path from the free-stream air through the core of the turbofan engine, the first component the air particles will encounter is the fan stage.

The turbofan engine is characterized by a fan positioned in front of the gas generator. The fan turning speed is relatively low, but displaces large air mass at relatively low speeds, which boosts the

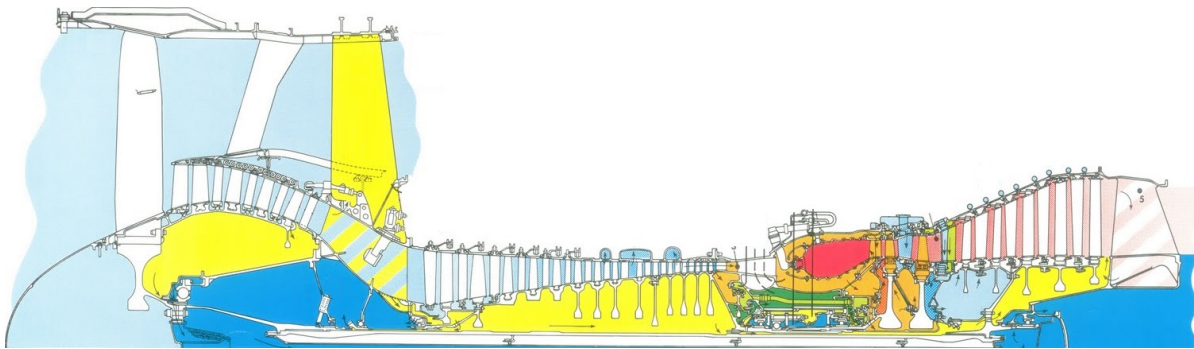


Figure 2.1: CF6-80C2 Sectional Drawing. *Source: [2]*

fan propulsive efficiency. The aerodynamic performance of the fan is an important factor in turbofan engine design as it is closely related to the specific fuel consumption (SFC) of the total engine. A 1% increase of fan efficiency can result in 0.7% SFC reduction, which is a key engine design parameter for long range aircraft [27].

The fan stage also puts additional constraints on the the engine design process. In two-spool turbofan configurations, the fan tip speed limits the LPC turning speed, as noise propagation from the fan tips can quickly exceed the allowable levels. Implementation of a gearbox would allow for higher LP spool rotational speeds, while still satisfying the fan tip speed constraint. However, due to increase in engine design complexity, the gearbox configuration is not considered in this thesis. These and other engine lay-out design choices have already been treated in section 2.1.

After the fan stage, the air enters the low pressure compressor or booster stage. The LPC stage pre-pressurizes the airflow before entering the high pressure compressor stage. The booster stage is connected to the LP spool and hence turns at the same speed as the fan component. Therefore, to increase the LPC efficiency, the flowpath is pushed outwards. After the LPC a connecting duct is needed to direct the flow inwards to the HPC inlet, since the HPC turns on the high pressure spool and thus the high turning speed limits the tip geometry.

The HPC consists of multiple compressor stages with narrowing annulus area towards the end. In the HPC, pressure losses occur due to many complex aerodynamic phenomena, tip clearance effects and cooling air abstraction. Also the HPC design has a high exchange rate between efficiency and SFC; a 1% increase in HPC efficiency can lead to $\sim 0.5\text{--}1\%$ reduction in SFC [26].

The compressed air now enters the combustion chamber (CC). The combustion chamber adds heat to the gas stream by burning fuel, increasing the turbine inlet temperature. At the design power conditions, the combustion process typically reaches efficiencies higher than 99.9% in the process of converting chemical energy to thermal energy [28].

The High Pressure Turbine (HPT) is designed to extract power from the hot gas that leaves the CC, and powers the HPC stages. The hot gas entering the turbine stage is first directed by a stator guidance vane to drive the rotor stage. Dependent on the number of HPT stages, this sequence is repeated.

The historical trend of increasing TIT for higher thermal efficiencies has caused temperatures to rise up to 700 degrees Celsius in excess of the airfoil material melting point [29]. Therefore, to protect the airfoil material, sufficient cooling should be provided. The high pressure turbine inlet guidance vane is typically film-cooled, other stages are also cooled by combination of internal and external cooling. The downside of cooling are mainly the resulting pressure losses in the stages where the cooling air is subtracted and secondary losses in the cooled stage due to aerodynamic distortions.

The Low Pressure Turbine (LPT) extracts power from the gas that just left the HPT stage. The LPT drives the low pressure spool, which is connected to the Fan and LPC stage. Like a the HPT stage, the flow is first directed by a guidance vane, and then the flow goes to the rotor stage to subtract the energy from the flow. This is repeated for the number of LPT stages, which altogether forms the LPT. An increase of 1% in LP turbine efficiency is equivalent to 1.25% decrease in SFC [30].

After the LPT stage, the gas only has to pass the exhaust nozzle before it reaches the end of the engine. The nozzle should increase the velocity of the exhaust gas before discharge from the nozzle, with minimum total pressure loss. Furthermore, the nozzle exit pressure should match the atmospheric pressure as close as possible to minimize losses, and should suppress jet noise [31].

2.3. Design Point

When designing an aircraft, it typically should be designed for a certain flight mission. For commercial aircraft, a typical design mission consists of some standard manoeuvres, as illustrated in figure 2.2.

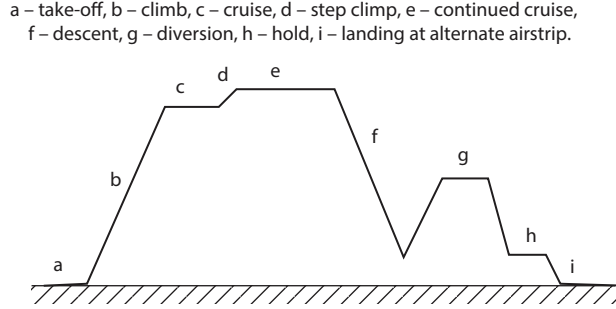


Figure 2.2: Typical mission profile for civil aircraft. *Source:* [3]

Also ground operations have to be considered, such as *roll to runway* before take-off and *roll to gate* after landing. The engine should be designed such that the aircraft is able to complete the full mission and stable operation is ensured over the entire range of operation conditions. In this section, the different types of design point considerations and the off-design analysis are treated.

The designer can choose to optimize the engine cycle performance for either one operating condition (single point design), or try to achieve the best overall performance over the entire mission by optimizing the engine cycle for multiple operating conditions (multi-point design). Typically, for civil aircraft, the aerodynamic design point at cruise is taken as main operating condition, as this flight condition is the nominal operating condition in the design mission, as shown in figure 2.2. However, the highest thermal loads and spool speeds occur during the take-off manoeuvre, and should therefore also be considered during the design process. Hence, these two conditions form the general design conditions for civil aircraft:

1. Cruise, aerodynamic design point
2. Hot day take-off, mechanical design point

For turbofan engine component design however, different design conditions may apply. An overview of the design conditions for individual turbofan engine components is described by Kurzke [14], and can be found in table 2.1.

Table 2.1: Typical component sizing conditions. *Source:* [14]

Component	Design Information	Cycle Conditions	Flight Condition	Mission Condition
Fan	Aero Design Point	Max PR	Sea Level Static	Take-Off
Compressor	Aero Design Point	Max PR	Upper LH Corner	Max Climb
Burner	Max Turbine Flow Function	Max Airflow	Sea Level Max Speed	Sea Level Dash
HPT	Max Loading	Max Loading	Sea Level Static	Take-Off
LPT	Max Loading	Max Loading	Sea Level Static	Take-Off
Augmentor	Max Fuel Flow	Max Fuel Flow	Sea Level Max Speed	Sea Level Max Speed
Nozzle	Min Throat Area	Min Throat Area	Sea Level Static	Take-Off
	Max Throat Area	Max Throat Area	Mid Envelope	Cruise
	Max Exit Area	Max Exit Area	Upper RH Corner	Dash

From table 2.1 it can be seen that the aerodynamic design conditions for both the fan and LPC stages are at their maximum pressure ratio. These component aerodynamic loading conditions occur at a certain point in the flight envelope. For the fan stage, the maximum pressure ratio is achieved at maximum climb at sea level conditions, while for the LPC the maximum pressure ratio occurs at the top-of-climb condition.

2.4. Modules

As mentioned earlier, the main objective of this thesis is to inspect the effects of engine design parameter changes on the aerodynamic performance, engine weight and noise generation of the engine. In order to

obtain these results, the performance of the engine is calculated using three modules: an aerodynamics module, weight module and noise module.

2.4.1. Aerothermodynamic performance

The aerodynamics module is used for the aero- and thermodynamic calculations in the fan and LPC stages. In the design process of both stages, many variables are not known on beforehand, while they are required for proper calculation of the gaspath analysis. Therefore, these parameters should be guessed initially, and after calculating the gaspath the parameters are compared to the new calculated values. This routine is then repeated until the the guessed and calculated values have converged. Iterative solver structures like this are used to ensure convergence of several design parameters in the fan and LPC desing case. A more detailed description of the solver structure for the fan and LPC stage are described in sections 3.4.1 and 3.5.1 respectively.

Aerodynamic performance of turbine engines is a well-studied subject, and several codes have been developed over the years for the purpose of aerodynamic performance analysis. Kyprianidis [15] provides a good overview of the developed codes, which is summarized in table 2.2.

Table 2.2: Overview of aerothermodynamic performance optimisation codes. *Source: [15]*

Code name	Institution	Authors	Year
GENENG	NASA	Koenig & Fishbach [32]	1972
GENENG II	NASA	Fishbach & Koenig [33]	1972
TURBOMATCH	Cranfield University	MacMillan [34]	1974
TURBOTRANS	Cranfield University	Palmer & Cheng-Zong [35]	1982
GSP	NLR & TU Delft	Visser [36] Visser et al. [37]	1995 2000
GeSTPAn	Chalmers University	Grönstedt [38] Grönstedt et al. [39]	2000 2002
NCP	NASA	Claus et al. [40] Drummond et al. [41]	1991 1992
NPSS	NASA	Lylte [42]	2000
PROOSIS	European Universities	Alexiou [43] Bala [44]	2007 2007

2.4.2. Weight estimation

Weight estimation methods for aircraft engines are available at different levels of accuracy. Whole-engine based weight prediction methods are often used in preliminary aircraft design, where the design of the aircraft alters, but the engine remains the same. These methods often correlate the total engine mass to a few basic engine parameters, and do not take any physical processes occurring inside the engine into account. Another approach for engine weight estimations is based on the individual engine component weights for which also a variety of methods are readily available. Lolis [45] provides a good overview of these earlier developed weight estimation techniques in table 2.3.

Table 2.3: Overview of component based weight estimation methods.

Method	Authors	Year
VTOL/STOL	Sagerser al. [46]	1971
NASA WATE	Pera et al. [47]	1977
NASA WATE (simplified)	Klees & Fishbach [48]	1978
NASA WATE-2	Onat & Klees [49]	1979
NASA WATE-S	Hale [50]	1982
Military turbojet	Sanghi [51]	1998
Disk weight & life	Tong et al. [11]	2004
NASA WATE++	Tong & Naylow [52]	2008
WeiCo (Weight & Cost)	Chalmers University & Stuttgart University [53]	2007

In this conceptual engine design and sizing tool, the stage weight is determined using a component based approach. A break-down of weight components in the fan and LPC stages can be found in figure 2.3. The weight estimation module aims at designing all components for minimum weight, which is determined using both static and fatigue design methods. In general, the static design determines the minimum required material thickness of the component, after which a fatigue analysis determines the

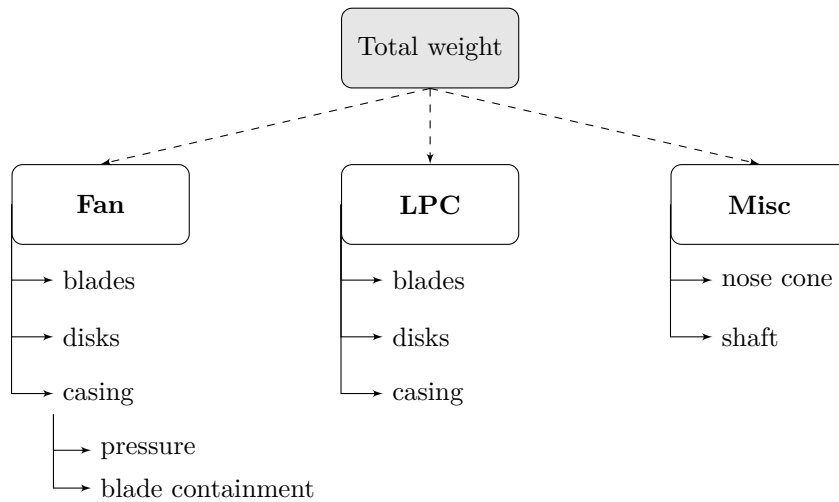


Figure 2.3: Engine weight component break-down.

fatigue design safety factor of the component. If the current fatigue safety factor does not meet the desired safety factor, the material thickness is modified accordingly, and the process is repeated until the solution has converged.

2.4.3. Noise prediction

Noise propagates from different sources of the engine, and there are large differences in the magnitude of each of these sources between different engine types. Figure 2.4 shows a comparison of the magnitude and sources of noise for both a low BPR and a high BPR turbofan engine. For bypass ratios larger than 5, the increased internal noise sources dominate the jet noise.

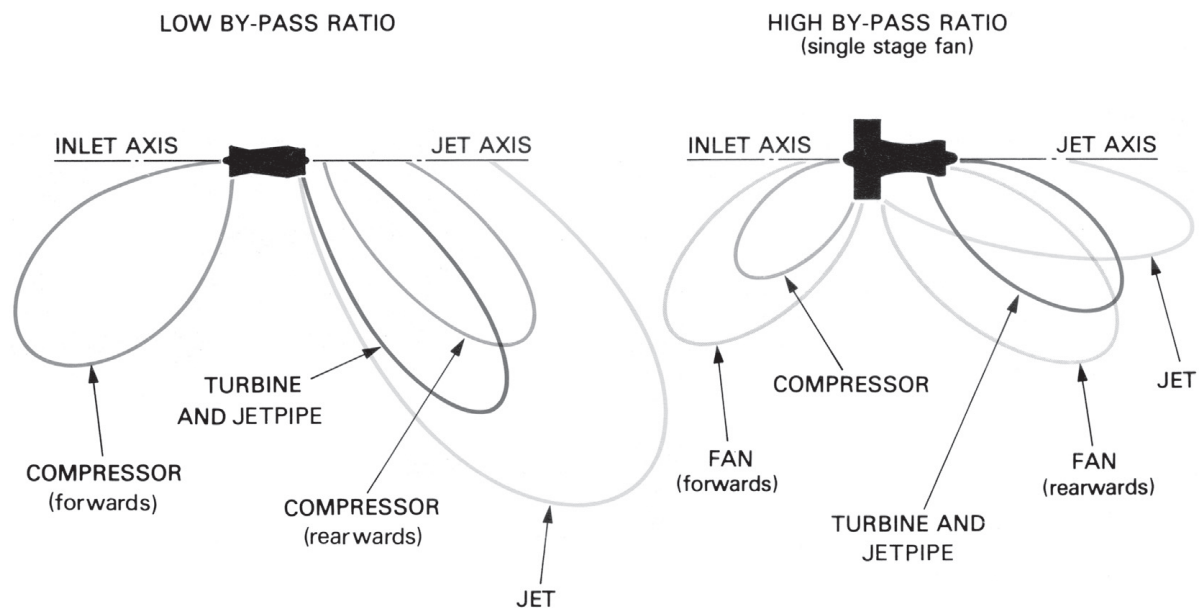


Figure 2.4: Comparison of noise sources and magnitudes for low- and high-BPR turbofan engines. *Source: [4]*

A European research project called “Environmentally Friendly Aero Engines” (VITAL), also focuses on the development of an engine design tool, capable of evaluating new engine architectures in the preliminary design phase. Within this research project, a Technoeconomic, Environmental and Risk Assessment tool called TERA2020 is being developed [16]. The tool consists of five modules: a noise module, an emissions module, a weight and dimensions module, an aircraft module and a performance module. The noise module is based on the extensive empirical acoustic prediction software called

Soprano. Kyprianidis et al. [16] give an overview of the implemented noise prediction methods used in the Soprano code, which are shown in table 2.4 below.

Table 2.4: Overview of implemented noise prediction methods in Soprano. *Source: [16]*

Noise source	Prediction method
Fan and compressors	Heidmann [54] Kontos [55]
Coaxial exhaust jet	Stone & Krejsa [56] SAE ARP 876D [57]
Turbine	Krejsa [58]
Airframe	Fink [59]
Noise propagation	SAE ARP 866A [60] Chien & Soroka [61] SAE AIR 1751 [62]
Installation effects on jet noise	Blackner and Bhat [63]
Contra-rotating rotors interaction tone noise	Hanson modified ([64] and [65]) Heidmann adapted ([54] and [55])

The noise prediction methods in Soprano use the ANOPP method by Heidmann [54] and the improved ANOPP method by Kontos [55] for the fan and compressor noise estimation. Diéz [5] introduced a third noise estimation method from the Engineering Society of Data Units (ESDU), and did a comparison with the three noise estimation techniques. It was concluded that no large differences between the methods were appreciated.

2.5. Validation

The separate modules are validated using existing engine data. For the CFM56-7B engine much data is available online. Test results from an engine testrun with a CFM56-7B24 engine are also available and hence the engine is used for aerodynamics and weight module validation. For the noise module validation, the CF6-80C2/B6F engine is used as extensive fan noise test were conducted with this engine of which the data is available.

For the noise module validation, the interaction with the aircraft is important, as this determines the flightpath and hence other values for the EPNL are observer. The CF6-80C2 is a high bypass ratio turbofan engine, manufactured by GE aviation which has been certified on several long-range aircraft, including the Airbus A300 and A310 series, Boeing's 747-400 and 767 models and the McDonnell Douglas MD-11. The CF6-80C2 engine is shown in figure 2.5. The CFM56-7B engine is shown in figure 2.6 some basic engine characteristics are mentioned in table 2.5.



Figure 2.5: CF6-80C2 engine. *Source: GE Aviation*



Figure 2.6: CFM56-7B engine. *Source: CFM International*

Table 2.5: Characteristic data for validation engines CF6-80C2/B6 (Roux [17]) and CFM56-7B24 (engine testrun data).

Parameter	Symbol	Engine		Units
		CF6-80C2/B6	CFM56-7B24	
Stages fan/LPC/HPC		1 / 4 / 14	1 / 3 / 9	
Fan diameter	D_{fan}	2.362	1.5494	m
Length	L	4.087	2.511	m
Mass	m	4386	2366	kg
Bypass ratio	BPR	5.06	5.06	–
Overall pressure ratio	OPR	31.1	25.383	–
Take-off thrust	T_{ssl}	267200	104570	N
Mass flow rate	\dot{m}_{ssl}	–	342.9	$\frac{kg}{s}$
Specific fuel consumption	SFC_{ssl}	$9.5 \cdot 10^{-5}$	$1.1061 \cdot 10^{-5}$	$\frac{kg}{N \cdot s}$

3

Aerodynamics

3.1. Governing equations and assumptions

For the flowfield analysis through the axial fan and compressor components, the Navier-Stokes equations are used as a starting point. However, as many turbine engine design handbooks suggest, for the purpose of the conceptual design phase some simplifying assumptions can be made with respect to the flowfield:

- Steady flow, no variation of flowfield parameters in time, $\frac{\partial}{\partial t} = 0$
- Axisymmetric flow, no variation of flowfield parameters in tangent direction, $\frac{\partial}{\partial \theta} = 0$
- Adiabatic flow, no heat transfer between the flow and the walls, $\dot{q} = 0$
- Radial equilibrium, no radial shift of the stream surface outside the blade rows, $C_r = 0$

Applying these assumptions to the set of Navier-Stokes equations greatly simplifies the three-dimensional gaspath analysis. This leads to a set of governing equations which describe the compressible flow through the axial compressor and fan stage in this thesis, which are given below:

- Continuity equation

The continuity equation states that the total mass flow should be conserved in a given control volume. For compressible flow, the mass continuity is described by equation (3.1).

$$\rho_1 A_1 C_1 = \rho_2 A_2 C_2 \quad (3.1)$$

- Euler equation

The Euler's turbine equation describes the fundamental working principle for turbomachinery, and relates the temperature difference across a given control volume to the change in rotational speed and momentum. Equation (3.2) shows the equilibrium and the specific work or power consumed by the compressor.

$$P = \dot{W} = \dot{m} c_p (T_{t,2} - T_{t,1}) = \dot{m} \Omega (r_2 C_{\theta,2} - r_1 C_{\theta,1}) \quad (3.2)$$

- Radial equilibrium equation

The full radial equilibrium equation is given by equation (3.3).

$$c_p \frac{\partial T_t}{\partial r} = T \frac{\partial s}{\partial r} + C_\theta \frac{\partial C_\theta}{\partial r} + \frac{C_\theta^2}{r} + C_{ax} \frac{\partial C_{ax}}{\partial r} - C_{ax} \frac{\partial C_r}{\partial z} \quad (3.3)$$

The last term in the radial equilibrium equation accounts for the radial accelerations in the flowfield, which according to the earlier stated assumptions equals zero and hence is neglected.

The radial equilibrium equation is only applied at the fan stage. For rotating machinery with relatively small blade heights, such as the low pressure compressor, radial variations of the flowfield are relatively small, and these effects are assumed to be negligible. For the turbofan fan stage however, blades heights

are typically too large to ignore the variation of the flowfield along the blade span, and hence radial equilibrium should be applied to ensure a feasible design output.

Some general equations used for determining the change in total air properties and related static properties are discussed here as well. First, the total temperature ratio over an arbitrary stage is for three cases: the ideal case, assuming constant isentropic efficiency and assuming constant polytropic efficiency.

$$\frac{T_{t,2}}{T_{t,1}} = \left(\frac{p_{t,2}}{p_{t,1}} \right)^{\frac{\kappa-1}{\kappa}} \quad \text{Ideal case} \quad (3.4)$$

$$= 1 + \frac{1}{\eta_c} \left(\left(\frac{p_{t,2}}{p_{t,1}} \right)^{\frac{\kappa-1}{\kappa}} - 1 \right) \quad \text{Isentropic efficiency} \quad (3.5)$$

$$= \left(\frac{p_{t,2}}{p_{t,1}} \right)^{\frac{\kappa-1}{\eta_p \kappa}} \quad \text{Polytropic efficiency} \quad (3.6)$$

If the total conditions of the airflow are known, the static properties can be derived using equations (3.7) and (3.8):

$$T_1 = T_{t,1} \cdot \left(1 + \frac{\kappa-1}{2} \cdot M_1^2 \right)^{-1} = T_{t,1} - \frac{V_1^2}{2 \cdot c_{p,1}} \quad (3.7)$$

$$p_1 = p_{t,1} \cdot \left(1 + \frac{\kappa-1}{2} \cdot M_1^2 \right)^{-\frac{\kappa}{\kappa-1}} \quad (3.8)$$

3.2. Non-dimensional performance parameters

In compressor design it is common practice for a designer to control three main criteria: the flow capacity, the work done per stage and the distribution of flow diffusion over the rotor and stator blade row. These three specifications are controlled by non-dimensionalized performance parameters, to make them representative to any given operative condition.

Stage flow coefficient

The flow coefficient controls the flow capacity, and is defined as the axial flow velocity non-dimensionalized by the rotational velocity, as shown in equation (3.9).

$$\phi = \frac{C_{ax}}{U} \quad (3.9)$$

Stage loading coefficient

The dimensionless work done in a stage is expressed by the stage loading coefficient, which is derived from Euler's equation (3.2) and non-dimensionalized using the rotational velocity.

$$\psi = \frac{\Delta h}{U^2} = \frac{C_{\theta,2} - C_{\theta,1}}{U^2} \quad (3.10)$$

Stage reaction

The distribution of diffusion between rotor and stator blade rows is given by the stage reaction. The definition of the stage reaction is the ratio of the rotor static enthalpy rise divided by the stage total enthalpy rise.

$$\Lambda = \frac{h_2 - h_1}{h_3 - h_1} \quad (3.11)$$

For repeating stage designs ($C_1 = C_3$), the stage reaction can be rewritten in the following forms

$$\Lambda = \frac{W_{\theta,1} + W_{\theta,2}}{2U} = \frac{\phi(\tan \beta_1 + \tan \beta_2)}{2} \quad (3.12)$$

$$\Lambda = \frac{1 + \phi(\tan \beta_2 + \tan \alpha_1)}{2} \quad (3.13)$$

Apart from the above mentioned design parameters, there are some non-dimensional performance parameters that describe the aerodynamic performance of the compressor stages.

Efficiency

The total-to-total adiabatic stage efficiency is given by equation (3.14) and relates the stage total pressure rise to the temperature rise of the stage. It defines the efficiency of the compression process by of the rotor and stator blade rows together.

$$\eta = \frac{\frac{p_{t,2}}{p_{t,1}}^{\frac{\kappa-1}{\kappa}} - 1}{\frac{T_{t,2}}{T_{t,1}} - 1} \quad (3.14)$$

Pressure- and temperature ratio

The stage total pressure ratio, Π , and total temperature ratio, τ , are defined by equations (3.15) and (3.16) respectively.

$$\Pi = \frac{p_{t,2}}{p_{t,1}} \quad (3.15)$$

$$\tau = \frac{T_{t,2}}{T_{t,1}} \quad (3.16)$$

Axial- and rotational velocity ratio

The axial velocity ratio, μ , defines the relative change in axial velocity over the blade row. Similarly, the rotational velocity ratio, ν , gives the change in rotational velocity due to radial shift over the rotor blade. Axial- and rotational velocity ratios are described by equations (3.17) and (3.18) respectively.

$$\mu = \frac{C_{ax,2}}{C_{ax,1}} \quad (3.17)$$

$$\nu = \frac{U_2}{U_1} \quad (3.18)$$

DeHaller number

The DeHaller number is a measure of the diffusion in each blade row. Too much diffusion in a blade row could cause flow separation leading to compressor stall or surge. Therefore, the DeHaller number is limited to minimum value of 0.72 for both the rotor and stator blade rows, which is an acceptable value for modern turbofan engines [66]. Equations (3.19) and (3.20) give the DeHaller number calculation and limits for rotor and stator stages respectively.

$$DH_r = \frac{W_2}{W_1} \geq 0.72 \quad (3.19)$$

$$DH_s = \frac{C_2}{C_1} \geq 0.72 \quad (3.20)$$

3.3. Gas path analysis

Aerodynamic performance prediction of axial compressors is often performed using a gaspath analysis. In a gaspath analysis the aerodynamic properties of the airflow throughout the component are calculated at all intermediate stations. From the resulting gas properties before and after the component, the stage performance parameters can be determined using equations mentioned in section 3.2.

3.3.1. Design methods

A gaspath analysis can be performed at different levels of accuracy. In the conceptual design phase, usually simple methods are used to increase the computational performance of the design tool. A method often used in conceptual design of turbomachinery is the mean-line design method. In a mean-line design, the flow is defined by the mean flow properties at each station. More information about the mean-line design method is given in section 3.3.1.

Although mean-line design methods are sufficiently accurate for most low- and high pressure compressor and turbine stages, the effect of the underlying simplifying assumption becomes apparent when stages with larger blade heights, such as the fan stage, are considered. Due to the increasing effect of three-dimensional flow phenomena that are not fully captured by the mean-line design method, the performance predictions start to deviate from the actual component performance. To better deal with three-dimensional flow effects, a blade-element design method (BEM) is used, which will be further elaborated upon in section 3.3.1.

Even more accurate results can be obtained by performing Computational Fluid Dynamics (CFD) analysis. In CFD analysis the flow path is discretized using a meshgrid with a finite volume around every node point. However, properly setting up the flow field and performing the analysis is a computationally time consuming process. Therefore, CFD analysis is mainly used for specific cases in later design stages, and is not further considered in this thesis.

Mean-line design

The mean-line analysis is a one-dimensional design method commonly used in conceptual engine design. Although the method uses an extremely simplified representation of the actual flow field, it allows the designer to quickly investigate effects on the performance of the component. Extensive research has been done in the field of compressor loss predictions and their use in conceptual design applications. Section 3.5 will further elaborate on the design methodology and loss prediction methods used in the mean-line design method. Combination of this rather simple design method with current loss prediction models has proven to deliver accurate results for performance prediction of modern compressor and turbine stages. [67]

Blade-element method

In the previous sections all calculations of the flow field were limited to the one-dimensional domain. For the low-pressure compressor component, a one-dimensional flow analysis at the mean-line results in a sufficiently accurate performance prediction for the conceptual design stage. However, in the fan stage the radial change of velocities in the flowfield result in appreciable spanwise variation of performance. Therefore, the one-dimensional mean-line design approach does not suffice here, and a blade-element method is used instead. In a blade-element method (BEM), the flow field is discretized in a number of smaller sections. At each section, a one-dimensional design approach is used to calculate the flow properties before and after the stage. Radial equilibrium and mass continuity are checked for all sections, and the axial velocity ratio is modified accordingly to converge the solution. The design process is described in more detail in section 3.4.1.

3.3.2. Annulus geometry

The first step in the design process of a component is determining the inlet and outlet annulus dimensions. For the fan stage the cross sectional area at the rotor inlet is determined using the inlet calculations as described in section 3.4.2. The input to the inlet calculation procedure should either be the inlet Mach number or airspeed. To fully describe the inlet geometry, one geometric parameter should be provided as input. The provided dimension can either be a fixed radial location (hub, mean, tip or root-mean squared (RMS) radius) or the non-dimensional hub-to-tip ratio (HTR). With the provided dimension and the annulus area, other dimensions can be calculated. Equation (3.21) shows the

hub radius calculation for provided hub-to-tip ratio.

$$r_t = \sqrt{\frac{A}{\pi(1 - HTR^2)}} \quad (3.21)$$

Based on the total pressure ratio and isentropic efficiency, the gas total conditions at the outlet can be determined using equations (3.5). The static properties are then calculated to determine the air density, which in combination with the mass continuity equation leads to the exit annulus area. The annulus shape between the inlet and outlet of the component is determined by the design flowpath geometry. The three most common flow path designs are the mentioned in figure 3.1 below. Another

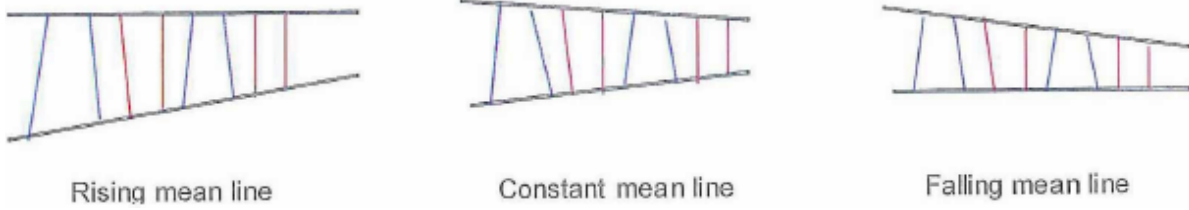


Figure 3.1: Flowpath geometry designs.

possible design is the constant root-mean square design, at which the radial location r_{RMS} is fixed. In this design, the annulus area above and below the fixed radial location are equal.

Finally, the blockage factor, K_B , is introduced to simulate boundary layer effects at the walls. The blockage factor is implemented in the mass equilibrium equation, which results in equation (3.22), and effectively reduces the annulus flow area.

$$\dot{m} = \rho \cdot C_{ax} \cdot A \cdot K_B \quad (3.22)$$

The blockage factor is a function of the component stage number, and is given in table 3.1.

Table 3.1: Blockage factor. [18]

Stage	N_i	1	2	3	4	5	6	7	8	9
Blockage factor	K_B	0.982	0.952	0.929	0.910	0.895	0.883	0.875	0.868	0.863
Stage	N_i	10	11	12	13	14	15	16	17	18
Blockage factor	K_B	0.860	0.857	0.855	0.853	0.851	0.850	0.849	0.848	0.847

3.3.3. Cascade design

The fan and compressor components consist of several stationary and rotating blade rows. The rotating blade row (rotor) adds energy to the working fluid by increasing the swirl velocity, while the stationary blade row (stator) is designed to remove the swirl velocity from the airflow caused by the rotor and create a desired swirl velocity profile for the next rotor blade row. In the stator blade row, the kinetic energy of the flow is converted to cause a static pressure rise. Special cases of stationary blade rows are inlet guide vanes (IGV) and exit guide vanes (EGV), which are specifically designed for zero swirl inlet and exit conditions respectively.

The ambient air entering the fan first passes the fan rotor, after which the flow is divided into two sections: the bypass and core flow. The bypass flow then passes an exit guide vane in the bypass duct which removes the swirl from the airflow, after which the air leaves the engine bypass duct through the bypass duct nozzle. The core flow enters the first stage of the low pressure compressor via an inlet guide vane, which is designed to give the flow the desired swirl distribution for the first compressor rotor stage. Depending on the number of compressor stages, the core flow passes multiple rotor-stator blade rows, which raises the total pressure of the flow. After the last compressor rotor blade row, the core flow passes the compressor exit guide vane, which again remove the swirl distribution of the flow.

Some primary assumptions regarding the rotor and stator blades are indicated here as well. The rotor tip gap is defined as the spacing between the rotor tip and the annulus. The tip gap clearance τ_{gap} , is assumed to be fixed at **5mm** for the fan stage and **1mm** for all compressor stages.

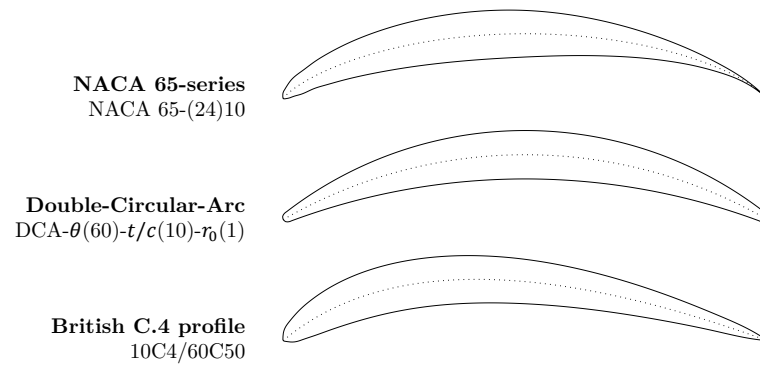


Figure 3.2: Three popular compressor cascades.

For fan and compressor design some common airfoil shapes are used. Three airfoil types are considered: Double Circular Arc (DCA), NACA 65-series airfoils (NACA) and British-C.4 airfoils (C4). Figures 3.2 shows the countours of the airfoils for 60° camber angle and 10% thickness-to-chord ratio. The flow over an airfoil cascade and the airfoil shape itself are defined by a several angles. Table 3.2 gives an overview of the nomenclature used in this thesis. The angle definitions are indicated in figure 3.3.

Table 3.2: Airfoil and velocity triangle nomenclature.

Symbol	Unit	Description
α	deg	Absolute flow angle
β	deg	Relative flow angle
γ	deg	Stagger angle
δ	deg	Deviation angle
ι	deg	Incidence angle
κ	deg	Metal angle
θ	deg	Camber angle
c	m	Chord
t/c	-	Thickness-to-chord ratio
a/c	-	Maximum camber location
b/c	-	Maximum camber
C	m/s	Absolute flow speed
U	m/s	Rotor tangential speed
W	m/s	Relative flow speed

3.3.4. Velocity triangles

The velocity triangles are used to indicate the direction and magnitude of the flow field velocity for both absolute and relative flow conditions. The angles are typically measured from the axial direction, which is used here as well. Figure 3.4 shows the general velocity triangle for a compressor stage.

From figure 3.4 a notable difference between inlet and exit velocity triangles can be seen. The axial velocity component decreases over a compressor stage due to flow diffusion. An important parameter in compressor design is the axial velocity ratio, μ , which defines the change in axial velocity over the blade row.

3.3.5. Vortex design

The vortex design method is used to control the radial variation of the swirl velocity component. For the fan stage, the vortex design method is part of the aerodynamic design module. After the calculations at the reference radius are completed, the velocity triangles at all radial stations between the hub and tip are determined using the selected vortex design method. For the low pressure compressor however, the blade heights are relatively small. Therefore the radial variations in the flow field are assumed to have little effect on the average stage performance. The average stage performance for the LPC is determined using a mean-line design method, in which the gas path through the mean-line of

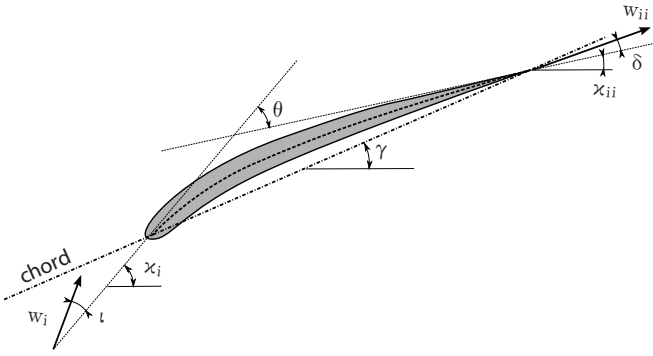


Figure 3.3: Fan blade angle nomenclature. Source: [5]

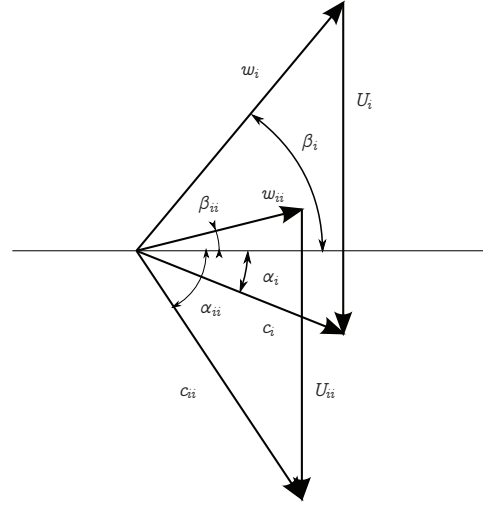


Figure 3.4: Velocity triangle nomenclature. Source: [5]

the component is considered to represent the average value in the compressor stage. It is a common used method in preliminary compressor design, and is proven to provide sufficient accuracy for the performance prediction in this design stage. A variety of blade vortex designs that are commonly used in compressor design are discussed below.

Free vortex design

The free vortex design method is the most simple and well-known method. Using this method, the work is distributed evenly along the blade span. The stage reaction however increases with radius, and for short compressor blades often results in highly twisted blade designs. The free vortex design method is described by equation (3.23).

$$C_\theta = \frac{a}{r} \quad (3.23)$$

Forced vortex design

The forced vortex design is rarely used, due to the unfavourable effect of a quadratic increasing work coefficient along the blade span. The governing equation for a forced vortex design is shown in equation (3.24).

$$C_\theta = ar \quad (3.24)$$

Constant reaction design

The constant reaction whirl distribution ensures that the blade reaction and work coefficients are constant along the blade span. Although this is a favourable property of the whirl distribution, it is prone to result in high twist angles. The constant reaction vortex design is defined before and after the rotor, by equations (3.25) and (3.26) respectively.

$$C_{\theta 1} = ar - \frac{b}{r} \quad (3.25)$$

$$C_{\theta 2} = ar + \frac{b}{r} \quad (3.26)$$

Exponential vortex design

In comparison to the free vortex design, the exponential vortex design has an extra constant which causes a variation of the blade reaction with radius. The exponential vortex design method is described before and after the rotor by equations (3.27) and (3.28) respectively.

$$C_{\theta 1} = a - \frac{b}{r} \quad (3.27)$$

Table 3.3: Special cases for general vortex design.

n	a	b	Special case
0			Exponential design
1			Constant reaction design
	0		Free vortex design
1		0	Forced vortex design

$$C_{\theta 2} = a + \frac{b}{r} \quad (3.28)$$

General vortex design

The general whirl distribution combines aspects of the free vortex design with an adjustable forced vortex distribution. Equations (3.29) and (3.30) describe the tangent velocity distribution before and after the rotor for the general vortex design respectively.

$$C_{\theta 1} = ar^n - \frac{b}{r} \quad (3.29)$$

$$C_{\theta 2} = ar^n + \frac{b}{r} \quad (3.30)$$

The vortex or swirl exponent, n , is used to control the shape of the radial whirl distribution. Table 3.3 show special cases of the general whirl distribution that occur at specific combinations of n , a and b .

3.3.6. Incidence angle

The incidence angle is defined as the difference between the inlet flow angle and the blade inlet metal angle. Several studies have shown that the cascade loss is dependent on the incidence angle, and at a certain angle, the optimum incidence angle, the cascade loss is minimal. Figure 3.5 shows the cascade loss “bucket” and the optimum incidence angle location.

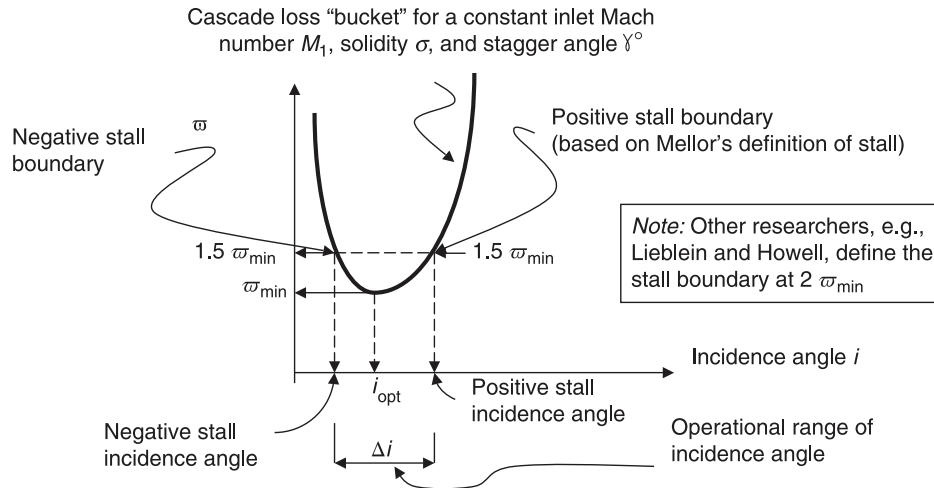


Figure 3.5: Optimum incidence angle and stall boundaries on the cascade loss curve. Source: [6]

There are several empirical methods available for optimum incidence angle calculations in cascade designs. To determine which method most accurately predicts the incidence angle in the considered operating conditions, five different methods are tested using experimental data available from rotor measurements at the NASA Lewis Research Center. Table 3.4 shows the data that has been used for validation.

The three methods by Aungier [77], Howell [78] and Johnsen & Bullock [79] respectively, are investigated here. Furthermore, Falck [8] presents in his work a set of equations, originally introduced by Howard, based on the original correlations from Johnsen & Bullock. Howard's method is also included in the analysis here.

Table 3.4: Experimental data used for validation of incidence angle and deviation angle prediction methods.

Designation	Pressure ratio [-]	Tip-speed [m/s]	Mass flow [kg/s]	Year	Reference
Rotor 35	1.82	455	20.2	1978	[68]
Rotor 36	1.82	455	20.2	1974	[69]
Rotor 37	2.05	454	20.2	1980	[70]
Rotor 51	1.15	243.8	29.9	1974	[71]
Rotor 52	1.25	257.7	34.9	1974	[72]
Rotor 53	1.35	302.8	32.7	1978	[73]
Rotor 55	1.20	213.3	31.2	1974	[74]
Rotor 57	1.38	289.6	29.6	1979	[75]
Rotor 67	1.59	428.9	33.3	1979	[76]

The validation data from the NASA rotors mentioned in table 3.4 consists of geometrical data and measurements of flow angles, velocities at different turning speeds. For the comparison of methods, the design operating conditions are used, and the error is defined as the absolute difference between the predicted and measured value. The combined results of the analysis are shown in figures 3.6 and 3.7.

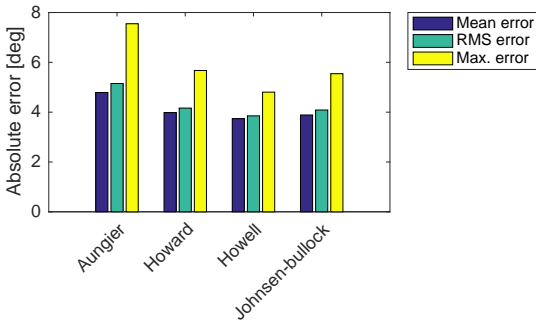


Figure 3.6: Comparison of rotor incidence angle prediction methods using NASA rotor data (table 3.4).

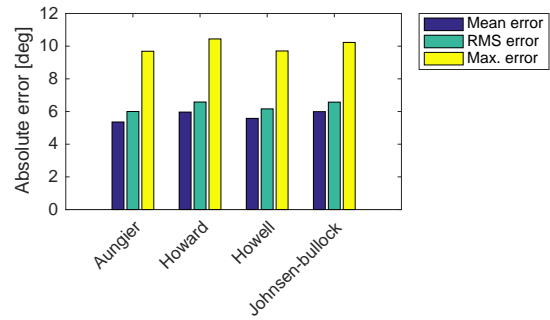


Figure 3.7: Comparison of stator incidence angle prediction methods using NASA rotor data (table 3.4).

Although Howell predicts the incidence angle more accurately for the rotor, the other methods show approximately the same results. The method that will be used to determine the minimum loss incidence angle method is the method by Aungier, as it has been used in Tournier [67] and resulted in accurate predictions when combined with the right deviation angle method, which is discussed next.

3.3.7. Deviation angle

The deviation angle is described by the difference between the trailing edge metal angle κ_2 and the relative exit flow angle β_2 . Ideally the flow over the blade cascade would perfectly follow the contours of the cascade such that no deviation angle would be present. However, due to pressure differences between the upper and lower surface of the airfoil the airflow is unable to stay attached to the surface and flow deviation occurs. The deviation angle gives an indication of the pressure loss in a stage and several empirical methods are available to predict the deviation angle based on flow conditions and cascade geometry. A total number of 9 deviation angle prediction methods is considered, and a similar comparison of techniques as for the incidence angle methods is performed here. The rotor data from table 3.4 is used here as well, and the results are shown in figures 3.8 and 3.9.

For both the rotor and stator, the deviation angle is best predicted using Johnsen and Bullock's method. This method, in combination with Aungier's method for the incidence angle, has been used in Tournier's work for determining the blade metal angles corresponding to the minimum loss in compressor cascades. Since the combined performance of these two methods has proven to deliver accurate predictions, these design methods are used here as well.

The iterative design methodology of determining the minimum loss blade metal angles based on the known air flow angles is shown in a flow diagram in figure 3.10.

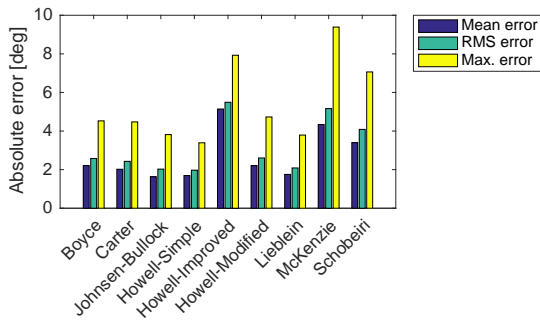


Figure 3.8: Comparison of rotor deviation angle prediction methods using NASA rotor data (table 3.4).

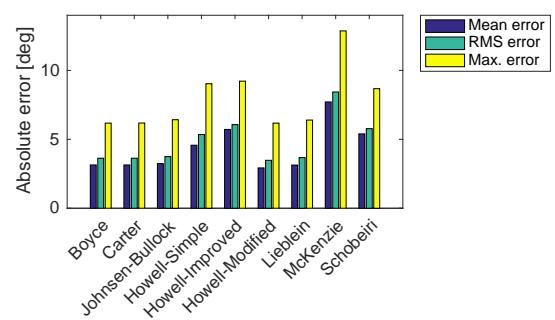


Figure 3.9: Comparison of stator deviation angle prediction methods using NASA rotor data (table 3.4).

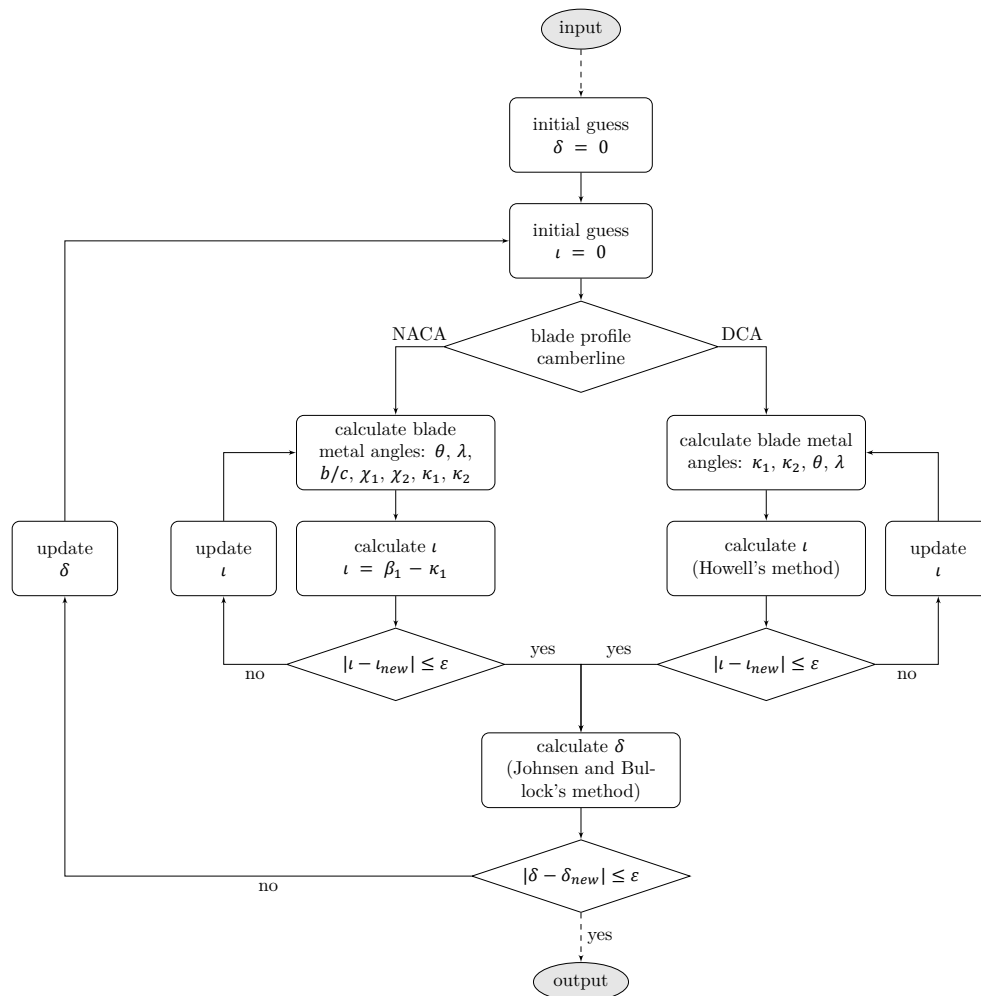


Figure 3.10: Iterative solving method for blade angles.

3.3.8. Loss sources

Now the flowfield over a cascade is properly defined, the analysis is extended to the three-dimensional domain. Complex flow fields develop inside the compressor stage due to the three-dimensional effects caused by rotating hardware. These effects are difficult to model, however, these flow phenomena should be taken into account to make a good estimate of the pressure loss in a compressor cascade. Figures 3.12 and 3.12 show some of the typical effects that occur in a compressor stage.

The basic sources of loss occurring in the fan stage are primary losses, secondary losses and shock losses. The primary losses are mainly caused by the blade profile, and capture the effects of momentum

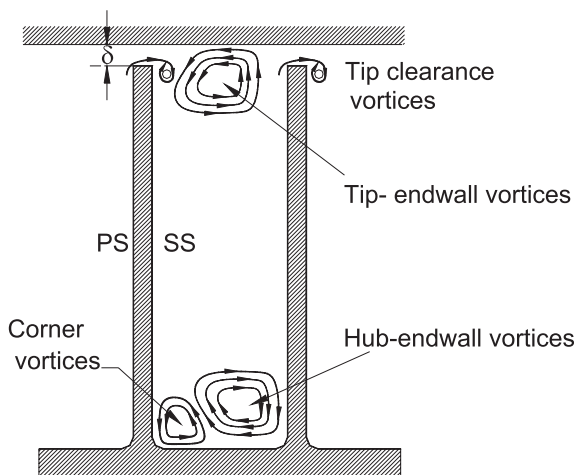


Figure 3.11: Development of tip, hub and endwall vortices in fan rotor and stator blade channels. *Source: [7]*

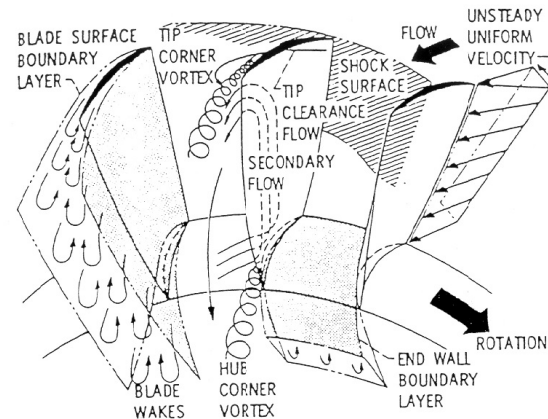


Figure 3.12: Flow fields in a compressor cascade with loss sources indicated. *Source: [8]*

loss over the blade, but also include losses resulting from induced drag. Secondary losses are caused by wall phenomena, such as the tip clearance, and are often referred to as endwall losses. Figure 3.11 shows the development of tip and hub endwall vortices, causing the secondary losses. Shock loss occur when the accelerating flow over the suction side of the fan blade exceeds the sonic limit. Using a loss model originally proposed by Lieblein et al. [80], all of these losses are incorporated in one loss factor, Z , from which the isentropic efficiency can be determined directly. The calculation of the fan cascade loss coefficient is explained in more detail in section 3.4.3.

In the LPC stage, the isentropic efficiency is determined by several loss models. Tournier & El-Genk [67] provide a well-documented summary of some of the latest loss models, and define the total loss coefficient as the sum of five different loss sources. The losses that are captured in the total loss coefficient are: profile loss w_{pro} , secondary losses w_{sec} , end-wall friction loss w_{end} , tip clearance losses w_{tc} and shock losses w_{shock} . From the total loss coefficient w , the ratio stagnation pressure loss over the dynamic inlet pressure can be calculated, and hence the total pressure loss in the stage can be determined. This method is elaborated upon in section 3.5.3.

3.4. Fan Analysis & Design

The aerodynamic performance analysis and design of the fan stage is treated in this section. The fan stage of a typical high bypass ratio turbofan engine is indicated in figure 3.13. The main purposes of the fan stage is to accelerate the bypass air to generate thrust, and increase the pressure ratio for the core inlet air. The fan stage consist of a rotor- and stator blade row. The rotor blade row is positioned in front of the engine, after which a splitter divides the airflow into a primary flow section, the core flow, and a secondary flow section, the bypass stream. The bypass stream only passes a stator blade row to remove the swirl velocity, which ideally produce an axial flowfield at the exit of the stator row. Then the air is expanded through the bypass nozzle generate a thrust force. The primary flow however, enters the low-pressure compressor stage via an inlet guide vane (IGV). It should be noted here that the stator vanes in the bypass duct are considered part of the fan design routine, while the IGV is designed using the LPC design routine.

First the design methodology used for the fan stage is explained in section 3.4.1. After that, the separate steps in the fan stage analysis and design process are treated, starting with the inlet calculations in section 3.4.2, followed by efficiency calculations using loss prediction models as explained in section 3.4.3.

3.4.1. Design methodology

The gas path analysis is carried out using a Blade Element Method (BEM) as described in section 3.3.1. The analysis of the fan stage consists of an iterative solving routine. Calculating the state after the rotor requires knowledge of the stage performance. However, as the stage performance is not yet

known, an initial guess is provided for the isentropic efficiency, η , and axial velocity ratio, μ . Later on in the calculation process the actual performance can be calculated, and values are compared to the initial guessed parameters. If the error is larger than a predefined error margin, a new performance value is guessed, and the calculation scheme is repeated until convergence of the parameters occurs. Table 3.5 provides a list of the input parameters that are required to solve the velocity triangle after the fan stage.

Table 3.5: Fan inlet input parameters.

Property	Symbol	Units
Mass flow	\dot{m}	kg/s
Angular velocity	Ω	rad/s
Fan face total pressure	$p_{t,1}$	Pa
Fan face total temperature	$T_{t,1}$	K
Fan face Mach number	M_1	-
Inlet angle	α_1	deg
Hub-to-tip ratio, LE	HTR_1	-
Hub-to-tip ratio, TE	HTR_2	-
Tip radius, LE	$r_{t,1}$	m
Tip radius, TE	$r_{t,2}$	m
Blade aspect ratio	AR	-
Blade solidity ratio	σ	-
Thickness-to-chord ratio	t/c	-
Max. chamber location	a/c	-
Vortex design swirl exponent	n	-
Blade tip gap	τ	m
Blade axial spacing	$F_{sp} = \Delta x/c$	-

With the pre-rotor velocity known and a given inlet flow angle, the inlet velocity triangle can be solved. The fan gas path is first analysed at the reference radius. The efficiency and pressure ratio at the reference radius are initially guessed. The temperature ratio can be determined from these two parameters using equation (3.5), and hence the flow properties after the rotor are known. Since the rotational speed of the rotor is known, the tangential velocities can be calculated and using the axial velocity ratio the entire velocity triangle at the reference radius can be constructed. Now using a defined vortex distribution as described in 3.3.5, the velocity triangles at all other radii are constructed.

With the entire velocity distribution known at all radii, the blade metal angles are calculated. Based

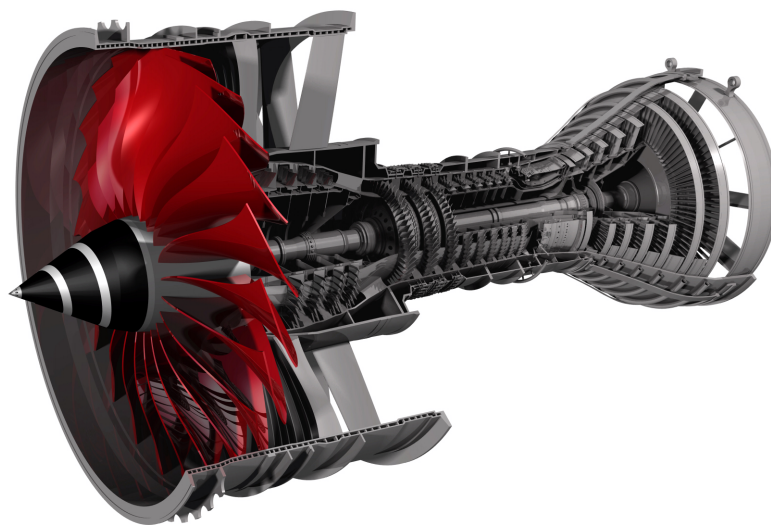


Figure 3.13: Fan stage. *Source: GrabCAD*

on the minimum loss cascade design method shown in figure 3.10, the blade metal angles are calculated. With the blade geometry and the flow field known, the pressure loss can be determined using the pressure loss prediction method described in section 3.4.3.

Now all information is available to check if the guessed axial velocity ratio, μ , is correct. Diéz showed that the a simple check using the continuity equation alone is not sufficient [5]. Hence, the radial equilibrium equation (3.3) is applied with the radial acceleration term neglected. As explained earlier, this results in a partial differential equation (PDE) which can then be rewritten in the form of an ordinary differential equation (ODE). The resulting ODE can be solved for the exit axial velocity term by applying the trapezoidal rule, resulting in equation (3.31)

$$C_{ax,2} = \sqrt{CF \cdot (F_1 + F_2 - F_3 - F_4 - F_5)} \quad (3.31)$$

Where the constants CF and F_i are given by equations (3.32) to (3.37) respectively.

$$CF = \frac{1}{1 - \frac{\kappa-1}{2\kappa} \ln \left[\frac{\left(\frac{T_t}{T_{t,ref}}\right)^{\frac{\kappa}{\kappa-1}}}{\left(\frac{p_t}{p_{t,ref}}\right)} \right]} \quad (3.32)$$

$$F_1 = C_{ax,2,ref}^2 \left(1 + \frac{\kappa-1}{2\kappa} \ln \left[\frac{\left(\frac{T_t}{T_{t,ref}}\right)^{\frac{\kappa}{\kappa-1}}}{\left(\frac{p_t}{p_{t,ref}}\right)} \right] \right) \quad (3.33)$$

$$F_2 = 2c_p(T_t - T_{t,ref}) \quad (3.34)$$

$$F_3 = (C_\theta^2 - C_{\theta,ref}^2) \quad (3.35)$$

$$F_4 = \left(\frac{C_\theta^2}{r} - \frac{C_{\theta,ref}^2}{r_{ref}} \right) (r - r_{ref}) \quad (3.36)$$

$$F_5 = \ln \left[\frac{\left(\frac{T_t}{T_{t,ref}}\right)^{\frac{\kappa}{\kappa-1}}}{\left(\frac{p_t}{p_{t,ref}}\right)} \right] \left[R(T_t + T_{t,ref}) - \frac{\kappa-1}{2\kappa} (C_\theta^2 + C_{\theta,ref}^2) \right] \quad (3.37)$$

Performance parameters such as pressure ratio, temperature ratio, and isentropic efficiency per radial section are then calculated. The weighted average of these performance parameters is used to determine the stage performance for the core and bypass sections of the fan blade, which are compared to their desired values after which the design input is altered accordingly. This process is repeated until the desired and calculated performance parameters converged.

3.4.2. Inlet calculations

The input to the fan design calculation process consists of the static air properties of the ambient, p_0 and T_0 , the mass flow ingestion \dot{m} , and the airspeed, either expressed by the axial Mach number, M_{ax} , or the axial velocity, C_{ax} . Assuming a fixed isentropic efficiency of the inlet, the total temperature and pressure at the fan rotor leading edge can be determined using equations (3.38) and (3.40) respectively.

$$T_{t,1} = T_0 + \frac{C_0^2}{2c_p} \quad (3.38)$$

$$= T_0 \left(1 + \frac{\kappa-1}{2} M_0^2 \right) \quad (3.39)$$

$$p_{t,1} = p_0 \left(1 + \eta_{is,in} \frac{C_0^2}{2c_p T_0} \right)^{\frac{\kappa}{\kappa-1}} \quad (3.40)$$

$$= p_0 \left(1 + \eta_{is,in} \frac{\kappa-1}{2} M_0^2 \right)^{\frac{\kappa}{\kappa-1}} \quad (3.41)$$

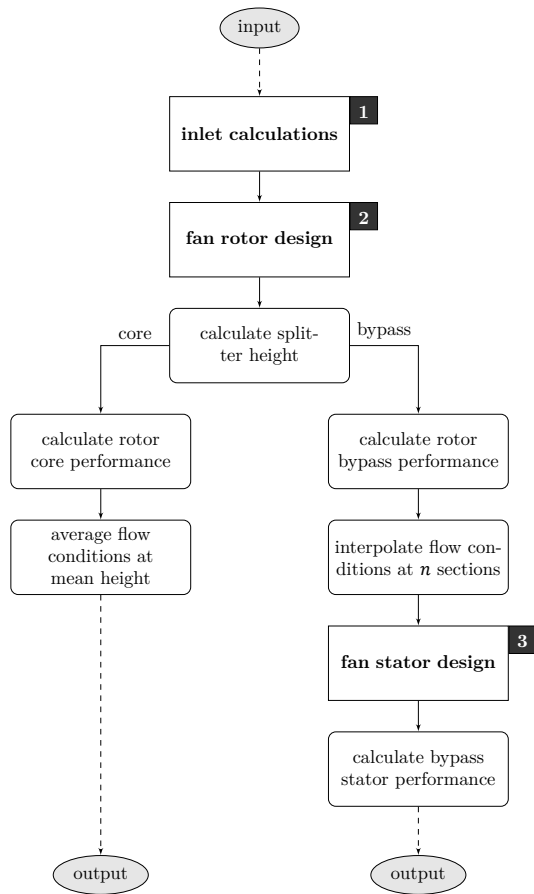


Figure 3.14: Fan design .

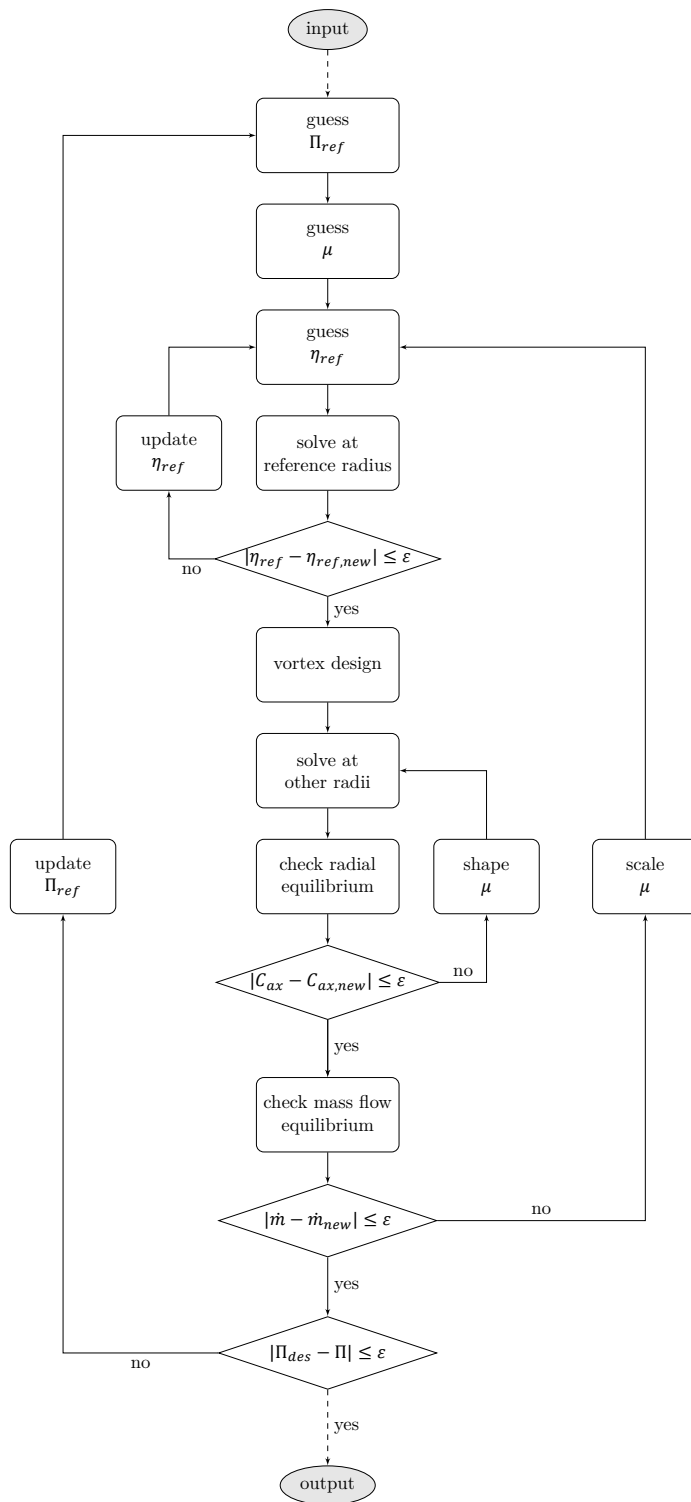


Figure 3.15: Iterative solving method for fan rotor design.

The static air properties are calculated using equations (3.7) and (3.8) respectively. However, to calculate the static properties at the rotor inlet, the axial velocity should be known. In the design case, the rotor inlet is designed for a certain axial inflow velocity, and the annulus area is determined these two inputs.

For the analysis case however, the annulus dimensions are known, but the axial velocity should be determined. An initial guess for the axial velocity is provided, and the static flow properties are calculated. The air density is calculated using equation (3.42).

$$\rho_1 = \frac{p_1}{RT_1} \quad (3.42)$$

The air density is then used to determine the mass flow rate at the rotor inlet using the continuity equation (3.1). If the mass flow rate is different from the provided operative condition, the axial speed is updated accordingly, and the calculation process is repeated until convergence of the flow parameters. Figure 3.16 shows the iterative solver scheme of determining the axial velocity at the rotor leading edge using the total flow conditions and the mass flow rate.

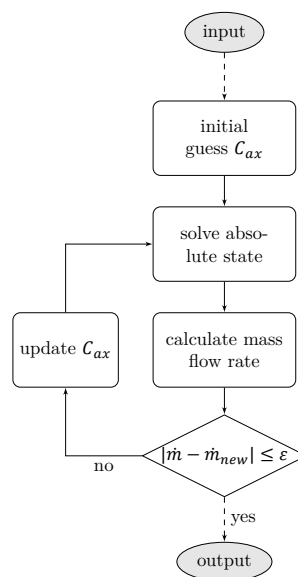


Figure 3.16: Iterative solving method for inlet axial velocity, C_{ax} .

It should be noted that the mass flow rate that is provided as input should be corrected for the given operating conditions. The corrected mass flow is given by equation (3.43).

$$w = \frac{\dot{m}\sqrt{\theta}}{\delta} \quad (3.43)$$

where $\theta = T_t/T_{ref}$ and $\delta = p_t/p_{ref}$ are correction factors for the current operating conditions in non-dimensional form. The reference values are taken at standard sea level conditions.

3.4.3. Pressure losses

The pressure losses encountered in the fan stage are estimated by loss correlations described in Schobeiri [81],[82],[7]. Schobeiri presents a method to predict the total loss in a fan or compressor stage including three main loss sources: the primary blade loss, shock loss and secondary losses. The primary blade loss is generated by flow interaction with the wall causing flow shear stress at the walls, and also includes trailing edge mixing losses. The shock losses resulting from transonic and supersonic relative inlet conditions are captured in the shock loss correction coefficient. Finally, secondary losses due to boundary layer development and tip clearance effects are captured by the secondary loss coefficient.

Loss coefficients

The profile and shock loss coefficients are both directly determined using correlations presented by Schobeiri [7]. Appendix A shows the correlation curves, which are both functions of the immersion ratio and diffusion parameter.

The immersion ratio, H , is the relative radial position from the blade tip as a function of the blade height. Hence, the immersion ratio is written as equation (3.44).

$$H = \frac{r_t - r}{r_t - r_h} \quad (3.44)$$

The flow diffusion is calculated using the modified diffusion parameter, D_m , as suggested by Schobeiri. The modified diffusion parameter takes the compressibility effects into account, and using the described angle definitions from figure 3.3, diffusion parameter is given by equation (3.45).

$$D_m = 1 - \mu \frac{\cos \beta_i}{\cos \beta_{ii}} + \frac{\nu \cos \beta_i}{\sigma(\nu + 1)} \left[\frac{\mu}{\nu \phi} (1 - \nu^2) + \tan \beta_i - \tan \beta_{ii} \right] \times \left[1 - \mu \frac{\cos \beta_i}{\cos \beta_{ii}} M_i^2 \left(\mu \frac{\cos \beta_i}{\cos \beta_{ii}} - 1 \right) \right] \quad (3.45)$$

Although the loss coefficients are determined from the correlation data, it is important to address the derivation of the profile loss coefficient here. The profile loss coefficient is defined as a function of the relative flow angles, β_1 and β_2 , blade solidity ratio, σ and the boundary layer momentum thickness, $\frac{\delta_2}{c}$, as shown in equation (3.46).

$$\zeta_p = \sigma \frac{\delta_2}{c} \left(\frac{\sin \beta_1}{\sin \beta_2} \right)^2 \cdot F(H_{12}, H_{32}, \frac{\delta_2}{c}, \sigma) \quad (3.46)$$

where the function F is a function of the above described parameters and the displacement and energy form factors, H_{12} and H_{32} respectively.

Correction factors

All correlations are based on experimental results with specific blade geometries and flow conditions. By making use of correction factors for Mach number, Reynolds number and blade thickness, these correlations can be applied to other flow conditions as well.

The Mach number correction should be applied when the Mach number locally reaches values of $M_R \geq 1.0$. Jansen and Moffatt [83] suggested that the total pressure loss increases rapidly after the maximum local flow velocity reaches values above a critical Mach number. The critical Mach number is given by equation (3.47).

$$\left(\frac{V_{max}}{V_1} \right)^2 - 1 = \frac{1 - \left(\frac{2}{\kappa+1} + \frac{\kappa-1}{\kappa+1} M_{1,cr}^2 \right)^{\frac{\kappa}{\kappa-1}}}{-1 + \left(1 + \frac{\kappa-1}{2} M_{1,cr}^2 \right)^{\frac{\kappa}{\kappa-1}}} \quad (3.47)$$

Davis [84] suggested a relation to directly determine the critical Mach from the maximum velocity ratio. The relation is given in equation (3.48) below.

$$M_{1,cr} = 2.925 - 2.948 \left(\frac{V_{max}}{V_1} \right) + 1.17 \left(\frac{V_{max}}{V_1} \right)^2 - 0.1614 \left(\frac{V_{max}}{V_1} \right)^3 \quad (3.48)$$

Now the profile loss coefficient is corrected using the critical Mach number by applying equation (3.49).

$$\zeta_{p,cor} = \zeta_p (A(M_1 - M_{1,cr}) + 1.0) \quad (3.49)$$

with $A = 1.8 - 2.0$ [85].

For pressure loss calculations at lower Reynolds numbers, the profile loss should be corrected accordingly. The profile loss correction applies only to a range of Reynolds number $Re < 2.5 \cdot 10^5$. The correction factor is given by equation (3.50).

$$\zeta_{p,cor} = \zeta_p \left(\frac{Re}{2.5 \cdot 10^5} \right)^{0.2} \quad (3.50)$$

At last, the blade thickness effect is considered by correcting the profile loss accordingly. A relation between the blade thickness and boundary layer momentum thickness is provided in Schobeiri [7].

While the profile loss is originally described by the boundary layer momentum thickness according to equation (3.46), the function F is often approximated to be a constant with a value of $F = 2$ [86]. This assumption is adopted here as well for the thickness correction, and hence the boundary layer momentum thickness is now directly proportional to the profile loss coefficient, $\frac{\delta_2}{c} \zeta_p$. Equation (3.51) shows the blade thickness correction applied on the profile loss coefficient.

$$\zeta_{p,cor} = \zeta_p \left(6.6 \frac{t}{c} + 0.34 \right) \quad (3.51)$$

3.5. LPC analysis & design

The low pressure compressor design is performed using a mean-line design method. The input to the compressor design problem are the weighted average flow properties from the inner fan stage. Figure 3.17 shows the location of the LPC stage in the turbofan engine.

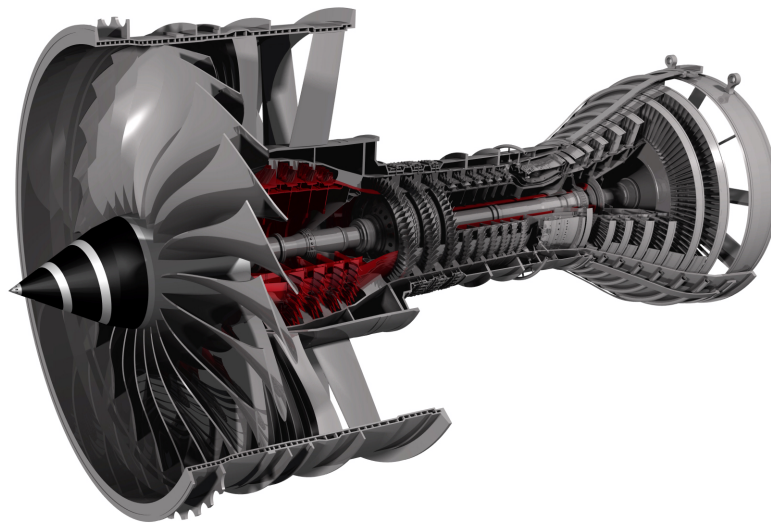


Figure 3.17: Low pressure compressor stage. *Source: GrabCAD*

The booster primarily serves to supercharge the high pressure compressor. Air enters the LPC through the inlet guide vane which directs the flow in a favourable direction for the first booster stage. The rotor stage accelerates the air to increase the kinetic energy. The kinetic energy is then translated into an increase in pressure by the stator vanes.

3.5.1. Design methodology

The low-pressure compressor is designed for a given design pressure ratio and degree of reaction, and using a minimal number of stages. The design process is again described by an iterative solver structure, which is controlled by the stage outflow angles α_3 , the stage loading parameter ψ and the number of stages n_{stages} . Initially, the design is tried with a low number of stages. A distribution of work through the compressor is defined by the stage loading coefficient. The first compressor stage is typically the highest loaded stage. Expressing the of the other stages relative to the work coefficient of the first stage, the last compressor stage operates at 80% of the the loading coefficient and the stages in between at 90% of the loading coefficient. Then the air outflow angles are guessed; the IGV has no flow deflection while the air outflow angles for all other stages are linearly decreasing to zero, since a zero-whirl exit condition is preferred. The stage calculations are performed, which determine the annulus dimensions and the cascade losses. After convergence of the stage calculation, first the achieved degree of reaction is checked with the initial guessed parameter. The outlet flow angles are updated if the values have not converged. If the degree of reaction of the stages is converged, the pressure ratio over the compressor is checked with the desired pressure ratio. If the achieved pressure ratio is not within the predefined error limit of the design pressure ratio, the loading coefficient is adjusted. A check with the maximum allowed loading coefficient ensures the new value is within the loading limit, otherwise the number of

compressor stages is increased. Figure 3.18 shows a schematic overview of the LPC component design procedure.

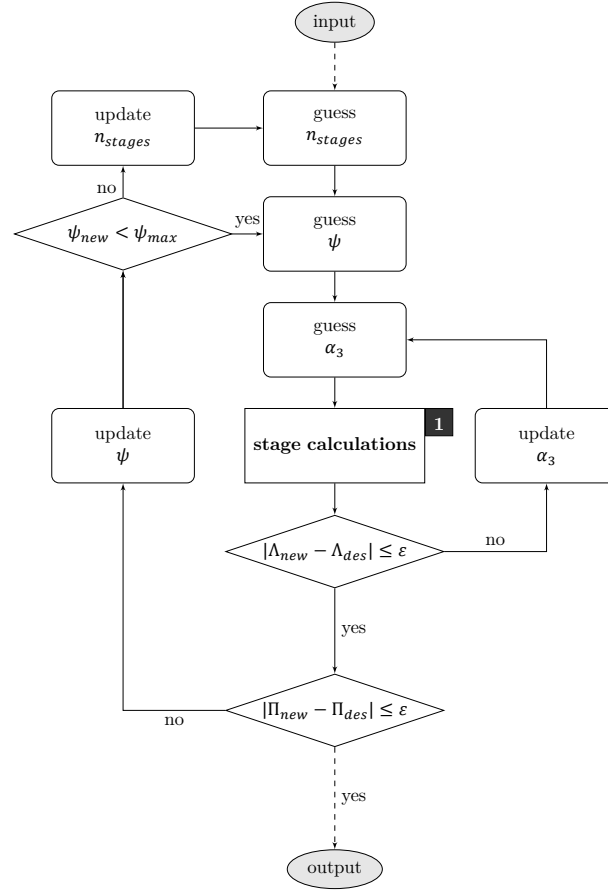


Figure 3.18: Low pressure compressor design map.

The compressor design routine is defined by numerous inputs. Most important are the total pressure ratio over the LPC component, the stage reaction and loading coefficients and the flow conditions at the compressor inlet. Furthermore, blade parameters for both rotor and stator blade rows are defined as fixed design parameters, and most are assumed to be linearly varying from hub to tip. Blade parameters include the blade shape, thickness-to-chord ratio, maximum camber location and taper ratio. An overview of typical LPC operating conditions is given in table 3.6.

3.5.2. Inlet calculations

In order to determine the required annulus cross-sectional area, first the flow conditions at the booster inlet should be calculated. The Mach number at the booster inlet is determined using the inlet specific flow, $(D/S)_{inlet}$, which is defined as the ratio of corrected mass flow over the annulus area, and is calculated using equation (3.52).

$$\left(\frac{D}{S}\right)_{inlet} = \frac{p_{01}}{\sqrt{T_{01}}} \cdot MFP \quad (3.52)$$

Where MFP is the mass flow parameter, which in term is given by equation (3.53).

$$MFP = \sqrt{\frac{\kappa}{R}} \cdot M_1 \cdot \left(1 + \frac{\kappa - 1}{2} \cdot M_1^2\right)^{\frac{\kappa + 1}{2 \cdot (1 - \kappa)}} \quad (3.53)$$

According to Mattingly [31], for the fan and LPC stage inlet, the inlet specific mass flow is typically between 195 and 205 $kg/(m \cdot s)$. Figure 3.19 shows the inlet specific flow parameter as a function of Mach number. It can be seen that the limited range of inlet specific flow results in an inlet Mach number

Table 3.6: LPC inlet input parameters.

Property	Symbol	Units
Design pressure ratio	PR_{des}	-
Number of stages	n_{stages}	-
Mass flow	\dot{m}	kg/s
Angular velocity	Ω	rad/s
Inlet total pressure	$p_{t,1}$	Pa
Inlet total temperature	$T_{t,1}$	K
Inlet Mach number	M_1	-
Inlet flow angle	α_1	deg
Hub-to-tip ratio, LE	HTR_1	-
Tip radius, LE	$r_{t,1}$	m
Blade aspect ratio	AR	-
Blade solidity ratio	σ	-
Thickness-to-chord ratio	t/c	-
Max. chamber location	a/c	-
Blade tip gap	τ	m
Blade axial spacing	$F_{sp} = \Delta x/c$	-

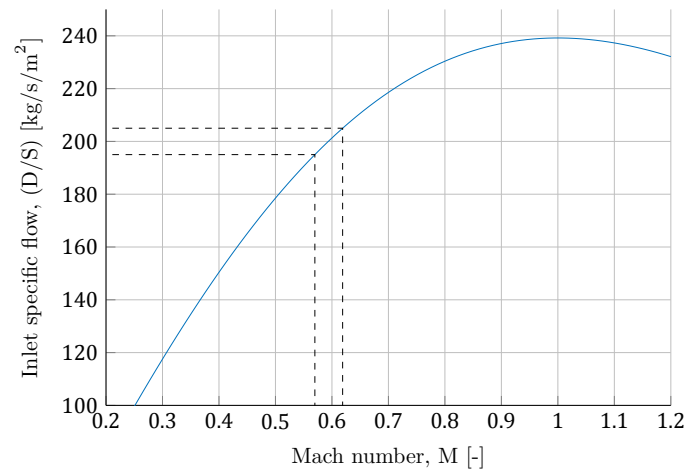


Figure 3.19: Inlet specific flow vs. Mach number with typical LPC inlet conditions indicated.

range of 0.55 to 0.65 approximately. Using the mass flow parameter, the cross-sectional annulus area at the LPC inlet can be calculated using equation (3.54):

$$A_1 = \frac{\dot{m} \cdot \sqrt{T_{01}}}{MFP_1 \cdot p_{01} \cdot \cos \alpha_1} = \pi \cdot (r_{t,1}^2 - r_{h,1}^2) \quad (3.54)$$

The hub-to-tip radius ratio, (r_h/r_t) , is an input parameter and is lower limited due to problems with the radial velocity distribution with low values for (r_h/r_t) . A typically used lower limit for the hub-to-tip ratio is 0.4. [87] [31]

3.5.3. Pressure losses

The LPC isentropic efficiency is determined by several loss models. Tournier & El-Genk [67] provide an overview of empirical methods used to determine the losses in a compressor cascade based on five loss sources: profile loss w_{pro} , secondary losses w_{sec} , endwall friction losses w_{end} , tip clearance losses w_{tc} and shock losses w_{shock} . The total loss coefficient is then computed using equation (3.55).

$$w = w_{pro} + w_{sec} + w_{end} + w_{tc} + w_{shock} \quad (3.55)$$

From the total loss parameter w , the ratio of loss in stagnation pressure over the dynamic inlet pressure can be calculated, using equation (3.56).

$$w = \frac{\Delta p_t}{p_{t,1} - p_1} \quad (3.56)$$

The computation of the five loss sources is treated separately in the following sections.

Profile loss

The blade profile pressure loss coefficient is described by Lieblein [88] as:

$$w_{pro} = 2 \left(\frac{\theta_2}{c} \right) \frac{\sigma}{\cos \beta_2} \left(\frac{\cos \beta_1}{\cos \beta_2} \right)^2 \left(\frac{2H_{TE}}{3H_{TE} - 1} \right) \left[1 - \left(\frac{\sigma_2}{c} \right) \frac{\sigma H_{TE}}{\cos \beta_2} \right]^{-3} \quad (3.57)$$

Where θ_2 is the momentum thickness of the boundary layer at the blade outlet, and in the dimensionless form it is given as

$$\frac{\theta_2}{c} = \left(\frac{\theta_2^0}{c} \right) \cdot \zeta_M \cdot \zeta_H \cdot \zeta_{Re} \quad (3.58)$$

Furthermore, H_{TE} is the boundary layer trailing edge shape factor, which represents the ratio of boundary layer displacement thickness to the boundary layer momentum thickness. The boundary layer trailing edge shape factor is given as

$$H_{TE} = H_{TE}^0 \cdot \xi_M \cdot \xi_H \cdot \xi_{Re} \quad (3.59)$$

The values of θ_2^0 and H_{TE}^0 refer to the nominal conditions of inlet Mach numbers, $Ma_1 < 0.05$, no height contraction, H , due to reduced annulus flow area, an inlet Reynolds number of $Re_{1c} = 10^6$ and hydraulically smooth blades. Koch & Smith [89] presented accurate correlations for the boundary layer momentum thickness and the boundary layer trailing edge shape factor for the described nominal flow conditions, which are given by the following equations respectively.

$$\frac{\theta_2^0}{c} = 2.644 \cdot 10^{-3} D_{eq} - 1.519 \cdot 10^{-4} + \frac{6.713 \cdot 10^{-3}}{2.60 - D_{eq}} \quad (3.60)$$

$$\begin{aligned} H_{TE}^0 &= \frac{\delta_{TE}^*}{\theta_2^0} \\ &= (0.91 + 0.35 D_{eq}) \{ 1 + 0.48 (D_{eq} - 1)^4 + 0.21 (D_{eq} - 1)^6 \} \end{aligned} \quad (3.61)$$

When $D_{eq} > 2.0$ a value of $H_{TE}^0 = 2.7209$ is used. Apart from the nominal conditions, Koch & Smith also developed correlations for the correction factors from equations (3.58) and (3.59) respectively. First, the correction factors of Mach number ζ_M , contraction ratio ζ_H and Reynold's number ζ_{Re} are provided

for the momentum thickness equation. For the inlet Mach number correction factor, ζ_M , the following correlation is provided

$$\zeta_M = 1.0 + (0.11757 - 0.16983D_{eq})M_1^n \quad (3.62)$$

Where the power term n is given by

$$n = 2.853 + D_{eq}(-0.97747 + 0.19477D_{eq}) \quad (3.63)$$

The correlation of the correction factor for the flow area contraction is given by

$$\zeta_H = 0.53 \frac{H_1}{H_2} + 0.47 \quad (3.64)$$

The Reynolds correction factor is well approximated by Aungier [90], who introduced the critical blade chord Reynolds number above which the effect of roughness becomes significant, which is determined by $Re_{cr} = \frac{100c}{\kappa}$. The correlation is given for two cases. When $Re_{1c} < Re_{cr}$ the Reynolds correction factor is determined by

$$\zeta_{Re} = \begin{cases} \left(\frac{10^6}{Re_{1c}}\right)^{0.166} & \text{for } Re_{1c} \leq 2 \cdot 10^5 \\ 1.30626 \left(\frac{2 \cdot 10^5}{Re_{1c}}\right)^{0.5} & \text{for } Re_{1c} < 2 \cdot 10^5 \end{cases} \quad (3.65)$$

However, above the critical blade chord Reynolds number the friction losses are dominated by the surface roughness. Therefore, if $Re_{1c} > Re_{cr}$, the Reynolds correction factor is given by

$$\zeta_{Re} = \begin{cases} \left(\frac{10^6}{Re_{cr}}\right)^{0.166} & \text{for } Re_{cr} \leq 2 \cdot 10^5 \\ 1.30626 \left(\frac{2 \cdot 10^5}{Re_{cr}}\right)^{0.5} & \text{for } Re_{cr} < 2 \cdot 10^5 \end{cases} \quad (3.66)$$

It should be noted that typical values of the blade chord to surface roughness are in the range of $c/\kappa = 10000 - 20000$.

For the form factor equation, the correction factors for Mach number ξ_M , contraction ratio ξ_H and Reynold's number ξ_{Re} are now considered. The Mach number correction is described by

$$\xi_M = 1.0 + [1.0725 + D_{eq} \cdot (-0.8671 + 0.18043 \cdot D_{eq})] \cdot M_1^{1.8} \quad (3.67)$$

The flow area contraction ratio correction factor is given by

$$\xi_H = 1.0 + \left(\frac{H_1}{H_2} - 1.0\right)(0.0026 \cdot D_{eq}^8 - 0.024) \quad (3.68)$$

The inlet Reynold's number correction factor is again given for two cases

$$\xi_{Re} = \begin{cases} \left(\frac{10^6}{Re_{1c}}\right)^{0.06} & \text{for } Re_{1c} < Re_{cr} \\ \left(\frac{10^6}{Re_{cr}}\right)^{0.06} & \text{for } Re_{1c} \geq Re_{cr} \end{cases} \quad (3.69)$$

The equivalent diffusion ratio, D_{eq} , which is referred to in several of the above equations, is described by Koch & Smith [89] as

$$D_{eq} = \frac{V_{1R}}{V_{2R}} \left[1 + K_3 \cdot \frac{t_{max}}{c} + K_4 \cdot \Gamma^* \right] \cdot \sqrt{(\sin \beta_1 - K_1 \sigma \Gamma^*)^2 + \left(\frac{\cos \beta_1}{A_{throat}^* \cdot \rho_{throat} / \rho_1} \right)} \quad (3.70)$$

Where the throat area contraction ratio, A_{throat}^* , is given as

$$A_{throat}^* = \left[1.0 - \frac{K_2 \sigma \left(\frac{t_{max}}{c} \right)}{\cos \left(\frac{\beta_1 + \beta_2}{2} \right)} \right] \cdot \frac{A_{throat}}{A_1} \quad (3.71)$$

With the assumption that the cascade throat area occurs at one-third of the axial chord, the cascade throat area A_{throat} equals

$$A_{throat} = A_1 - \frac{A_1 - A_2}{3} \quad (3.72)$$

Another term mentioned in the equivalent diffusion ratio equation ((3.70)) is the ratio of gas density in the throat to the ambient gas density, ρ_{throat}/ρ_1 , which is obtained by

$$\frac{\rho_{throat}}{\rho_1} = 1 - \frac{M_{x1}^2}{1 - M_{x1}^2} \left(1 - A_{throat}^* - K_1 \sigma \Gamma^* \frac{\tan \beta_1}{\cos \beta_1} \right) \quad (3.73)$$

Where the constants mentioned in these equations are determined from experimental data by Koch & Smith, and are presented in table 3.7.

Table 3.7: Constants K_i as mentioned in the diffusion factor calculations

Parameter	Value
K_1	0.2445
K_2	0.4458
K_3	0.7688
K_4	0.6024

The dimensionless blade circulation parameter, Γ^* , is given by

$$\begin{aligned} \Gamma^* &= \frac{r_{1m} \cdot v_1 - r_{2m} \cdot v_2}{\sigma V_1 \cdot (r_{1m} + r_{2m})/2} \\ &= (\tan \beta_1 - \tan \beta_2) \cdot \frac{\cos \beta_1}{\sigma} \end{aligned} \quad (3.74)$$

Since it is assumed that $r_{1m} = r_{2m} = r_m$, the rotational speeds are also equal: $U_{1m} = U_{2m} = U_m$. Hence, the equation simplifies to the last line of equation (3.74).

Secondary losses

The secondary losses describe another major part of the total losses in the LPC stage. The nature of this loss has elaborated upon in section 3.4.3, and is visualised in figure 3.11. For the LPC stage, the following correlation for the secondary flow loss coefficient has been proposed by Howell [78]:

$$w_{sec} = 0.018 \cdot \sigma \cdot \frac{\cos^2 \beta_1}{\cos^3 \beta_m} \cdot C_L^2 \quad (3.75)$$

Where C_L is the compressor blade lift coefficient, and is described by

$$C_L = \frac{2}{\sigma} \cdot \cos \beta_m \cdot [\tan \beta_1 - \tan \beta_2] \quad (3.76)$$

And the mean velocity angle, β_m , is given as

$$\tan \beta_m = \frac{\tan \beta_1 + \tan \beta_2}{2} \quad (3.77)$$

Endwall friction losses

The endwall loss coefficient has been well correlated by Aungier [77] based on a modified model of Howell [78]. The expression for the enwall loss coefficient is given by Aungier as:

$$w_{end} = 0.0146 \cdot \frac{c}{h} \cdot \left(\frac{\cos \beta_1}{\cos \beta_2} \right)^2 \quad (3.78)$$

Tip clearance loss

Yaras & Sjolander [91] proposed a prediction method for the tip-leakage loss factor, w_{tc} , which is split up in three losses: secondary losses, tip leakage losses and gap losses. As the secondary losses have already been treated, only the tip-leakage loss and gap loss are discussed here, hence:

$$w_{tc} = w_{tip} + w_{gap} \quad (3.79)$$

Yaras & Sjolander present the following correlations for the tip and gap losses:

$$w_{tip} = 1.4K_E\sigma \cdot \frac{\tau}{h} \cdot \frac{\cos^2 \beta_1}{\cos^3 \beta_m} \cdot C_L^{1.5} \quad (3.80)$$

$$w_{gap} = 0.0049K_G\sigma \cdot \frac{c}{h} \cdot \left(\sqrt{C_L}/\cos \beta_m\right) \quad (3.81)$$

Where τ is the blades tip clearance gap and the h blade height. The constants are given by $K_E = 0.5$ and $K_G = 1.0$ for mid-loaded compressor blades. For front- or aft-loaded blades the constants are $K_E = 0.566$ and $K_G = 0.943$.

Shock loss

The shock loss is not always present in the LPC stage, but if the blade tip velocity of a stage reaches $M_{1R} > 1$, the shock loss should be taken into account. Koch & Smith [89] presented a figure with calculated shock loss coefficients for several high-speed fan stages. A correlation between the Mach number and the shock loss coefficient has been based on this figure by Boorsma [19].

$$w_{shock} = 0.375 - 0.75 \cdot M_{1R} + 0.375 \cdot M_{1R}^2 \quad (3.82)$$

Boorsma also indicates that since the first compressor stages often have a low hub-to-tip ratio, the radial variation in Mach number becomes significant. As the shock loss coefficient rapidly increase with Mach number, a weighted average is taken from the Mach number at blade mean radius and the Mach number at the blade tip, to better predict the total shock loss effect.

$$M_{1R,shock} = M_{1R,mean} + 0.9 \cdot (M_{1R,tip} - M_{1R,mean}) \quad (3.83)$$

4

Structural analysis & Weight

Components of gas turbine engines get exposed to extreme loading conditions. In this chapter, the different design challenges that are encountered during the conceptual engine design phase are discussed. In section 4.1 the materials considered in for the fan and low pressure compressor stages evaluated and the selection process is explained. After that, the fatigue design methodology is elaborated upon in section 4.2. The structural design considerations of each individual component are treated in separate sections. First, a short section 4.3 is dedicated to the design of the structural design of the blades and the weight estimation of the component. The rotating blades in a rotor blade row are held in place by a rotating disk, which carries the load of the resulting outwards centrifugal force of the blade. Section 4.4 gives a detailed insight in the disk design methods and optimization procedures that are used in this thesis. Pressure containment and blade release are two important criteria for the design of fan and compressor casing, which is elaborated upon in section 4.5. The design of the low pressure spool driving the compressor and fan stages is considered in section 4.6, and finally in section 4.7 the spinner cone calculation process is elaborated upon. It should be noticed that the connecting hardware and load carrying components are not designed with this tool.

4.1. Materials

Material selection in gas turbine engine design is an import aspect of the design process, as the operational environment of the engine components is highly demanding. The most extreme loading conditions are found at the first HPT stage, just after the combustion chamber. Here, gas temperatures can reach values up to 700K in excess of the material melting point [29]. Since the HPT is connected to the high pressure spool, high rotational velocities are resulting in large mechanical stresses due to centrifugal effects. On top of that, in aerospace applications component weight is also an important factor. In combination with the mechanical and thermal loads on the engine components this results in the requirement of advanced, light-weight materials with outstanding mechanical properties. Favourable material properties are often expressed in density fractions, such as the specific strength, $\frac{\sigma_{UTS}}{\rho}$ and specific stiffness, $\frac{E}{\rho}$. Although the "hot section" of the gas turbine is not considered in this thesis assignment, it is assumed that the low pressure compressor uses the same material for its casing. This is due to the fact that the LPC and HPC casing are made of one piece, and hence it is designed for the most extreme operating conditions. At the final HPC stage high pressures and elevated temperatures occur, and therefore the LPC casing material should be able to withstand high temperatures and have high specific strength characteristics. Table 4.1 shows an overview of basic material properties of some commonly used materials in aeroengine design. In the T-AXI Disk software a database of materials is present, which is directly adopted in the Matlab engine design and sizing tool. Figure 4.1 shows the temperature dependency of the material strength properties of the three most common fan and compressor design materials. Similar trends of decreasing properties with increased temperature are found for the Young's Modulus of the material as well.

Table 4.1: Aeroengine material properties. *Source: [19–21]*

Material	ρ [kg/m^3]	E [GPa]	σ_U [MPa]	σ_Y [MPa]	ν [-]	T_{max} [K]	α [K^{-1}]	RA [%]
Ti-6Al-4V	4430	113.8	950	880	0.34	550	$9 \cdot 10^{-6}$	25
Ti-17	4650	115	1185	1140	0.33	–	$8.5 \cdot 10^{-6}$	25
Inconel-718	8190	179	1100	980	0.32	980	$13 \cdot 10^{-6}$	18
Rene-41	8249	188	1400	1014	0.32	1255	$13.5 \cdot 10^{-6}$	25
Haynes 188	8980	205	243	131	-	1400	$18.5 \cdot 10^{-6}$	13

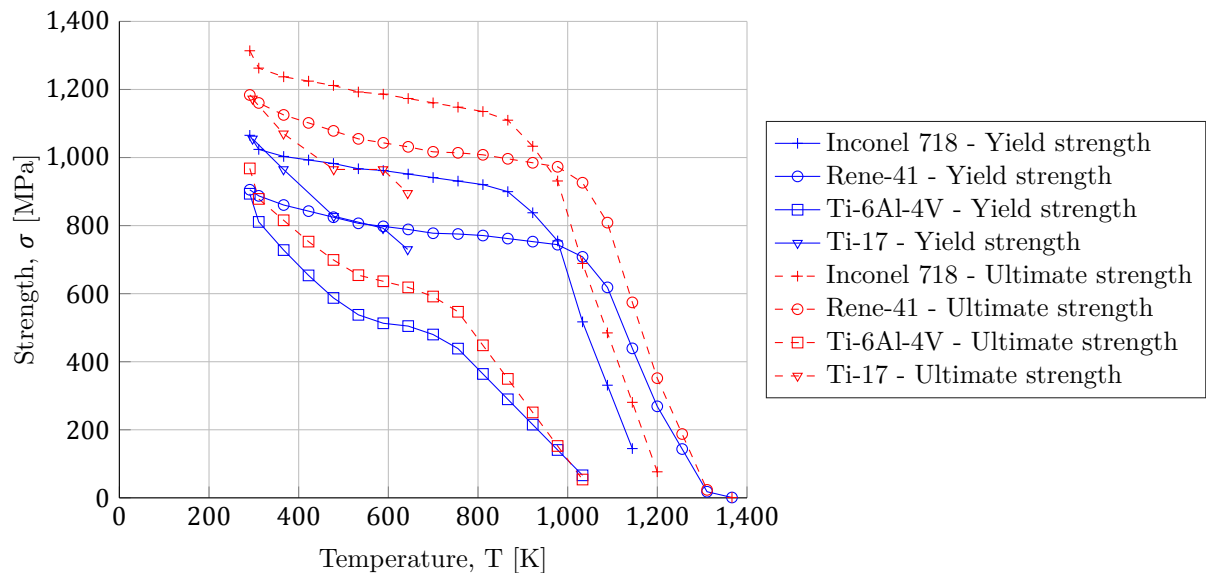


Figure 4.1: Temperature effect on yield and ultimate strength.

4.2. Fatigue life

The structural analysis of the engine components is extended by incorporating material fatigue effects in the calculations. The fatigue life of a component is determined by a number of load cycles until failure. Components are designed for a predefined number of design load cycles (N_{des}), and at the end of the component life the maximum stress values in the material multiplied by a fatigue safety factor should be within the lower than the defined stress limits.

First the general aspects of fatigue loading and design limits are explained in the design methodology section 4.2.1. After that, the method of estimating the stress-life curve of a component is elaborated upon in section 4.2.2.

4.2.1. Design methodology

The fatigue life of a component is dependent on many different factors, such as the material used, loading of the component, component geometry and surface finishing. Loading of the component is defined by the type of loading and the load cycle profile. The loading types considered in the fatigue design method described here are axial loading, torsion and bending. A load cycle can be defined by two main properties: maximum stress, σ_{max} , and the stress ratio, $R = \frac{\sigma_{min}}{\sigma_{max}}$. Other important values can be determined from those, such as the minimum stress, σ_{min} , the mean stress, σ_m , and stress amplitude, σ_A . Figure 4.2 shows some typical load cycles indicating the important stress levels for a stress ratio of $R = 0.1$.

Common used load cycles are the fully reversed cyclic loading ($R = -1$), the repeated stress cycle ($R = 0$) and elevated mean stress cyclic loading ($R = 0.1$). The latter is often used for testing of aerospace structures. However, for stress cycle analysis in engines it is more convenient to use a stress ratio of $R = 0$, as the maximum stresses are repeatedly present during engine operation, and stresses are absent when the engine is not operational.

Determining the minimum required thickness for fatigue design of the separate components is done

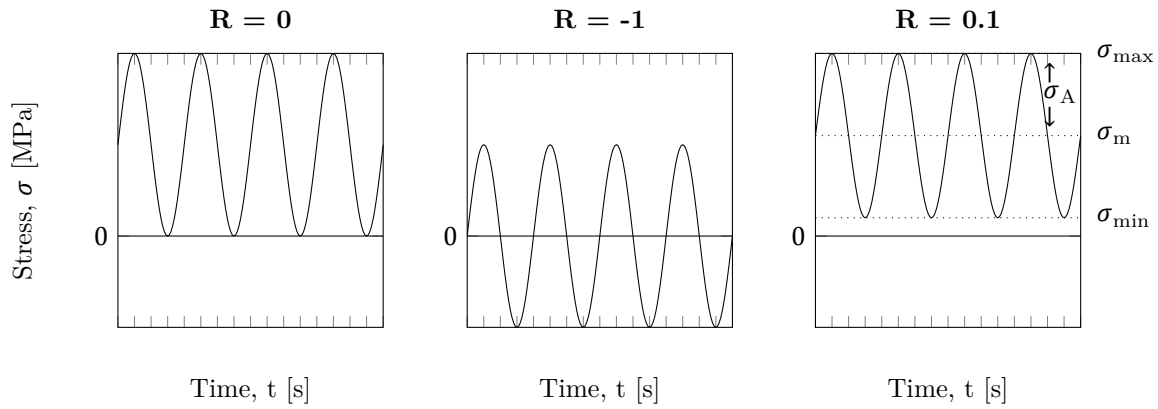


Figure 4.2: Stress amplitude ratio.

using an iterative solving procedure. First the component endurance limit, S_e , is calculated for the design number of load cycles. The endurance limit is determined by estimation of the stress-life (S-N) curve, using a method described in Lee [9]. The estimated S-N curve method accurately predicts the effects of fatigue loading on the component strength, and the implications of the method are briefly discussed in section 4.2.2. After the endurance limit is determined, the component thickness is calculated for the maximum static stress loading and an initial static safety factor is applied. The static stress analysis for each component are discussed in sections 4.3 to 4.6 respectively. Now the margin of safety in the fatigue domain is determined using the Goodman diagram. Several other methods are available to determine the fatigue safety factor as shown in figure 4.3. Goodman’s method is used here to describe the safety margin of the design, as it is a conservative method that is widely used in fatigue design.

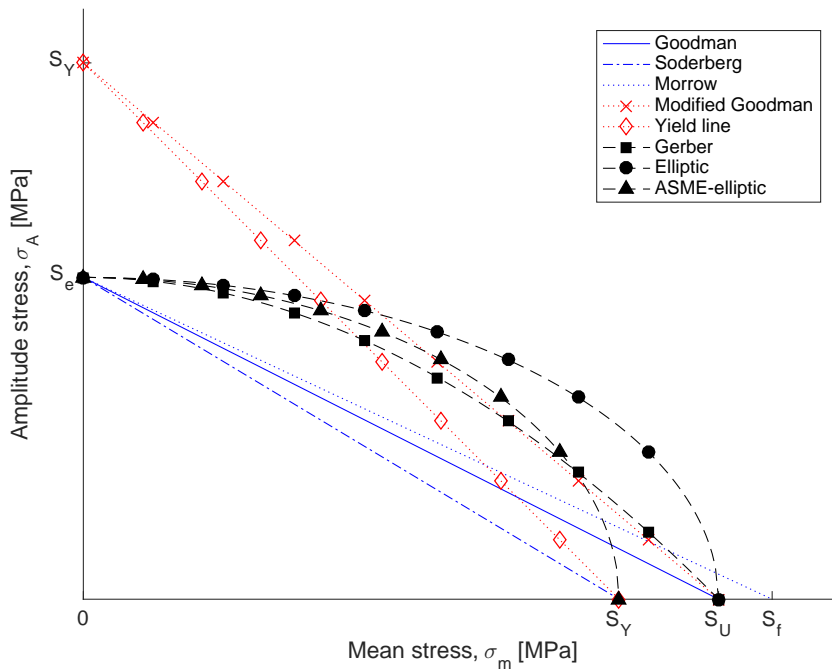


Figure 4.3: Fatigue safety margin methods.

The yield line is a straight line from the material yield value on the mean stress (vertical) axis to the yield value on the amplitude stress (horizontal) axis. The Goodman line is defined by equation (4.1).

$$\frac{\sigma_A}{S_e} + \frac{\sigma_m}{S_U} = 1 \tag{4.1}$$

Since the stress amplitude and mean stress are known, the current design point location, (σ_m, σ_A) , on

the figure is also known. The fatigue loading safety margin is then determined by equation (4.2).

$$SF_{GM} = \frac{L_{DP} + L_{GM}}{L_{DP}} \quad (4.2)$$

Where L_{DP} is the distance from the origin to the current design point, and L_{GM} is the shortest distance from the design point to Goodman line. In a similar fashion the safety factor of the yield line is determined. The desired value is then compared to the current smallest safety factor, and a new guess for the static safety factor is made. This iterative procedure is used for the fatigue design of all parts except for disk fatigue life prediction. The disk life is approximated using a different method, which is further explained in section 4.4.

4.2.2. Estimated stress-life

Stress-life curves describe the decrease in component failure strength as a result of the number of load cycles applied on the component. Based on extensive destructive load cycle testing, S-N curves are developed. However, there are many factors that have effect on the failure strength of a component, and a different stress-life cycle should be determined for each case. Since testing is an expensive and time-consuming process, methods have been developed to estimate the S-N curves. A quick method of estimating the stress-life curve of a component based on the material ultimate strength is presented by Lee [9].

A typical stress-life (S-N) curve of an arbitrary steel component is shown in figure 4.4. It can be seen that the fatigue life of a component is dependent on several factors, such as the material used, the loading conditions, geometry, surface finishing. The method uses correction factors to compensate for these effects.

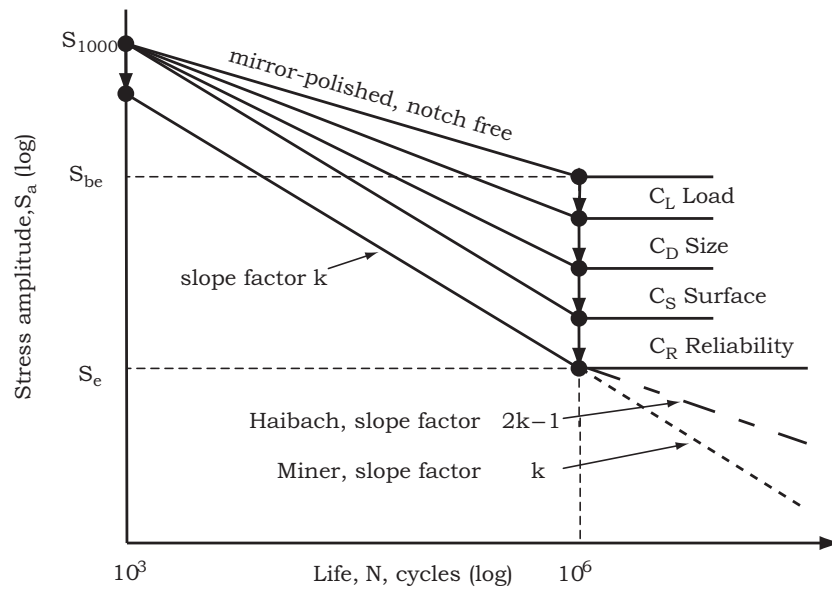


Figure 4.4: Modified S-N curves for steel component. Source: [9]

In the method, the baseline fatigue strength at 10^3 cycles, S_{1000} , is determined based on the ultimate tensile strength and depending on material type and type of loading. The loading type itself is also of great influence on the shape of the S-N curve, the effect of which is captured in the loading correction factor, C_L . Table 4.2 gives an overview of the the baseline fatigue strength and loading factor, based on the material and loading conditions, while the reliability correction factor is presented in table 4.3.

Due to the random nature of the fatigue life of components, non-destructive testing data usually are scattered. A reliability correction factor, C_R , is introduced to incorporate this statistical effect of the distributed results on the S-N curve. Table 4.4 shows the suggested values of the correction factor for different reliability levels.

From figure 4.4 it can be seen that after a certain number of cycles, the fatigue properties do not decrease anymore. This is called the fatigue limit, and the uncorrected baseline of the fatigue limit is determined by the bending fatigue limit as shown in table 4.4.

Table 4.2: Baseline fatigue strength, S_{1000} , and loading factor, C_L , based on the material and loading conditions.

Loading	Material	S_{1000}	C_L
Bending	All	$0.90 \cdot S_U$	1.0
Axial	All	$0.75 \cdot S_U$	0.9
Axial+Bending	All	$0.75 \cdot S_U$	0.7
Torsion	Steel	$0.72 \cdot S_U$	0.58
Torsion	Nonferrous	$0.63 \cdot S_U$	0.58
Torsion	Cast iron	$1.17 \cdot S_U$	0.8

Table 4.3: Reliability factor, C_R

Reliability	C_R
0.50	1.000
0.90	0.897
0.95	0.868
0.99	0.814
0.999	0.753
0.9999	0.702
0.99999	0.659
0.999999	0.620

Table 4.4: Baseline bending fatigue limit, S_{be} , and cycle limit, N_{be}

Material	S_{be}	N_{be}	
Steel	$0.5 \cdot S_U$	10^6	$S_U < 1400MPa$
Steel	$700MPa$	10^6	$S_U \geq 1400MPa$
Cast iron	$0.4 \cdot S_U$	$5 \cdot 10^7$	
Nonferrous	$0.4 \cdot S_U$	$5 \cdot 10^8$	$S_U < 336MPa$
Nonferrous	$130MPa$	$5 \cdot 10^8$	$S_U \geq 336MPa$

The size factor, C_D , is used to correct for different specimen sizes of the component, and is defined by equation (4.3).

$$C_D = \begin{cases} 1.0 & \text{for } d < 8\text{mm} \\ 1.189d^{-0.097} & \text{for } 8\text{mm} < d < 250\text{mm} \end{cases} \quad (4.3)$$

The last correction factor is the surface finishing factor, C_S . All engine components are assumed to be well polished and hence the surface finishing correction factor is fixed at $C_S = 1.0$.

Finally, the corrected fatigue limit, S_e , can be estimated by multiplying the baseline bending fatigue limit with all correction factors, which results in equation (4.4).

$$S_e = S_{be} C_L C_S C_D C_R \quad (4.4)$$

Now the slope of the line can be determined using the logarithmic difference of the corrected fatigue strength at 10^3 cycles, $S_{1000,R} = S_{1000} C_R$, and the corrected fatigue limit, S_e , according to equation (4.5).

$$k = -\frac{\log(10^3) - \log(N_{be})}{\log(S_{1000}) - \log(S_{be})} \quad (4.5)$$

The stress at any point on this line is then determined by equation (4.6).

$$N_2 = N_1 \left(\frac{S_1}{S_2} \right)^k \quad (4.6)$$

The estimated stress-life method has been compared to actual S-N curve data for Ti-6Al-4V at a cyclic stress ratio of $R = 0$. The resulting estimated S-N curve is shown in figure 4.5.

The data has been fitted based on a simplified version of the random fatigue limit (RFL) model, as proposed by Pascual and Meeker [92]. The RFL model describes the fatigue limit of each individual specimen, and maximum likelihood methods are used to estimate the parameters of the S-N as described by equation (4.7).

$$\ln N = \beta_0 + \beta_1 \ln(\sigma - \gamma) + \varepsilon \quad (4.7)$$

where β_0 and β_1 are fatigue curve coefficients, γ the fatigue limit of the specimen and ε the error term. The simplified model used for fitting uses another logarithmic which resulted in better data fitting, and is described by equation (4.8).

$$\ln(N - \varepsilon) = \beta_1 (\ln(\sigma) - \gamma) \quad (4.8)$$

As can be seen in the figure, the estimated S-N curve is well in agreement with the actual test data. The standard deviation of fitted curve of the test data has been used to calculate the actual

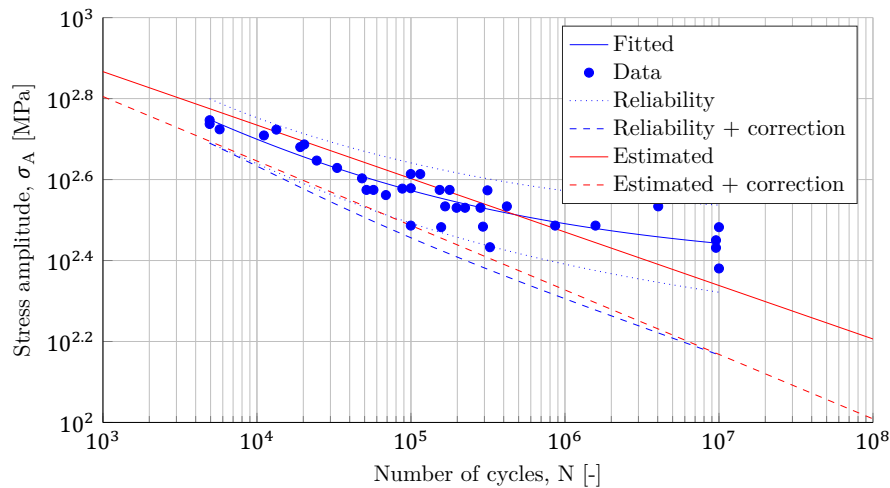


Figure 4.5: S-N data curve fitting vs. fatigue life estimation

reliability factor. Comparing the actual reliability to the estimated correction factor values also shows good agreement, and the same holds for application of the correction factors.

For the design case of the different engine components, the number of design life cycles should be determined. Since turbofan engines are typically designed for over 20 years of operation, the number of design load cycles extends beyond the low-cycle fatigue (LCF) limit into the high-cycle fatigue (HCF) range. According to Tong [11], a typical range for commercial production engines is between 15000–20000 flight cycles. The upper limit of this range is taken as the design conditions for all components. Table 4.5 shows an overview of the fatigue input conditions of each component.

Table 4.5: Component materials and fatigue design input parameters.

Stage	Component	Material	Loading type	Life cycles
Fan	Blades	Ti-6Al-4V	Axial	200,000
	Disks	Ti-17	–	200,000
	Pressure casing	Al-6061	Axial+Bending	200,000
	Blade containment casing	Kevlar	Impact	–
LPC	Blades	Ti-6Al-4V	Axial	200,000
	Disks	Ti-17	–	200,000
	Pressure casing	Ti-6Al-4V	Axial+Bending	200,000
Misc	Nose	Al-6061	–	–
	Shaft	Ti-17	Torsion	200,000

4.3. Blades

According to Armand [93] the blade volume can be approximated by taking the height of the blade, h_{bl} , multiplied by the squared value of the blade chord length, c_{bl} , and applying a volumetric correction factor, V_F , leads to equation (4.9).

$$V_{bl} = h_{bl} \cdot c_{bl}^2 \cdot V_F \quad (4.9)$$

The volumetric correction factors are defined by Onat & Klees [49] as fixed values for different type of compressor stages. The correction factors are defined as:

$$V_F = \begin{cases} 0.024 & \text{for fan blades} \\ 0.047 & \text{for LPC blades} \\ 0.163 & \text{for HPC blades} \end{cases}$$

The resulting blade mass includes the root section of the blade. However, more accurate results for blade weight estimation might be obtained by calculating the airfoil and blade root weight separately. In this

approach, the airfoil mass is estimated by creating a lofted surface from the stacked airfoils at different radial locations, and calculating the enclosed volume multiplied by a volumetric correction factor. This approach is used here, as it is assumed to be more accurate in predicting blade mass changes due to design parameter changes. The volumetric correction factor for fan blades is assumed to be $V_F = 0.055$, based on the wide-chord hollow fan blade weight from the CFM56-7B validation engine. For the fan stator, compressor IGV, rotor and stator airfoils all are assumed to be solid, and hence $V_F = 1$.

At the hub of the airfoil section, a compressor rotor blade is connected to the disk. The interface between the blade airfoil and the rotor disk called the blade root. In the documentation of GasTurb, the blade of a turbine engine is split up in several parts [10]. Figure 4.6 shows the build up of a typical blade root section.

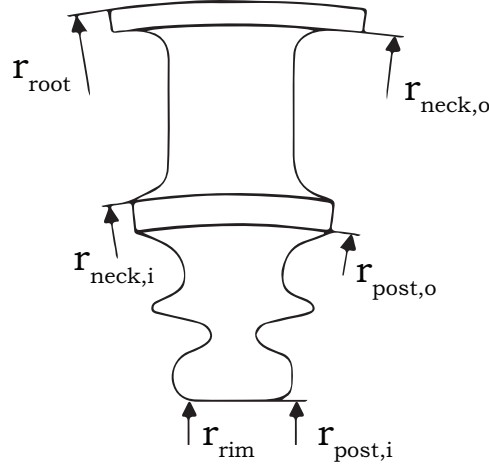


Figure 4.6: Blade build up. Source: [10]

A blade assembly can be divided into two main sections, the blade section and the root section. The blade section contains the airfoil and shrouds, while the root section exists of a platform, neck and fir tree. However, the neck only exists if the total height of the blade root is bigger than the sum of the blade platform thickness plus the fir tree height. The total mass of a blade assembly is given by equation (4.10):

$$m_{bl} = m_{af} + m_{srd} + m_{platform} + m_{firtree} + m_{post} + m_{neck} \quad (4.10)$$

The equations for the calculation of the airfoil, shroud, platform, fir tree, post and neck masses are given in equations (4.11)-(4.17) below. The blade root analysis is extended to correct for radial variation at the blade hub, hence when $r_2 \neq r_1$. The neck on the longer side of the blade, effectively adding a triangular shaped piece of material to the neck, which has the same thickness as the neck. The platform is rotated to match the blade hub.

$$m_{af} = \rho_{bl} \cdot V_{bl} \quad (4.11)$$

$$m_{srd} = \rho_{bl} \cdot 0.05 t_{rim}^2 \frac{2\pi r_{b,tip}}{n_b} \quad (4.12)$$

$$m_{platform} = \rho_{bl} \cdot 0.05 t_{rim}^2 \frac{2\pi r_{root}}{n_b} \quad (4.13)$$

$$m_{firtree} = \rho_{bl} \cdot t_{rim} \pi \frac{r_{neck,i}^2 - r_{rim}^2}{2 \cdot n_b} \quad (4.14)$$

$$m_{post} = \rho_{disk} \cdot t_{rim} \pi \frac{r_{post,i}^2 - r_{rim}^2}{2 \cdot n_b} \quad (4.15)$$

$$m_{neck} = \rho_{bl} \cdot 2 \cdot t_b \cdot t_{rim} (r_{neck,o} - r_{neck,i}) \quad (4.16)$$

$$m_{neck,ext} = \rho_{bl} \cdot t_b \cdot t_{rim} (|r_{root,1} - r_{root,2}| - r_{neck,o}) \quad (4.17)$$

where ρ_{bl} is the blade material density and ρ_{disk} is the disk material density. The total center of gravity

of the blade is then given by equation (4.18).

$$r_{cg,b} = \sum \frac{m_i r_{cg,i}}{m_{bl}} \quad (4.18)$$

4.4. Disks

The stress analysis of a rotating disk is described in many literature, and is usually solved considering infinitesimal ring-shaped disk part of constant thickness, as indicated in figure 4.7.

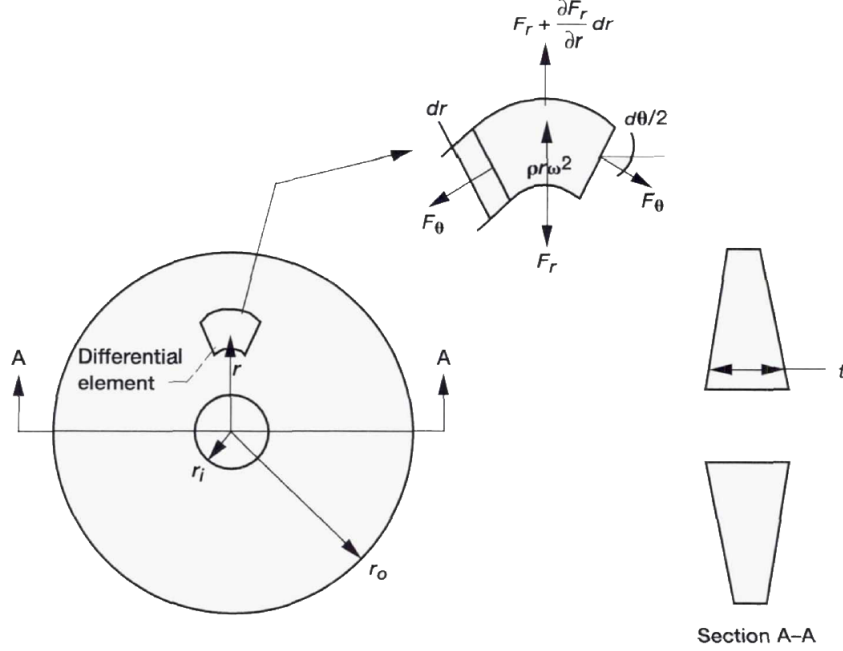


Figure 4.7: Rotating disk stress analysis. Source: [11]

Boorsma [19] presents three methods to solve the disk stress calculations in his work. One method from Mattingly [31], which allows for hyperbolic disk design at constant stress levels throughout the disk, secondly a finite difference method by Tong et al. [11], and finally a low fidelity method to optimize the disk shape, which is also used in T-AXI Disk [94, 95]. A fourth method for disk stress calculations has been added to this literature study. It is a calculation method presented in the work from Lolis [45], which mainly follows the method provided by a textbook from Potter [96].

In Boorsma's work it is concluded that the method used in T-AXI Disk will be best suited for preliminary disk stress calculations. This conclusion remains unchanged as the iterative solving structure for each element provided in Lolis' method, will result in slower calculations compared to the matrix calculations from the T-AXI Disk method. The governing equations for the disk stress analysis as described by Gutzwiller and used in T-AXI Disk, are shown below. [95]

Using a simple force equilibrium of the element indicated in figure 4.7, it is shown that the tangential and radial forces are given by equations (4.19) and (4.20).

$$\sum F_\theta = 0 \quad (4.19)$$

$$\sum F_r = \sigma_r \cdot r \cdot d\theta + \sigma_\theta \cdot dr \cdot d\theta - \left(\sigma_r + \frac{d\sigma_r}{dr} \cdot dr \right) \cdot (r + dr) \cdot d\theta - \rho \cdot \Omega^2 \cdot r^2 \cdot dr \cdot d\theta = 0 \quad (4.20)$$

After some algebraic manipulation, equation (4.20) can be rewritten in the form of equation (4.21).

$$0 = \frac{d}{dr}(tr \cdot \sigma_r) - t \cdot \sigma_\theta + t\rho\Omega^2 r^2 \quad (4.21)$$

The formula for the hoop stress, σ_θ , and radial stress, σ_r , are given in by equations (4.22) and (4.23) respectively.

$$\sigma_r = A \frac{du}{dr} + B \frac{u}{r} - A\alpha_r T - B\alpha_\theta T \quad (4.22)$$

$$\sigma_\theta = B \frac{du}{dr} + D \frac{u}{r} - B\alpha_r T - D\alpha_\theta T \quad (4.23)$$

The boundary conditions at the bore and at the rim of the disk are given by equations (4.24) and (4.25).

$$\sigma_r = A \frac{du}{dr} + B \frac{u}{r} - A\alpha_r T - B\alpha_\theta T = -\frac{n_b m_b r_{cg,b}}{2\pi r t} \Omega^2 \quad (4.24)$$

$$\sigma_r = A \frac{du}{dr} + B \frac{u}{r} - A\alpha_r T - B\alpha_\theta T = \frac{n_b m_b r_{cg,b}}{2\pi r t} \Omega^2 \quad (4.25)$$

Where $r_{cg,b}$ is given by equation (4.18), and constants A , B and D in the above equations are all functions of material properties such as material strength, E , and Poisson's ratio, ν , and their respective relations are shown in equations (4.4) – (4.4). Further details about the calculation process can be found in [94].

$$A = \frac{C_{11}C_{33} - C_{13}^2}{C_{33}} \quad (4.26)$$

$$B = \frac{C_{12}C_{33} - C_{13}C_{23}}{C_{33}} \quad (4.27)$$

$$D = \frac{C_{22}C_{33} - C_{23}^2}{C_{33}} \quad (4.28)$$

$$C_{11} = C_{33} = \frac{E_r(E_\theta - E_r\nu_{\theta r}^2)}{E_\theta - 2E_r\nu_{\theta r}^2} \quad (4.29)$$

$$C_{22} = \frac{E_\theta^2}{E_\theta - 2E_r\nu_{\theta r}^2} \quad (4.30)$$

$$C_{12} = C_{23} = \frac{E_r E_\theta \nu_{\theta r}}{E_\theta - 2E_r\nu_{\theta r}^2} \quad (4.31)$$

$$C_{13} = \frac{E_r^2 \nu_{\theta r}^2}{E_\theta - 2E_r\nu_{\theta r}^2} \quad (4.32)$$

The disk design is checked for feasibility based on three parameters. First the burst margin, BM , is calculated. According to Tong [11], the average tangential stress, $\sigma_{\theta,avg}$, should be at least 47% lower than ultimate strength of the material at the average disk temperature. The burst margin is calculated using equation (4.33).

$$BM = \left(\frac{0.47 \cdot \sigma_{ult}}{\sigma_{\theta,avg}} - 1 \right) \cdot 100 \quad (4.33)$$

The second design parameter is the design margin, DM , which compares the maximum allowable Von Mises stress, σ_{VM} , to the yield stress of the material, σ_y . A safety factor on the yield stress may be used, which results in equation (4.34).

$$DM = \left(\frac{0.9 \cdot \sigma_y}{\sigma_{VM}} - 1 \right) \cdot 100 \quad (4.34)$$

The burst speed, BS , of the disk is the last design parameter. The burst speed parameter takes into account the possible overspeed operation, at which the disk turn at more than the 100% rotational speed limit they are designed for. During the design mission, overspeed operations may occur for short periods of time, hence it is important to make sure the disk is designed to cope with the excessive stress loads that occur during such operational speeds. According to GasTurb, the disk should be designed for burst speeds up to 130%. [10]

$$BS = 100 \cdot \sqrt{\frac{\sigma_{ult}}{\sigma_{\theta,avg}}} \quad (4.35)$$

To take the effects of material fatigueness caused by cyclic loading of the disk into account, a fatigue life estimation method by Armand [93] is used. In this method, the equivalent strain range is calculated using the maximum-distortion-energy theory, shown in equation (4.36).

$$\Delta\varepsilon = \frac{\sqrt{2}}{3} \sqrt{(\varepsilon_r - \varepsilon_\theta)^2 + (\varepsilon_\theta - \varepsilon_z)^2 + (\varepsilon_r - \varepsilon_z)^2} \quad (4.36)$$

The value for the strain range obtained by equation (4.36) is compared to another definition of strain range, for a specimen loaded in only the axial direction. Equation (4.4) shows the relationship found by Mendelson & Manson [97] that relates the low-cycle fatigue life and other material properties to the strain range.

$$\Delta\varepsilon = 3.5 \frac{S_u}{E} N_f^{-0.12} + D^{0.6} N_f^{-0.6} \quad (4.37)$$

where, S_u is the ultimate tensile strength, E the Young's modulus, and D the ductility of the material. Since the temperature in the fan and LPC stage are relatively low, the material ductility is assumed to be constant. The ductility is a function of the reduction in area at failure, RA , and is calculated using equation (4.38).

$$D = \ln\left(\frac{1}{1 - RA}\right) \quad (4.38)$$

4.5. Casing

The casing of the fan and LPC stages have a great effect on the total engine weight. Therefore, it is important to carefully design such a component, while satisfying the main design requirements. Although the component casing has multiple functionalities in the total engine, the two main design criteria of the casing are the pressure containment and blade fraction containment. Several design philosophies exist for fan and compressor casings [45, 47, 98], and in this thesis two design methods are adopted.

In the fan stage two separate casings are designed. A steel casing is used to provide pressure containment in the fan stage and bypass duct. Section 4.5.1 further elaborates on the required casing thickness determination for pressure containment. Another, more critical design condition for the fan stage casing is the blade fraction containment. In case of a blade release, the fan casing should be able to withstand the blade impact. Blade fraction containment is ensured by introducing a kevlar liner inside the steel pressure pressure containment casing. The design methodology of the blade fraction containment casing is elaborated upon in section 4.5.2.

The casing in the LPC stages are only designed for pressure containment. However, as mentioned earlier the design point for the LPC casing is taken from the last HPC stage, as the casing is made of one piece and in practice the casing thickness often does not vary between these two components.

Apart from the static loading conditions, the casing fatigue life is also taken into account. The output of the static design case is used for the fatigue design which has been treated in section 4.2.

4.5.1. Pressure containment

When considering a static loads on the component, the casing thickness can directly be determined from Barlow's equation. Using this method, the casing is modelled as a pressurize pipe, and relates the internal pressure in the pipe or pressure vessel to the maximum stress level occurring in the material. Equation (4.39) shows the original formulation of Barlow's equation.

$$p_{st} = \frac{2 \cdot \sigma_y \cdot t}{D} \quad (4.39)$$

Where D is the casing outer diameter. However, for this design problem it is more convenient to rewrite the equation to solve for the minimum required thickness, given a material under a certain pressure, which leads to equation (4.40).

$$t_{cas,PR} = \frac{p_{st} \cdot r}{\sigma_y - p_{st}} \quad (4.40)$$

Where r is the casing inner radius and p_{st} the static internal pressure, given by $p_{st} = p_{in} - p_{out}$.

The above described design method results in very thin pressure casing thickness for the fan stage since the pressure difference between the inner fan casing and the ambient conditions are relatively

small. Onat & Klees [49] suggest a method by Stewart [99] which describes the collapsing pressure for thin-walled large diameter tubes. The collapsing pressure is given by equation (4.41).

$$p_{col} = 6.895 \cdot 10^6 \left(1 - \sqrt{1 - 1600 \frac{t^2}{D^2}} \right) \quad (4.41)$$

Where t is the the casing thickness, D the casing diameter and p_{col} the collapsing pressure. Although the external pressure will not exceed the fan duct inner pressure, the design condition for collapsing pressure is way more sensitive than the pressure containment design. Assuming a maximum pressure difference between inner and outer duct of 0.8 at static sea level conditions corresponds to a minimum casing thickness of $3.0mm$, which is used as a fixed minimum thickness in the design routine.

4.5.2. Blade containment

The blade containment casing is by far the most critical design condition for the fan stage. Since the pressure in the fan is relatively low, the minimum thickness requirements for the fan casing are low as well. The requirement for fan blade containment however is quite demanding, as the casing should be designed to withstand a full fan blade release at overspeed conditions.

Full scale analysis of blade impact and casing deformation extends beyond the scope of this thesis. For the conceptual design of the fan casing, a simple estimation method presented by Lolis [45] is used. First the fan blade kinetic energy at release is determined. Other methods sometimes include an extra term for the rotational kinetic energy. [100] The total kinetic energy is then given by equation (4.42)

$$E_{kin,bl} = \frac{1}{2} m_{bl} V_{bl}^2 + \frac{1}{2} I_{bl} \omega_{bl}^2 \quad (4.42)$$

where m_{bl} is the blade mass, V_{bl} the blade impact velocity, I_{bl} the blade mass moment of inertia and ω_{bl} the blade rotational velocity. For design using an energy balance, the kinetic energy of the blade should be balanced by the strain energy of the plastic deformed casing material. However, the method used here takes a more simple approach. The blade internal rotation is assumed zero, and hence the rotational kinetic energy is zero. The minimum required casing thickness is then defined by equation (4.43).

$$t_{cas,bl} = \frac{0.4 E_{kin,bl} E}{\sigma_y^2 h_{bl} c_{bl}} \quad (4.43)$$

4.6. Shaft

The low pressure shaft drives both the fan and compressor stages. The spool geometry is optimized for minimum weight. However, there are some constraints to the LP spool diameter. A larger outer diameter might be advantageous for the component torsional strength, the diameter should remain small enough as the HP spool is enclosing the LP spool.

The load on the LP spool is calculated based on the total compressor and fan specific work, \dot{W} . Equation (4.44) shows the relationship between the shaft stress as a result of the torsional loading, given an inner and outer diameter [47].

$$\sigma = \frac{16 D_o \dot{W}}{\omega \pi (D_o^4 - D_i^4)} \quad (4.44)$$

After the static design of the shaft is determined, the fatigue life is estimated using the method described in section 4.2. The optimum diameter and thickness of the shaft for minimum weight design are found using a simple optimization routine.

4.7. Spinner cone

The spinner cone is a hollow cone structure in front of the fan stage, which consists of a front and a rear cone part. The spinner front cone is usually designed to minimize the ice build-up and should be able to withstand bird-strike. The spinner rear cone is designed to smoothen the airflow at the fan inlet, usually resulting in a spline surface interface between the spinner front cone and the fan blade

platform. A simplified approach is used here, assuming a linear connection between the spinner front cone and fan blade platform, effectively extending the blade platform. The thickness of the nose cone is assumed to be fixed at $5mm$, as suggested by Lolis [45]. This value is well in accordance with the $4.9mm$ spinner front cone thickness measured on the CFM56-7 validation engine. The spinner front cone is made of black sulfuric anodized aluminium, but for the weight estimation here a standard aluminium alloy Al-6061 is used.

5

Noise Estimation

As shown in figure 2.4, noise propagation from high bypass ratio turbofan engines is dominated by the fan noise. At take-off however, jet stream noise can reach comparable levels to the fan noise. In this research, only the fan noise is considered and the noise propagation is predicted using three different noise estimation methods.

The noise prediction software *Soprano* uses two noise prediction methods developed by NASA: the Aircraft Noise Prediction Program (ANOPP) by Heidmann [54] and the improved ANOPP method by Kontos [55]. Diéz [5] introduced the use of a third method developed the Engineering Society of Data Units (ESDU) [101], and did a comparison with the three noise estimation techniques. Diéz concluded that there no large differences between the noise estimation methods were appreciated. The methods are well documented by Diéz [5], and hence his approach is adopted here to predict the noise output from the fan stage.

Another feature of the noise prediction tool is the fly-over simulation. The noise spectrum of the engine on itself is not a good indicator of the engine performance in terms of noise, as the perceived noise levels on the ground differ from the measurements directly at the source. For this reason, main noise descriptors are used to characterize the noise generated by the engine during a fly-over, which will be simulated using the noise spectrum output from the prediction methods. The determination of noise descriptors is further elaborated upon in section 5.6. The take-off and fly-over procedure is then described by section 5.5.

5.1. Noise prediction methods

Three empirical methods to estimate the noise propagation from the fan stage are considered here. Section 5.2 will elaborate on the ANOPP method by Heidmann. The other two considered methods originated from the original ANOPP method. Since the basic concepts of the empirical methods are therefore very much alike, only the differences between the methods will be explained for the other two methods in section 5.3 and 5.4 for the improved ANOPP method and ESDU method respectively.

5.2. Heidmann's method

The ANOPP method was originally presented by Heidmann in 1975 [54]. The method is used to compute the one-third octave band spectral intensities of the free field noise pattern. The intensities vary as a function of the polar angle about the fan or compressor axis, are assumed to be symmetric about this axis, and are given as the sound pressure levels (SPL) at a $1m$ radius.

The predicted free-field radiation can be divided into the following noise components:

1. Inlet duct noise
 - (a) Broadband noise
 - (b) Discrete-tone noise
 - (c) Combination-tone noise
2. Discharge duct noise

- (a) Broadband noise
- (b) Discrete-tone noise

Heidmann [102] tested full-scale fans at NASA Lewis Center to find parameters that correlate to the noise output of the fan. In the study, the fan is assumed to be a noise generator in which input mechanical power is converted to output sound power. Heidmann concluded that the sound power output is strongly related to the specific work performed during the compression process. Since the specific work and mechanical power are proportional to the total temperature rise in the stage ΔT and the mass flow rate \dot{m} a general form of the normalized sound pressure level SPL can be expressed in terms of equation (5.1).

$$SPL(f, \theta) = 20 \log \left(\frac{\Delta T_t}{\Delta T_0} \right) + 10 \log \left(\frac{\dot{m}}{\dot{m}_0} \right) + f(\text{design detail}) \quad (5.1)$$

in which ΔT_0 and \dot{m}_0 are reference values which are fixed at $\Delta T_0 = 0.555K$ and $\dot{m}_0 = 0.453kg/s$ respectively. The frequency spectral function $f(\text{design detail})$ depends on three main noise contributors as explained earlier. The contributions of broadband noise, discrete tone noise and combination tone noise are explained in sections 5.2.1, 5.2.2 and 5.2.3 respectively. A full detailed description of the ANOPP method can be found in Heidmann [54].

5.2.1. Broadband noise

The broadband noise is calculated by predicting the average behaviour of the one-third octave broadband noise

$$SPL(f, \theta) = 20 \log \left(\frac{\Delta T_t}{\Delta T_0} \right) + 10 \log \left(\frac{\dot{m}}{\dot{m}_0} \right) + F_1(M_{tip}, M_{tip,des}) \quad (5.2)$$

$$+ F_2(RSS) + F_3(\theta) + F_4(f, f_b) \quad (5.3)$$

where F_1 is a discrete function based on the operating and design relative tip Mach number, F_3 a directivity correction function for the broadband noise, and F_2 a correction function for the rotor-stator spacing parameter, RSS . The rotor-stator spacing parameter F_2 is determined by equation (5.4) or (5.5), depending on the inlet distortion conditions.

$$L = C_1 \log \left(\frac{RSS}{300} \right) \quad \text{without inlet flow distortions} \quad (5.4)$$

$$L = \begin{cases} C_1 \log \left(\frac{RSS}{300} \right) & \text{for } RSS \leq 100 \\ C_1 \log \left(\frac{100}{300} \right) & \text{for } RSS > 100 \end{cases} \quad \text{with inlet flow distortions} \quad (5.5)$$

where the relative rotor-to-stator spacing RSS is expressed in percentage of the tip rotor chord, and $C_1 = -5$ for broadband noise.

Finally, F_4 is determined using equation (5.6) and represents the broadband noise spectrum shape.

$$F_4(f, f_b) = 10 \log \left[e^{-0.5 \left(\frac{\ln \left(\frac{f}{2.5 f_b} \right)}{\ln \sigma} \right)^2} \right] \quad (5.6)$$

Here σ is the geometric mean deviation which is equal to 2.2, and f_b is the blade passage frequency, which is a function of the rotational speed, N , and the number of rotor blades, B . The definition of the blade passage frequency is given in equation (5.7)

$$f_b = \frac{N}{60} B \quad (5.7)$$

5.2.2. Discrete tone noise

The discrete tone noise is described by equation (5.8).

$$SPL(f, \theta) = 20 \log \left(\frac{\Delta T_t}{\Delta T_0} \right) + 10 \log \left(\frac{\dot{m}}{\dot{m}_0} \right) + F_1(M_{tip}, M_{tip, des}) + F_2(RSS) + F_3(\theta) + 10 \log [10^{0.1F_4(f, f_b)} + 10^{0.1F_5(f, f_b)}] \quad (5.8)$$

where again, F_1 is a discrete function describing the peak sound pressure level, based on the operating and design relative tip Mach number, F_3 a directivity correction function for discrete tones. The correction function for the rotor-stator spacing, F_2 is determined by equation (5.4), with the constant $C_1 = -10$.

A simplified form of the cut-off factor δ for the fundamental tone is given by equation (5.9).

$$\delta = \left| \frac{M_{tip}}{1 - \frac{V}{B}} \right| \quad (5.9)$$

where V is the number of stator blades. If the cut-off factor reaches values of $\delta \leq 1.05$, the fundamental tone level is reduced by 8 dB. The correction is not applied if the cut-off factor exceeds 1.05. The tonal noise reduction and cut-off is shown in figure 5.1.

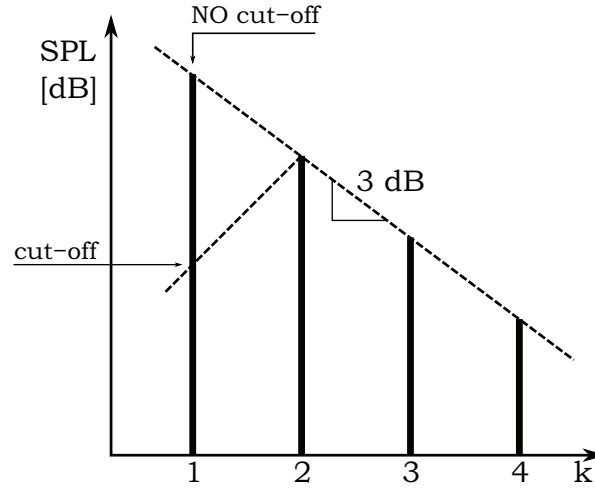


Figure 5.1: Rotor-stator interaction discrete tone harmonic levels and fundamental tone level cut-off. Source: [5]

5.2.3. Combination tone noise

Finally, the sound pressure level for the combination tone noise is described by equation (5.10). The combination tone noise is calculated at 1/2, 1/4 and 1/8 of the blade passage frequency, and ultimately added on an energy basis to obtain the total combination tone noise sound pressure level.

$$SPL(f, \theta) = 20 \log \left(\frac{\Delta T_t}{\Delta T_0} \right) + 10 \log \left(\frac{\dot{m}}{\dot{m}_0} \right) + F_1(M_{tip}) + F_2(\theta) + F_3(f, f_b) \quad (5.10)$$

where F_1 is a predictive function for the combination tone noise levels at 1/2, 1/4 and 1/8 of the blade passage frequency. F_2 is a directivity correction function for the combination tone noise, and F_3 a correction for the combination tone noise peak level spectrum content, depending on the blade passage frequency.

5.3. Improved Heidmann's method

In 1996, the improved ANOPP method was presented by Kontos et al. [55]. This method uses essentially the same fundamental equations as described in the original method by Heidmann, however some alternations were made to the correction factors. The difference between the two methods are listed below:

1. For the broadband noise propagating from the inlet (1a), the correcting function F_1 is modified and the term F_2 is eliminated.
2. For the broadband noise radiation from the discharge duct (2a), the correcting factor F_1 is modified.
3. For the discrete tone noise radiation (1b & 2b), the tonal reduction quantity is modified. Instead of a 3 dB reduction, the improved ANOPP method suggests a reduction of 6 dB or 9 dB, depending on the tip Mach number.
4. For the discrete tone noise propagating from the inlet (1b), the term F_2 is eliminated.
5. For the discrete tone noise radiation (1b & 2b), a further reduction of the blade pass frequency (BPF) tone and its second harmonic is proposed. The new reductions are dependent on the polar angle, and have to be interpolated from a table presented in the paper.
6. For the combination-tone noise (1c), the normalized combination tone noise levels, F_1 , are revised.

5.4. ESDU method

The ESDU method [101] is presented by the Engineering Sciences Data Unit (ESDU) in 1998, and is also based on the Heidmann's method. Therefore only the differences between the ANOPP and this method are mentioned here:

1. For the broadband noise propagating from the discharge duct (2a), a new directivity pattern is applied.
2. For the broadband noise radiation (1a & 2a), the spectrum content function, F_4 , is modified
3. For the discrete-tone noise radiation (1b & 2b), the directivity function is modified. For the superior harmonics, the tonal noise reduction is also changed.
4. For the combination-tone noise (1c), the normalized combination tone noise levels, F_1 , are revised.

5.5. Take-off simulation

A simulation of a take-off procedure will be used to determine the noise performance of the engine fan stage as measured by an observer on the ground. The simulation is set-up is according to the International Civil Aviation Organization (ICAO) regulations. Lateral and fly-over noise measurements are mandatory for the certification procedure described in ICAO regulations (Annex 16 to Chicago Convention, Volume I, chapter 3). Figure 5.2 and 5.3 show the take-off procedure flightpath with the location of the observer and important ground speeds and flight angles indicated.

For the take-off simulation a Boeing 767-300ER aircraft is used as the reference aircraft, equipped with two CF6-80C2/B6F engines [103]. All relevant input used for the determination of the take-off procedure flightpath is mentioned in table 5.1.

Table 5.1: Take-off simulation input parameters.

Property	Symbol	Value	Units
Rotation speed	V_R	82.24	m/s
Lift-off speed	V_2	84.81	m/s
Climb speed	V_C	92.52	m/s
Lift-off angle	γ_{L-o}	8	deg
Climb-out angle	γ_{C-o}	14	deg
Longitudinal distance	L_{long}	6500	m
Lateral distance	L_{lat}	450	m
Maximum take-off mass	$MTOM$	186880	kg
Maximum take-off thrust	F_{T-o}	269657	N

From the flight path the distance and angle as measured from the indicated observer points can be calculated, from which the variation of the distance and angle over simulation time can be found. Figures 5.4 and 5.5 show the distance and angle history respectively.

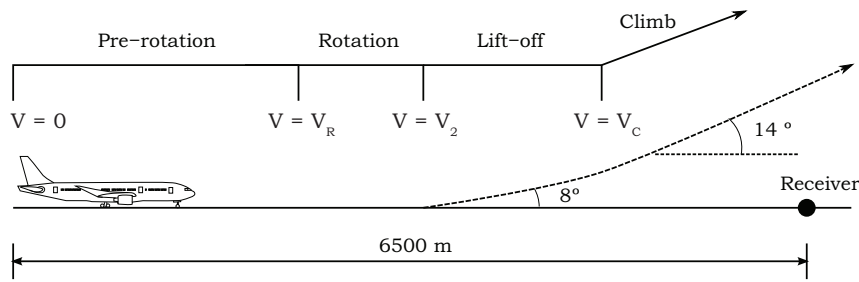


Figure 5.2: Take-off procedure. Source: [5]

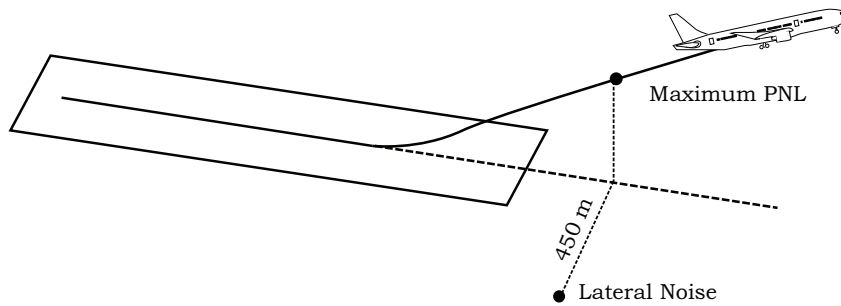


Figure 5.3: Lateral noise measurement location. Source: [5]

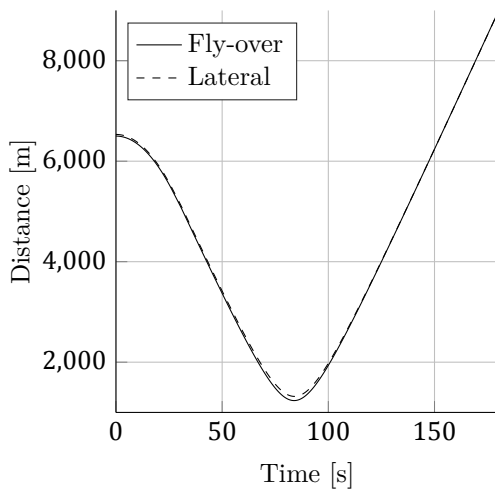


Figure 5.4: Distance history for 767-300ER take-off procedure.

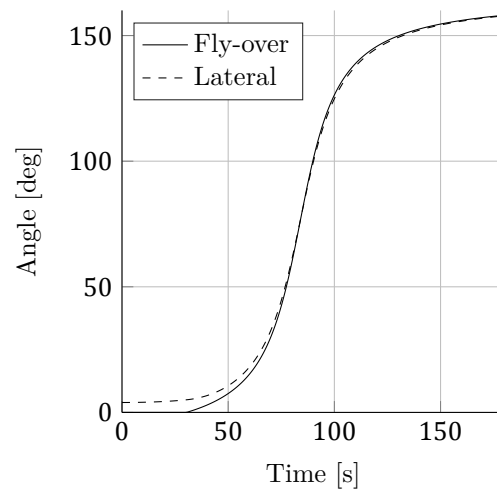


Figure 5.5: Angle history for 767-300ER take-off procedure.

5.6. Noise descriptors

Noise descriptors are used to give a better understanding of how a noisy event is perceived by humans on the ground. The ICAO has defined several noise descriptors for certification purposes. This section will elaborate on the calculation process of the noise descriptors.

The equivalent perceived noise level (EPNL) is the most important noise performance indicator, which is a modification to the perceived noise level (PNL) and takes the noise level as perceived by a human observer as well as the duration of the noisy event into account. To calculate the EPNL, the sound pressure level from the simulation should first be corrected for the Doppler shift, which is induced by the moving noise source. The frequency shift as a result of a moving noise source perceived by a

static observer is given in equation (5.11).

$$f_M = \frac{f}{1 - M \cos \theta} \quad (5.11)$$

where f_M is the frequency perceived by the observer, f the noise emission frequency, M the flight Mach number and θ the emission angle. The Doppler effect shifts the central frequency of each one-third-octave bands, and thus the SPL of the bands are affected. The corrected SPL is calculated using equation (5.12).

$$SPL_{i,new} = SPL_{i,old} \left(1 - \frac{S_i}{BW_i} \right) + SPL_{i\pm 1} S_{i\pm 1} \quad (5.12)$$

where S_i is the shift in central frequency and BW_i is the bandwidth of the i -th band.

The EPNL is calculated using equation (5.13).

$$EPNL = 10 \log \left(\frac{\Delta t}{T_{10}} \sum_{k=t_1}^{t_2} 10^{\frac{TPNL}{10}} \right) \quad (5.13)$$

where Δt is the time step, T_{10} a time-constant, and TPNL the tone corrected perceived noise level. The values t_1 and t_2 describe the beginning and end times in which the TPNL lies within 10 dB of the peak value. The tone corrected perceived noise level is given by equation (5.14).

$$TPNL = PNL + C \quad (5.14)$$

where C is the tone correction to the SPL spectrum. The perceived noise level (PNL) is determined from equation (5.15).

$$PNL = 40 + \frac{10}{\log 2} \log N \quad (5.15)$$

where N is the overall Noy value. The Noy value in its term is determined using equations (5.16).

$$N = n_{max} + 0.15 \left[\left(\sum_{i=17}^{40} n_i \right) - n_{max} \right] \quad (5.16)$$

where N is the total perceived noisiness, n_i is the perceived noisiness of the i -th band, and n_{max} is the maximum perceived noisiness of the 24 considered bands. n_i may be determined by converting tables for the earlier described Doppler corrected SPL [104].

6

Module validation

The validation of the three design modules is treated separately in the next sections. First the aerodynamic performance module is validated in section 6.1 using engine test run data from a CFM56-7B engine. Then the structural analysis and weight estimation module are validated using the same engine in section 6.2. Finally, the noise prediction module is validated in section 6.3 using fan noise data of a CF6-80C2 engine. After the modules have been validated, the effects of increasing tip diameter, varying spool speed and bypass ratio effects are tested using the design and sizing tool in chapter 7.

6.1. Aerodynamic module

The aerodynamic module uses an iterative solving procedure for the fan design. A one-dimensional flow analysis is carried out at multiple radial sections, and using empirical loss models the pressure loss at each blade-element is calculated. A vortex design method is applied to distribute the spanwise loading of the fan blade, and radial- and mass flow equilibrium checks ensure the design converges to a feasible solution. The fan design optimization process then maximizes the fan rotor efficiency for a given design fan pressure ratio. A redesign of the CFM56-7B fan stage at take-off conditions is considered here, and compared to the actual fan design. However, the input design fan pressure ratio has to be limited to $FPR = 1.35$, since higher values for the fan pressure ratio result in infeasible design solutions. Compared to the actual fan pressure ratio of approximately $FPR = 1.6$, this is quite low. The reason for the limited capabilities of the design code are the constraint acting on the positive camber angle ($\theta \geq 0$) and the DeHaller design limit ($DH \geq 0.72$). The camber angle constraint is applied for obvious reasons, as the iterative solving process for the blade angles and the loss models do not account for infeasible conditions. As discussed in section 3.2, the DeHaller number is a non-dimensional design parameter which limits the diffusion in a compressor stage to prevent excessive losses. These constraints limit the design space of the fan blade optimization process, and a maximum fan pressure ratio of $FPR = 1.35$ could be achieved. The aerodynamic performance of an optimized CFM56-7B turbofan engine fan rotor blade is shown in figure 6.1.

The spanwise distribution of the adiabatic rotor efficiency is shown in figure 6.1c. Due to the increasing relative velocity with radial location, the temperature difference over the rotor stage increases, boosting the fan efficiency. However, near the rotor tip the efficiencies suddenly decrease as a result of a steep increase of the loss parameters. The correlations of the shock and profile loss parameters are shown in figures A.1 and A.2 of appendix A respectively.

A relative high adiabatic efficiency is achieved over the rotor blade. However, it should be noted that these are the results for the rotor alone. The fan stator in the bypass duct and IGV at the LPC inlet decrease the efficiency as the total temperature remains constant, while pressure losses do occur over the static blade rows.

Figure 6.1d shows the DeHaller number and the axial velocity ratio distribution over the blade span. The DeHaller number is pushed towards its lower limit near the blade hub, while at the blade tip the positive camber angle constraint is limiting the design.

Figure 6.2 shows the optimized fan rotor blade shape. At three indicated radial locations, cross-sectional cuts along the streamline of the blade are made to show the local blade airfoil shape. Low

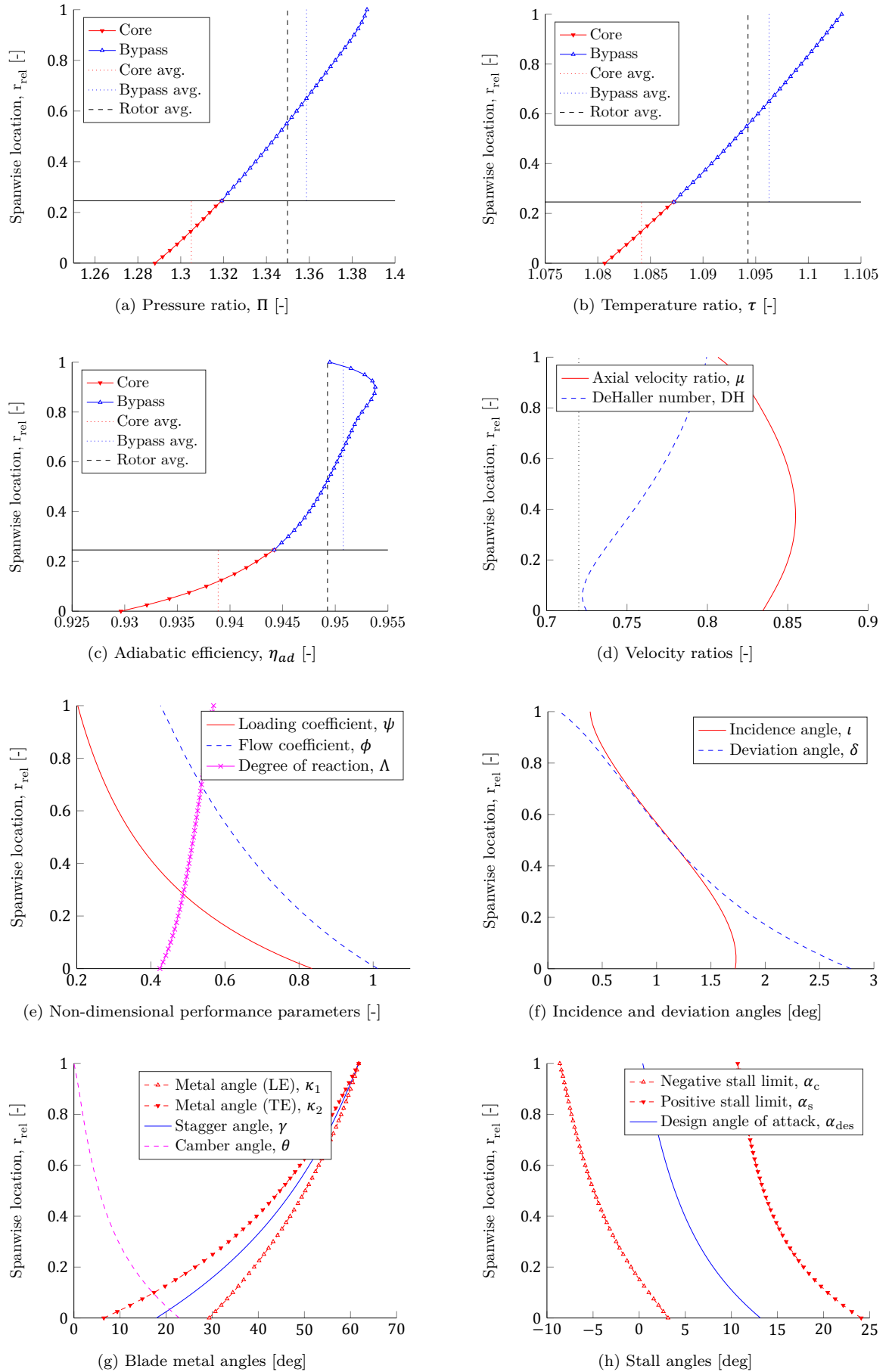


Figure 6.1: Optimized fan results for CFM56-7B engine at take-off design point.

camber angles are From figure 6.1g a trend of decreasing camber angle towards the blade tip can be

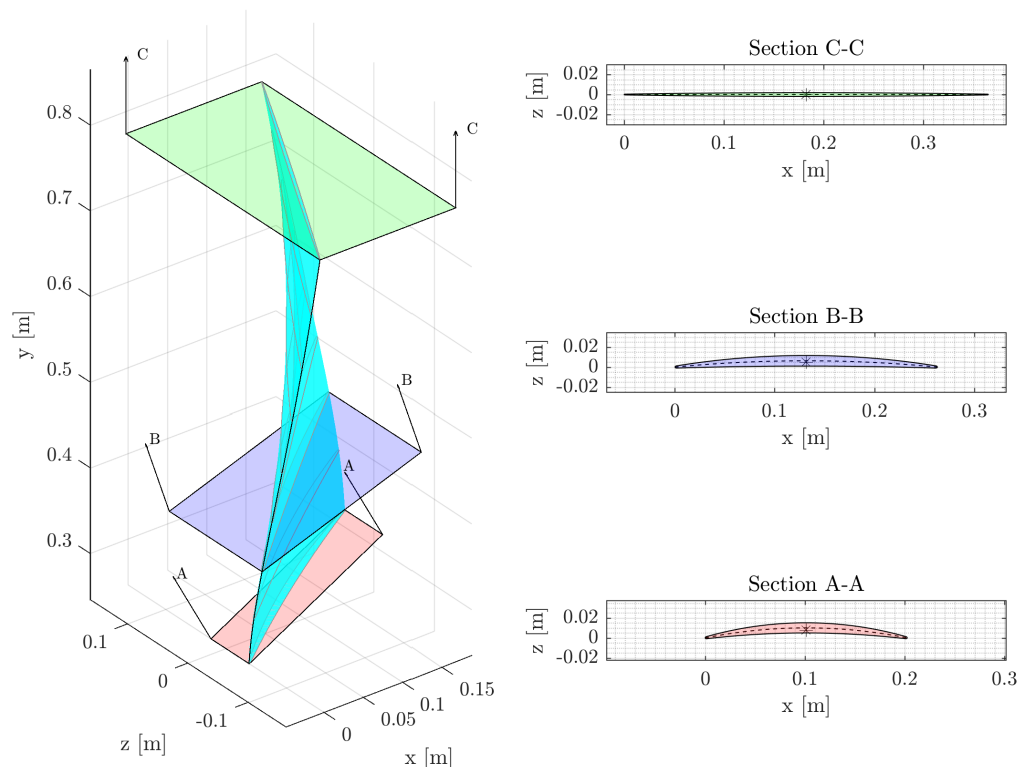


Figure 6.2: Optimized fan blade shape of a CFM56-7B engine at take-off design point, with section cuts along the streamline at hub, splitter and tip radii.

observed which limits the local blade loading. The blade is designed to operate at the optimum incidence angle over the entire blade span to ensure minimum loss over the cascade, as explained in section 3.3.6. An iterative solving method as described in figure 3.10 is used to determine the blade metal angles by converging the deviation and incidence angles calculations. Typically, minimum loss occurs at low incidence and deviation angles, thus effectively the blade is aligned to the airflow angles which results in the observed trend of increasing blade twist towards the tip.

In previous research by Díez [5] on the conceptual study of contra-rotating fans, higher fan pressure ratios were obtained using the same 1D fan analysis. Further inspection of the results obtained by Díez showed that the DeHaller design limit was not taken into account since DeHaller numbers below the design limit of 0.72 were encountered near the hub of the rotor. The effect of decreasing the DeHaller design limit is tested with the current design tool. The results obtained for the redesign of the CFM56-7B fan blade at take-off conditions with the decreased DeHaller design limit, are shown in figure 6.3. Indeed, higher fan pressure ratios can be achieved with the decreased DeHaller design limit. The fan blade is optimized for a fan pressure ratio of $FPR = 1.6$, which roughly represents the average fan pressure ratio of the CFM56-7B engine, and using a low vortex swirl exponent of $n = 0.1$. The aerodynamic performance of the optimized fan blade is shown in figure 6.3. Figure 6.4 shows the calculated airfoil and a validation sections of an actual CFM56-7B fan blade at approximately one-third of the blade height. It can be concluded that the decreased DeHaller number results in a more accurate representation of the actual fan blade geometry.

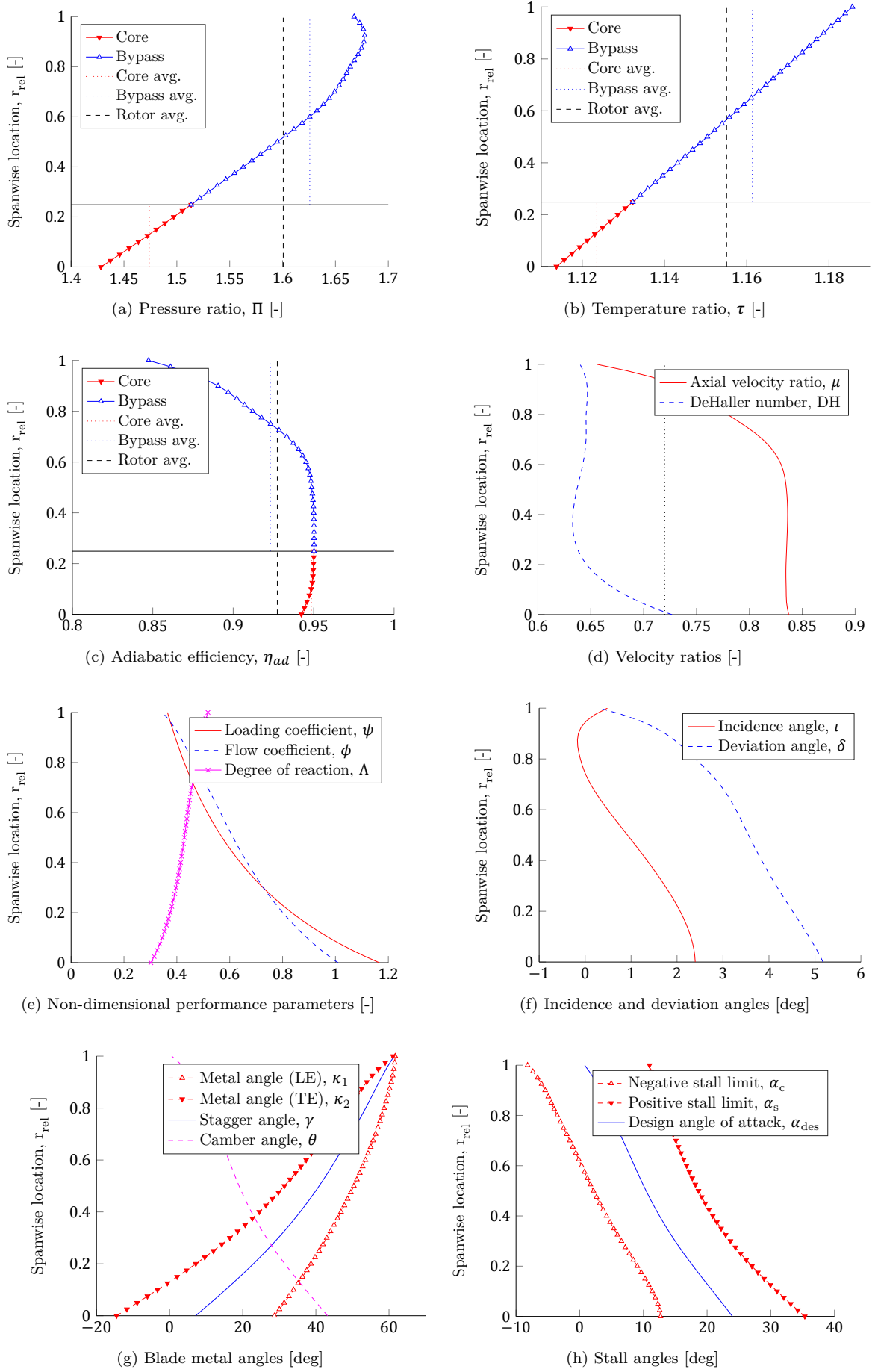


Figure 6.3: Optimized fan results for CFM56-7B engine at take-off design point, with alternative DeHaller design limit of 0.6.

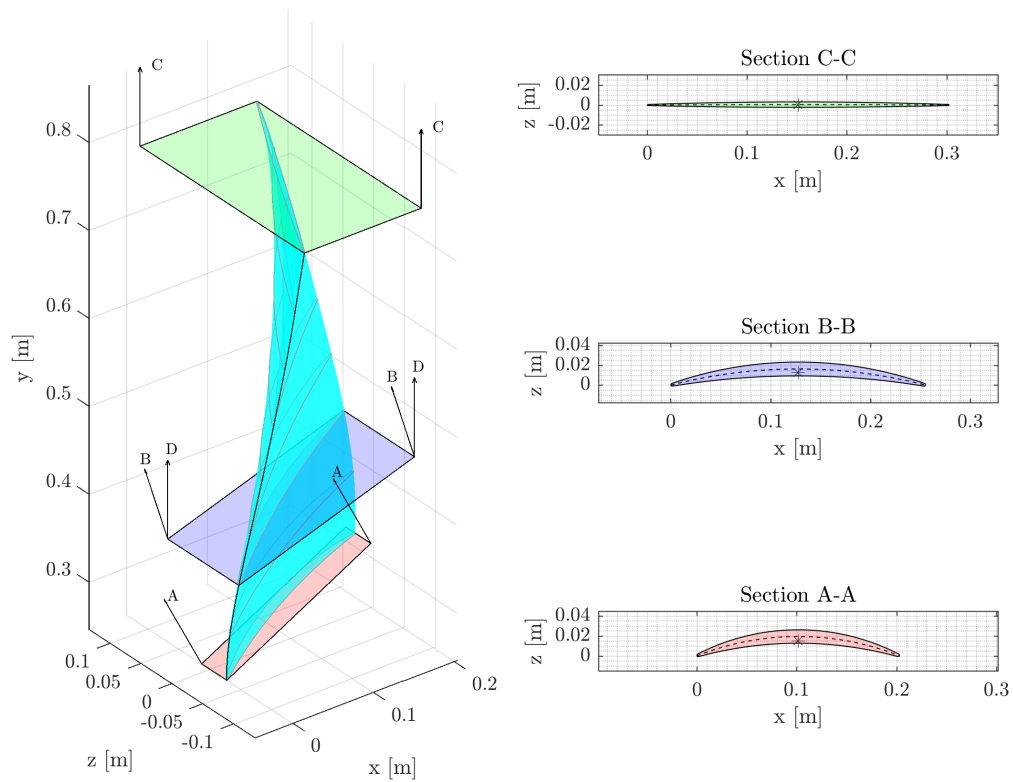


Figure 6.4: Optimized fan blade shape of a CFM56-7B engine at take-off design point, with alternative DeHaller design limit of $DH \geq 0.6$. Section cuts shown along the streamline at hub, splitter, and tip radii, and horizontal projected section cut at the splitter.

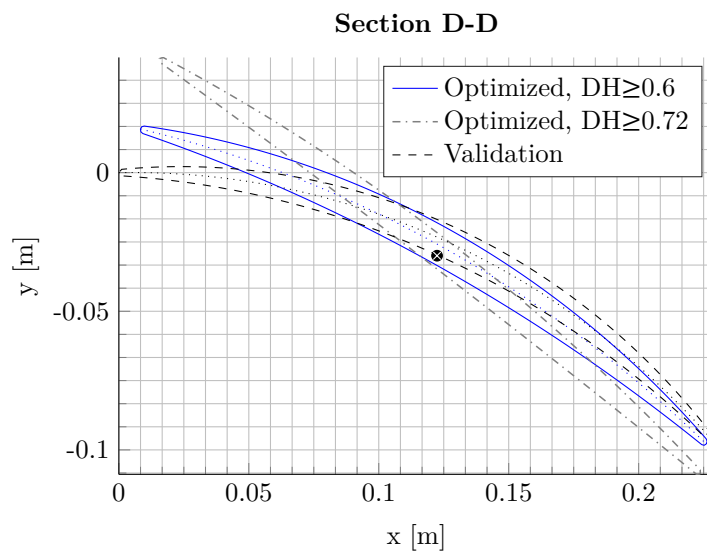


Figure 6.5: CFM56-7B fan blade validation section at approximately one-third of blade height.

From the results in figure 6.3a it can be seen that the decreased DeHaller limit allows for designs with higher fan pressure ratio. The design optimization routine in this work is designed to take the DeHaller criteria into account at each blade element, which results in a smaller design space and hence limits the domain of achievable design fan pressure ratios. The default limit is set to the design limit mentioned in literature, but can easily be changed to a custom design limit.

The fan rotor blade performance at off-design conditions is shown in figure 6.6. Although the figures show typical behaviour as seen on any fan map these values can not be validated due to the lack of available data for off-design performance of the validation CFM56-7B engine. However, since the off-design performance is not part of the analysis in the research question, the acknowledgement of a correct general trend is acceptable for the application here.

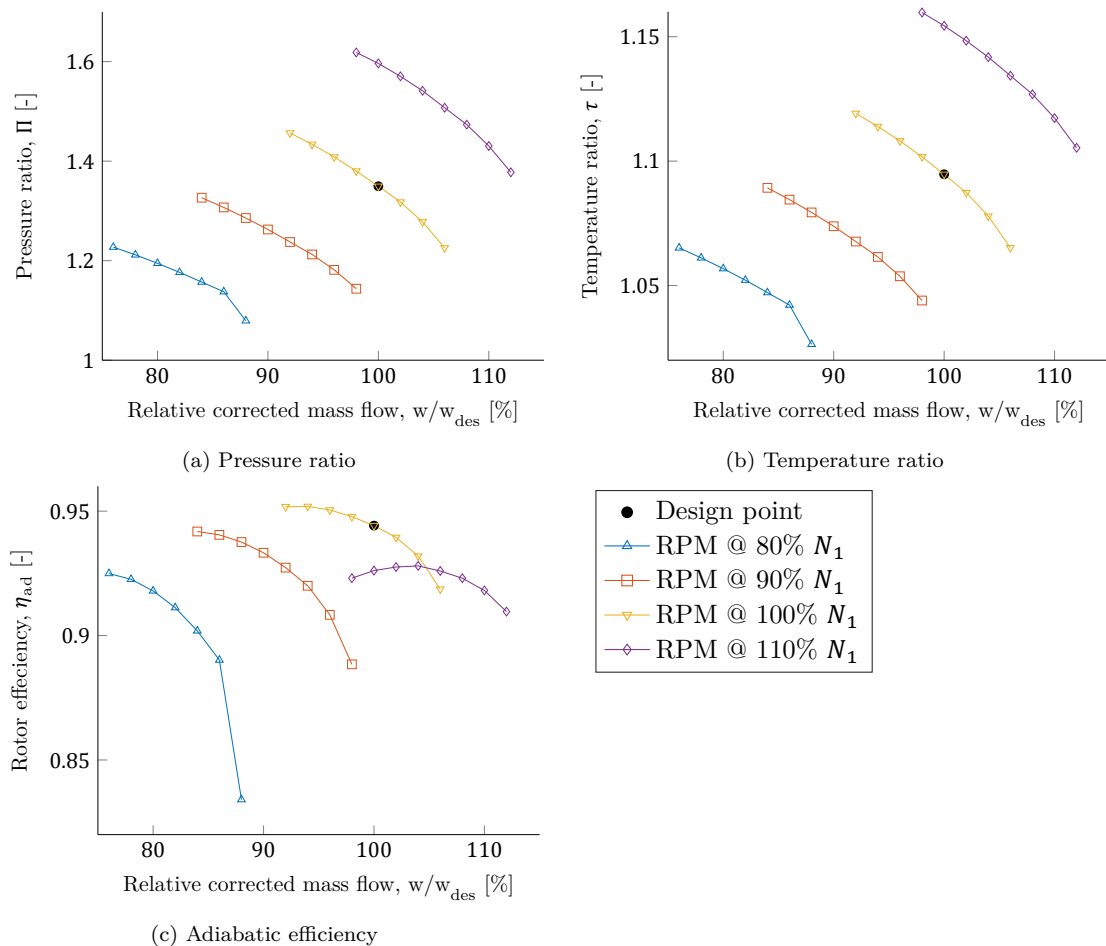


Figure 6.6: Fan rotor blade off-design performance with design point indicated.

6.2. Structural analysis & weight estimation module

Since only limited data is available on the exact weight of engine components, the weight estimation methods used here are validated by comparison to other available weight prediction methods. The blade assembly masses are calculated using a volume fraction based approach for the airfoil section and using the estimation method as described in section 4.3 for the blade root section. A small titanium blade with a blade height of 0.111 m is used as a validation case. The blade weighs about 150 g, without dead weight. This is compared to a calculated first stage low-pressure compressor rotor blade with a blade height of 0.104 m, with a mass of 0.1499 kg for the airfoil alone, and 0.292 kg for the blade including dead weight. The values are close enough to the real values, and using the extensive calculation method for the blade roots as described in section 4.3, it is expected that the weight trends are well-captured

by the weight estimation module.

The rotating disks are designed using a disk stress analysis method described by Manson, and is validated using `T-AXI Disk`. A pre-defined disk geometry has been used as input to the `Matlab` and `T-AXI Disk` disk stress analysis routine. Initially, large discrepancies were found in stress levels at the bore of the disk. The source code reveals that a linear temperature distribution is assumed, which uses the input for temperature at the bore as temperature at the engine rotational axis. This temperature distribution has been adopted in the design tool as an option. Figure 6.7 shows the three temperature distributions available for the disk stress analysis. The "linear0" temperature distribution corresponds

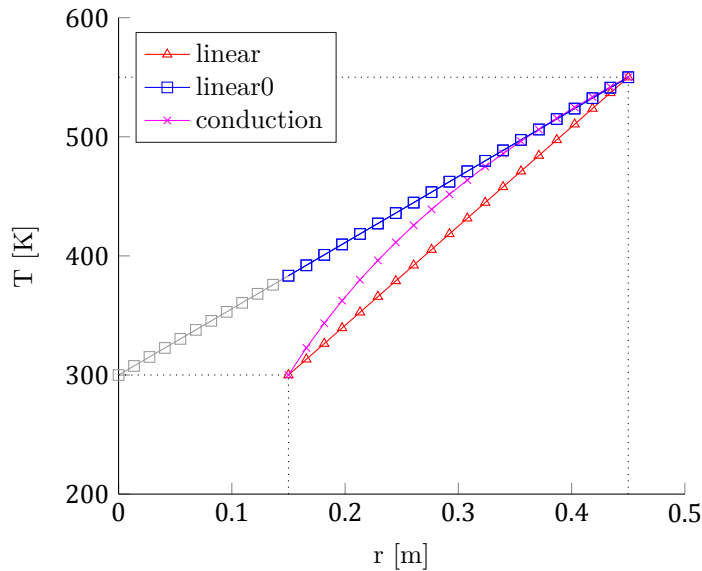


Figure 6.7: Disk stress analysis validation using `T-AXI Disk`

to the method used in `T-AXI Disk`. Using the same temperature distribution, nearly identical results were obtained for the disk stress validation in `Matlab`. Next, the disk optimization routine in `Matlab` is compared to the disk optimization from `T-AXI Disk`, to validate that the disk constraints mentioned in Tong [11] are implemented properly. The results of the analysis are shown in figure 6.8. Figure 6.8

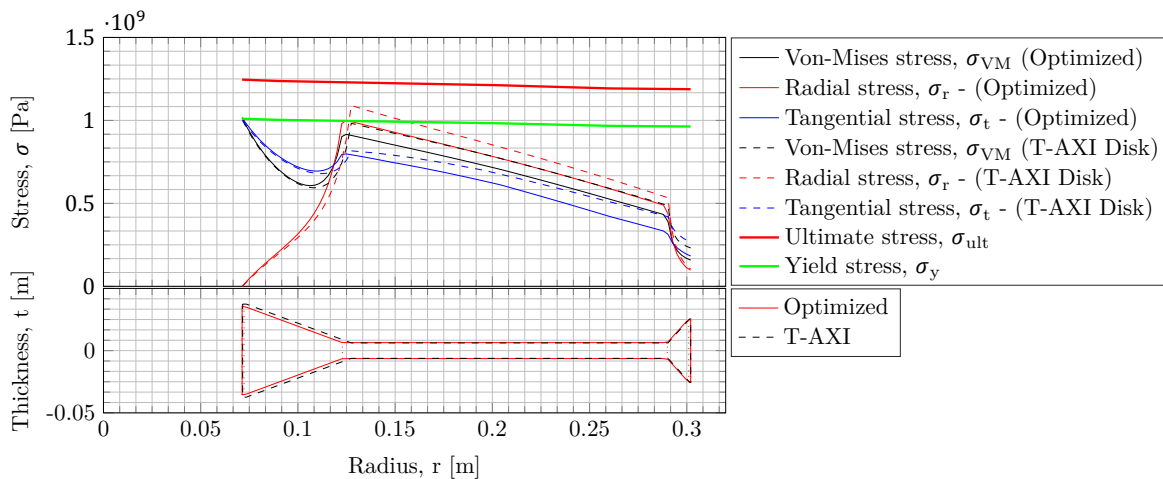


Figure 6.8: Disk stress analysis validation using `T-AXI Disk`

shows the results of an arbitrary disk optimization using Manson's method in `Matlab` versus the disk optimization tool in `T-AXI Disk`. As can be seen, `T-AXI Disk` does not take into account the yield stress criteria for the disk radial stress. Therefore, from the beginning of the neck until the disk rim a small offset is observed. Overall, the disk stress analysis and optimization method have proven to be

well in agreement with the results from T-AXI Disk.

Figure 6.9 shows an overlay of the fan and compressor stage designed with the engine conceptual design tool for the CFM56-7B at design tip radius.

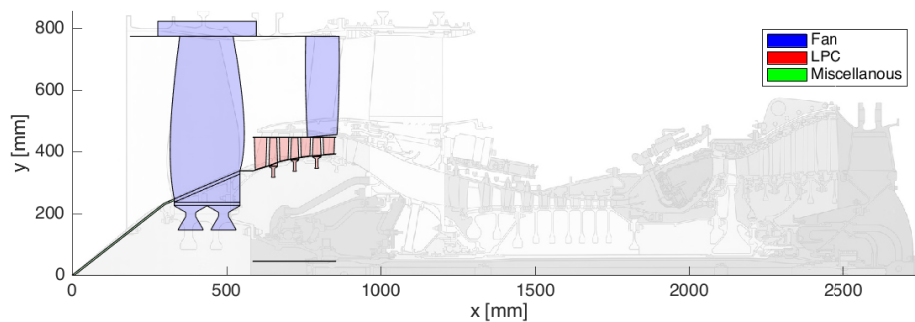


Figure 6.9: CFM56-7 Sectional drawing overlay. *Source:* [12]

As expected, the fan casing thickness resulting from the pressure containment criteria is smaller than the minimum design thickness. Therefore, the minimum casing thickness of 3mm is applied, as mentioned earlier in section 4.5. The blade containment casing material used in this design case was Al-6061, which resulted in a very thick blade containment casing design of 26.57 cm . If however Ti-6Al-4V would have been used, a casing thickness of 8.36 cm would be sufficient. Using pure carbon epoxy material results in the thinnest blade containment design of 1.52 cm thickness. Therefore, in the design cases later on, carbon epoxy is used as blade containment casing material.

The spinner cone is accurately sized as addressed in 4.7, and this is confirmed in figure 6.9. The design optimization procedure of the shaft designs the component for minimum weight. In this case, it keeps the thickness at the minimum value, and the pushes the inner radius outwards, until the maximum stress value found for the fatigue design is lower than the material yield strength.

A post-processing routine is developed to allow for visual inspection of the engine design. The tool generates 3D objects for all component, hence a 3D model of the designed engine section can directly be generated and exported to an universal 3D file type. It is advised to not view the 3D model inside the plot environment of Matlab, but rather use dedicated 3D mesh processing software such as MeshLab due to the poor performance of Matlab's plot environment with respect to rendering large 3D objects. Figure 6.10 shows the 3D model output rendered in MeshLab with a cut-out section.

6.3. Noise module

The noise module is validated using fan noise data from extensive tests conducted at the NASA Lewis Research Center in Cleveland, Ohio [55]. The CF6-80C2 engine is used as a validation case for the noise module, as discussed in section 2.5. The fan inlet and exhaust noise spectra are calculated at a range of directivity angles as measured from the engine inlet axis using three prediction methods as described in 5.1. It should be noted that the noise prediction method used here has already been validated by Díez. However, since different results were obtained in this research, the new results are presented here. Table 6.1 shows the input parameters used by Díez compared to input parameters used here.

As can be seen in table 6.1, most of the inputs correspond to the input parameters used by Díez. The Mach numbers mentioned by Díez however, do not correspond to the values mentioned in the validation source [55]. A relative tip design Mach number of 1.53 was mentioned in the noise validation data report for the CF6-80C2 engine. Therefore, this value is adopted here for validation purposes. The blade tip Mach number is calculated from the spool speed and fan tip radius. An axial Mach number of 0.5 is assumed at take-off on the fan face, and from that the relative tip Mach number of 1.175 is constructed. The results of the noise spectrum level calculations using the new input parameters are shown in figure 6.11.

In general, the computed noise spectrum data follows the same trend as the validation data, except for the lower range frequencies of the inlet radiated noise spectra. Large discrepancies between reported experimental data and computed noise spectrum levels are present in these lower bands of the noise spectrum. For the ANOPP method and the improved ANOPP method, this has also been reported

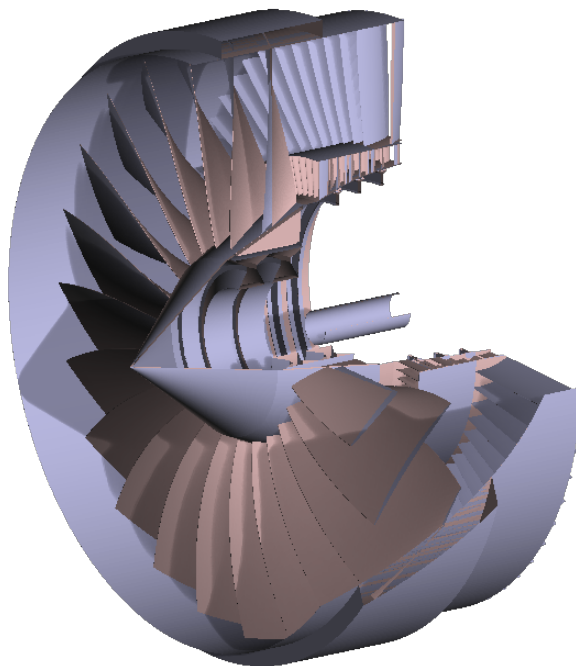


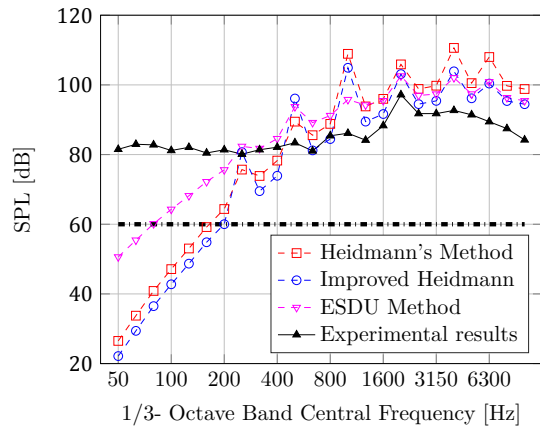
Figure 6.10: CFM56-7 LPC components exported to 3D output.

Table 6.1: Input for noise spectrum level calculations of the CF6-80C2 engine.

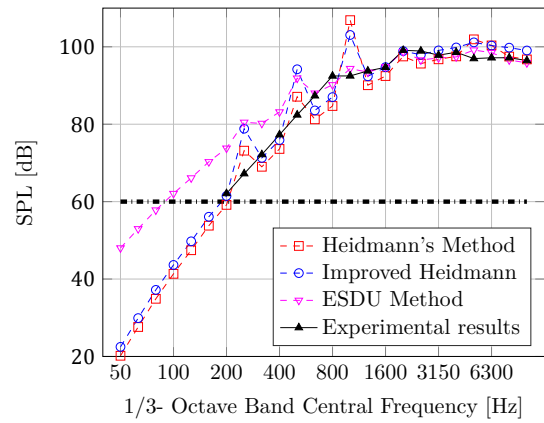
Parameter	Symbol	Input data		Units
		New	Diez	
Fan tip radius	r_{tip}	1.097	1.097	m
Temperature increase	ΔT	58.66	58.66	K
Mass flow rate	\dot{m}	802	802	kg/s
Spool speed, inlet	N_1	3150	3150	RPM
Spool speed, exhaust	N_1	3534	3534	RPM
Rotor-stator spacing	RSS	200	200	$\%$
Rotor blades	B	38	38	–
Stator blades	V	80	80	–
Design rel. tip Mach number	M_{trd}	1.53	1.15	–
Rel. tip Mach number	M_{tr}	1.175	1.06	–
Blade tip Mach number	M_t	1.064	0.77	–
Measurement radius	r	45.72	45.72	m
Measurement angle inlet	θ_{lat}	[20; 50; 80]	[20; 50; 80]	deg
Measurement angle exhaust	θ_{lon}	[90; 120; 150]	[90; 120; 150]	deg

by Kontos [55]. Since the ESDU method is based on the same fundamental equations for the noise prediction, a similar trend is seen here. However, the noise levels for these frequencies are relatively low as compared to the noise levels at frequencies from 1 kHz and above. Therefore, the error in the lower range frequencies will have small impact on the perceivable noise levels.

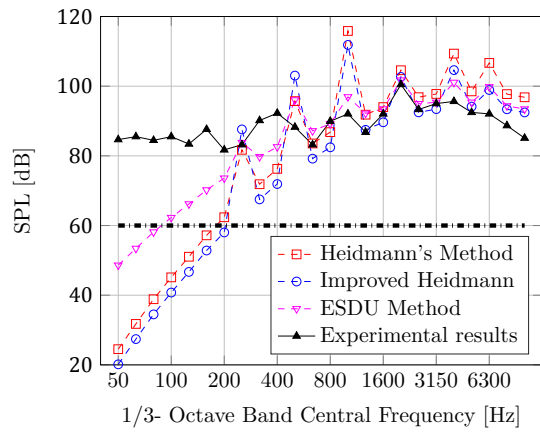
Another notable detail are the repeating large peaks predicted in sound pressure levels occurring between 200 Hz and 6300 Hz using Heidmann's and improved Heidmann's methods. These peaks are also present for the ESDU method, but much more subtle, and correspond well with the data. The peaks are related to the bypass frequency tone, which for the CF6-80C2 at take-off conditions is calculated to be $f_b = 1995Hz$. Comparing the results to the reported values by Díez [5] and Kontos [55], the effect of the bypass frequency is overestimated here. Since the ESDU method does not suffer from the same over-predictions, the error is suspected to be caused by the correction factors applied in Heidmann's and Heidmann's improved method.



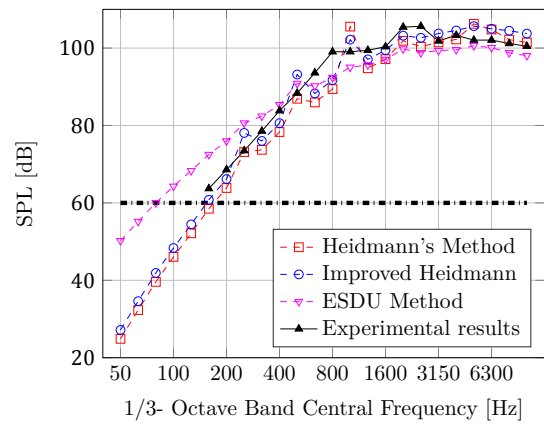
(a) Inlet, measured at 20°



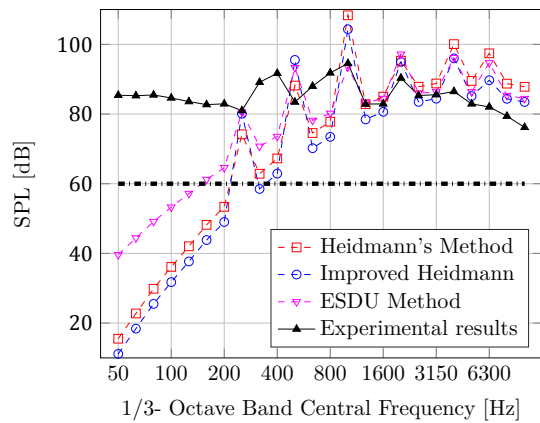
(b) Exhaust, measured at 90°



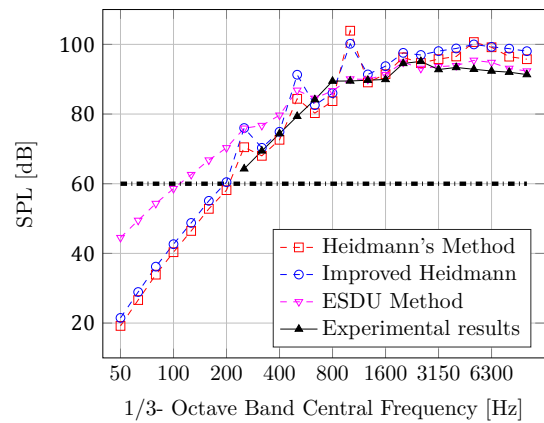
(c) Inlet, measured at 50°



(d) Exhaust, measured at 120°



(e) Inlet, measured at 80°



(f) Exhaust, measured at 150°

Figure 6.11: Fan inlet and exhaust noise spectral comparison of different noise prediction methods for a range of directivity angles measured from engine inlet axis at a 150 ft (45.27 m) radius.

The fly-over procedure is validated using the CFM56-7B engine certification measurement data [13, 105]. The computed equivalent perceived noise level (EPNL) values for the fly-over and lateral noise measurement points, as described in section 5.5, are shown in figures 6.12 and 6.13 respectively.

From figure 6.12 it can be seen that for the fly-over measurement, the equivalent perceived noise level is accurately predicted by the ESDU method. The other two methods over-predict the EPNL. This trend is expected as the flyover simulation is highly dependent on the inlet radiated noise levels. Since both Heidmann's and improved Heidmann's method over-predicted the noise spectrum levels, the results as shown here for the fly-over are as expected. However, from figure 6.13 it can be seen that for the lateral noise measurement point, Heidmann's and the improved Heidmann's method seem to predict the value most accurate, while the ESDU method predicts a lower value of 86.1 dB.

It is concluded that the fly-over simulation gives a reasonable approximation of the equivalent perceived noise levels as perceived by an observer on the ground. For the computation of the EPNL, the ESDU method will be used for flyover simulations, and Heidmann's method for the computation of the lateral noise measurement.

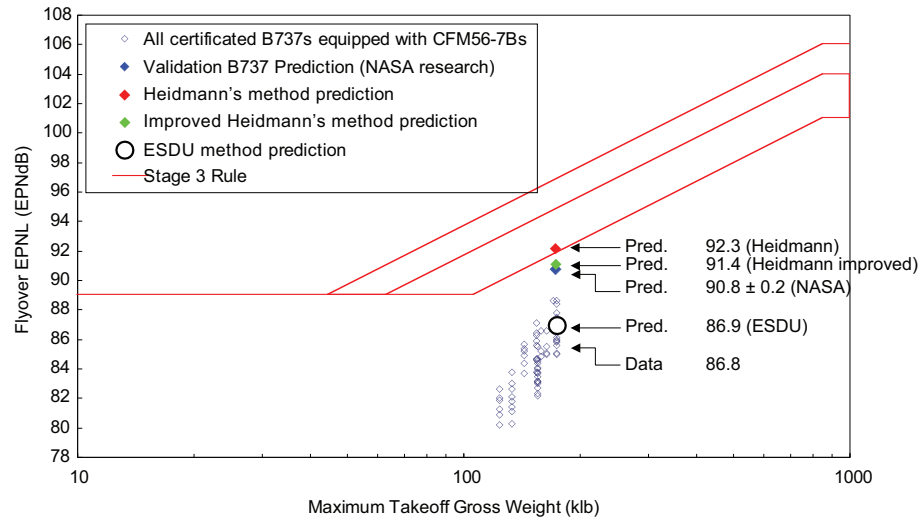


Figure 6.12: Take-off fly-over simulation vs. certified engine data. *Source:* [13]

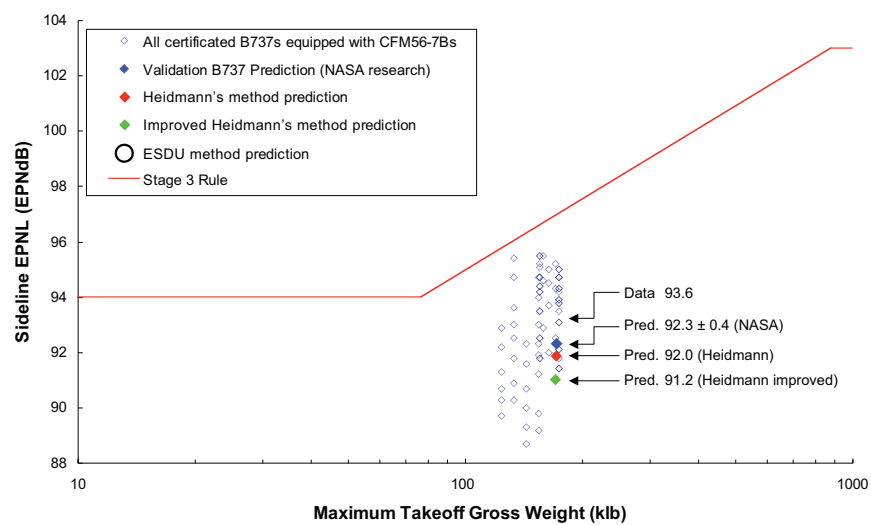


Figure 6.13: Take-off lateral simulation vs. certified engine data. *Source:* [13]

7

Results & Conclusions

Now all separate modules are validated, this chapter will further demonstrate the capabilities of the design tool by testing the effects of increasing tip diameter and varying spool speeds for a range of bypass ratios. First, the effects of increasing fan tip diameter are presented in section 7.1. Then the effect of spool speed is treated in section 7.2. At the end section 7.2, the effect of bypass ratio on the engine size is also shortly demonstrated. Finally, in chapter 8 recommendations with respect to future research are stated.

7.1. Effect of increasing fan tip diameter

The effect of increasing fan tip diameter is tested using the engine conceptual design tool. During the analysis, the inlet conditions are fixed and defined at the fan rotor leading edge. The fan tip speed is kept constant to avoid high losses and keep noise levels within bounds.

In this analysis, the fan is optimized for maximum rotor efficiency while respecting the design constraints, hence the camber angle should be positive and the DeHaller number greater than 0.72 over the entire span of the blade. After the optimised rotor geometry is found, the LPC is designed, all component weights are calculated and finally the noise performance in EPNL is calculated by performing a fly-over simulation. The results of the rotor aerodynamic performance is shown in figure 7.1, the effect on the total engine weight is shown in figure 7.2 and finally the effects on the engine noise are shown in figure 7.3 and 7.4.

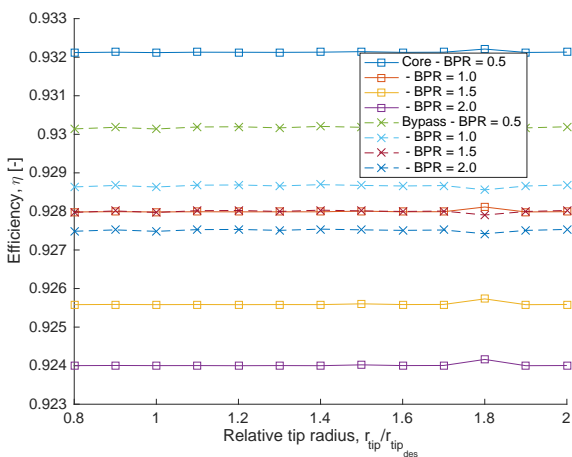


Figure 7.1: Rotor adiabatic performance

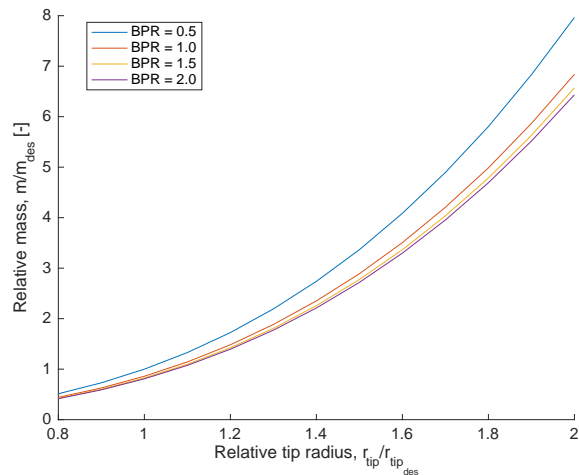


Figure 7.2: Relative total engine weight

Although the fan rotor has successfully optimized for each case, the rotor efficiency remains constant for all tip diameters. This is the result of fixing the tip Mach number and hub-to-tip ratio at the leading edge of the rotor. The fixed Mach number limits the rotational velocity, while the fixed hub-to-tip radius

ratio only scales the fan dimension. Constant axial velocity distribution at the face inlet, this results in a identical velocity distribution for each case. Hence, the rotor efficiency optimization converges to the same optimized solution. To obtain more meaningful results, the analysis is extended to include a range of bypass ratios for each tip diameter that is tested.

The trend of increased total engine weight is obvious for the increased tip diameter. A larger fan tip diameter requires an increase in fan casing diameter as well, which increases the total engine weight very quickly.

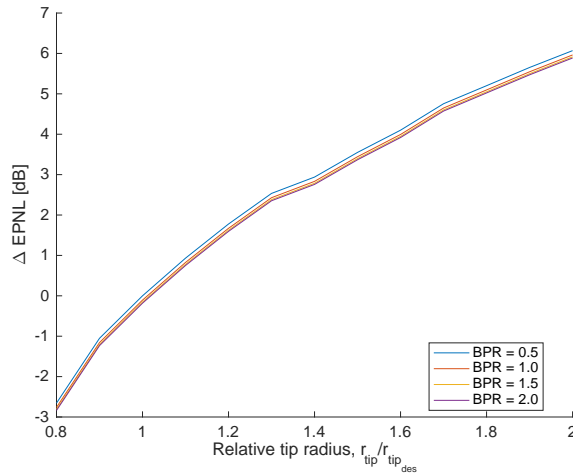


Figure 7.3: Tip diameter effect on the fly-over lateral measurement EPNL.

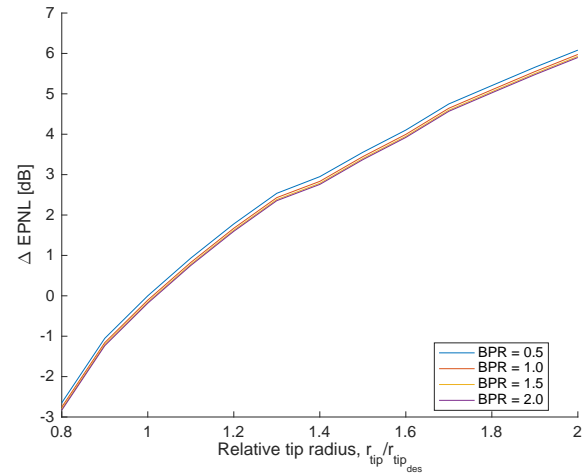


Figure 7.4: Tip diameter effect on the fly-over longitudinal measurement EPNL.

From figures 7.3 and 7.4 a trend of increasing fan engine noise can be observed with the larger tip diameter. This behaviour can be explained using the general equation for the normalized sound pressure level in equation (5.1). The fan noise spectrum is mainly dependent on the mass flow rate and temperature increase over the fan rotor. Since the distribution of temperature ratio will be approximately the same for all rotors with equal tip speed and the mass flow increases quadratically with tip radius, the fan noise will increase with tip diameter. Since the correction factors that are applied in the noise module are all functions of fixed design variables, they do not cause any variation in the sound pressure level.

It can be concluded that increasing the fan tip diameter while fixing the fan tip Mach number effectively scales the engine.

7.2. Effect of spool speed

The effect of spool speed on the performance of the fan and low-pressure compressor module is also investigated here. The spool speed is varied between 0.75 and 1.25 times the design spool speed of the CFM56-7B engine at take-off conditions. It should be noted that during the optimization process of this case, the DeHaller limit is decreased to 0.6 and the tip diameter and the inlet flow characteristics are kept constant in this design case. The results mainly focus on the overall performance of the fan and LPC stages combined. The calculation are performed for a range of BPR's to show the effect of bypass ratio. At the end of this section, one separate case is taken to inspect the effect of bypass ratio.

Merely a small selection of the output generated by the design tool is shown here to demonstrate the tool's capabilities. Following the structure of the report, first the aerodynamic performance is addressed. The effect of varying spool speed on the core and bypass stream efficiency for a range of bypass ratios is shown in figure 7.5. It should be noted that a filled marker corresponds to a change in the number of LPC stages, which holds for all figures.

From figure 7.5, a general trend of constant efficiency up to the design spool speed, and decreasing efficiency at higher spool speeds is observed for both the core and the bypass stream. Most noticeable is the steep decrease in efficiency for the bypass stream at the higher spool speeds. These effects are resulting from the fact that the fan tip diameter is fixed, and hence the relative airspeeds over the fan blade increase. Although the fan rotor is optimized for these new conditions, local super velocities may occur over the suction side of the fan blade, increasing the pressure losses in the cascade. The steep

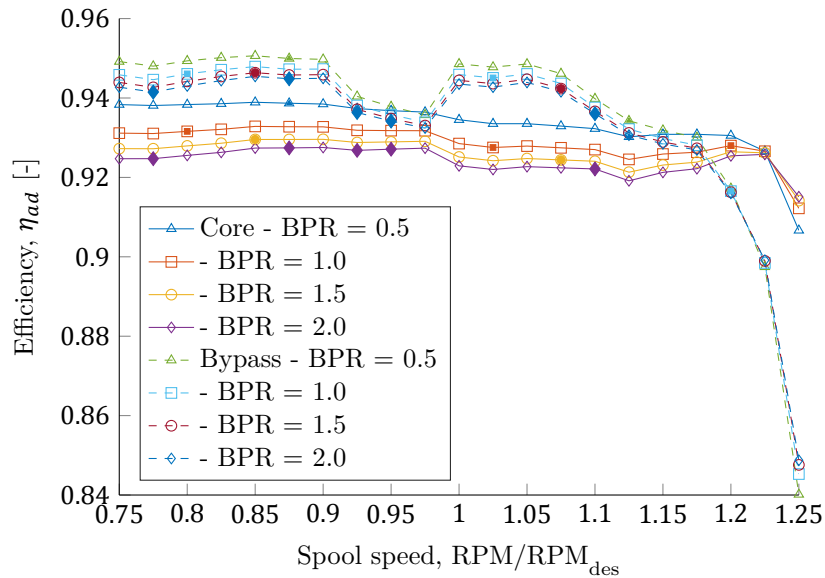


Figure 7.5: The effect of spool speed on the bypass and core adiabatic efficiency η_{ad} for a range of bypass ratios.

decrease in efficiency at higher spool speed is resulting from the increasing area of the fan blade that is operating in the sonic regime, and hence experiences increased shock losses.

The effects of spool speed on the total mass of the entire module is shown in figure 7.8, again for a range of bypass ratios.

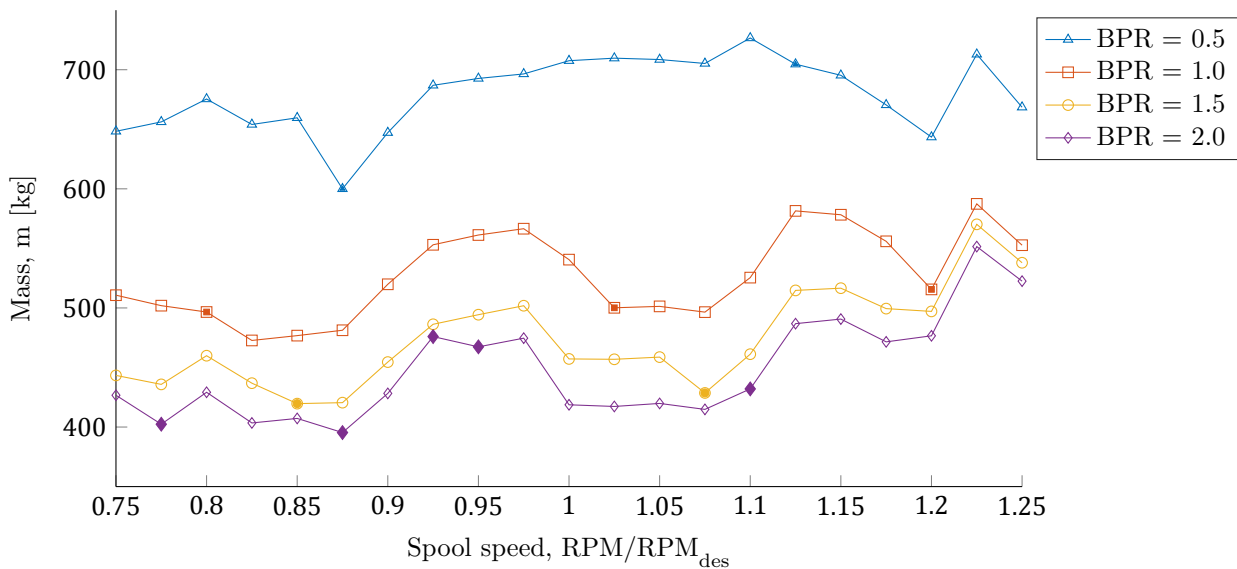


Figure 7.6: Effect of spool speed on total mass m_{tot} for a range of bypass ratios.

Figure 7.8b shows a gradual increase of the compressor weight until the point where a stage can be removed. The LPC mass then drops, and again starts gradually increasing with spool speed over the next few iterations. This increase of the LPC mass is caused by the increasing centrifugal loads for higher spool speeds. Therefore, the LPC rotor disks increase in size to cope with the higher stresses, which increases the LPC component mass.

For the design bypass ratio case, the component weight break-down is given by figure 7.7. From figures 7.8a and 7.8d it can be seen that the fan weight is not strictly dependent on the total fan length. In the lower range of spool speeds the fan length does seem to have some effect. In the higher spool speed region, the fan mass increases due to the increased size of the blade containment casing, which

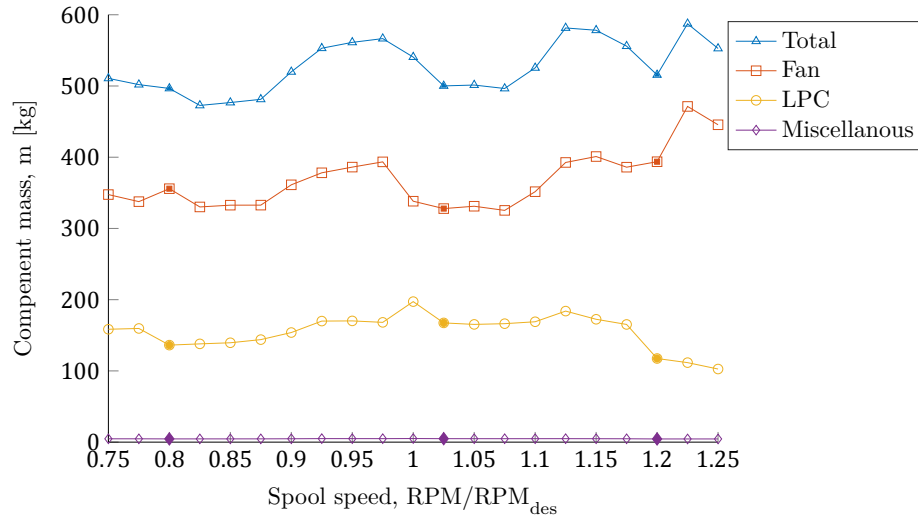
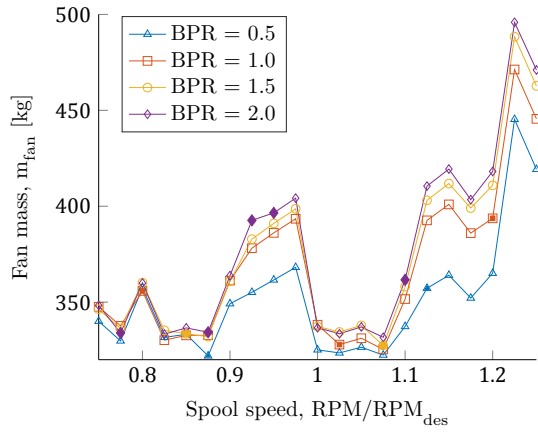
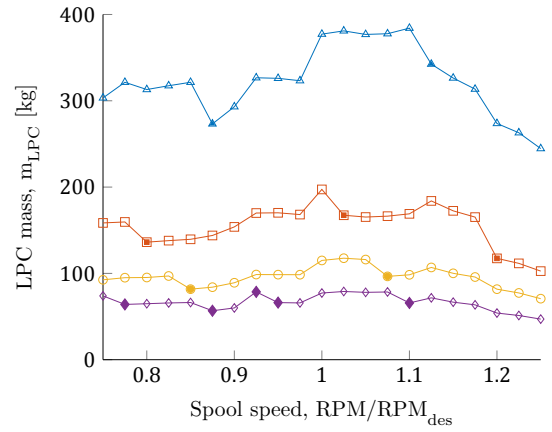


Figure 7.7: Component mass break-down for varying spool speed at design BPR.

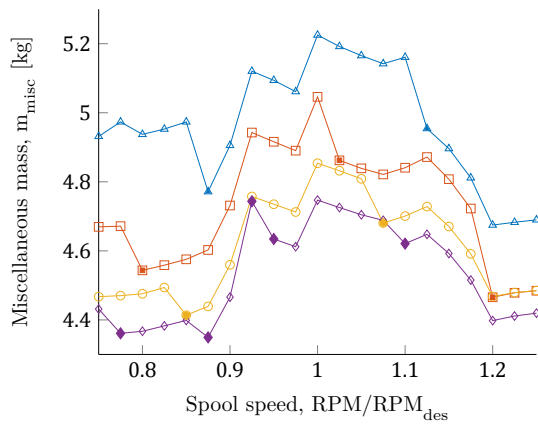
takes up a large part of the total fan mass.



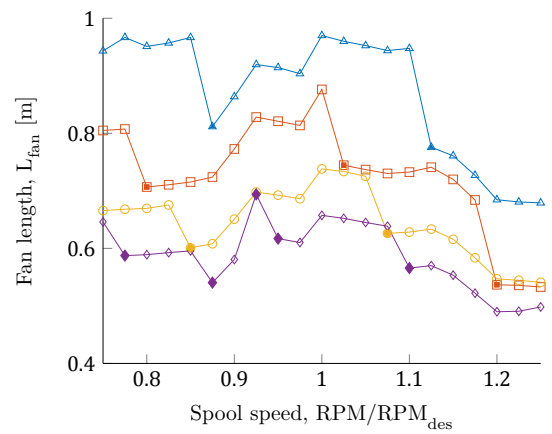
(a) Fan stage mass



(b) Low-pressure compressor mass



(c) Miscellaneous component mass



(d) Total fan length

Figure 7.8: Effect of spool speed on the aerodynamic efficiency and component mass.

Finally, from the results obtained above, a test case is selected to demonstrate the effect of bypass

ratio on the flow path geometry. In figure 7.6, the spacing between the bypass ratio lines at the design spool speed seems to give a good representation of the average bypass effect. Therefore, the design spool speed is taken as case study for bypass ratio effect. Figure 7.9 shows the resulting flow path geometry for the four bypass ratios considered.

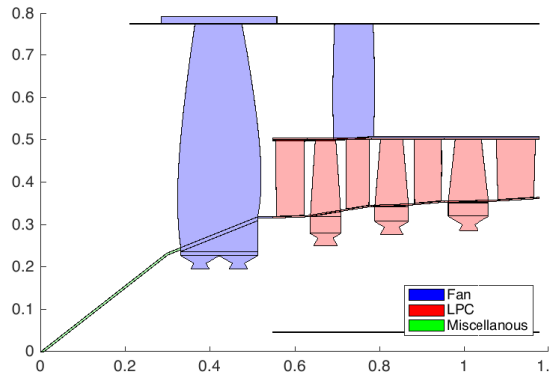
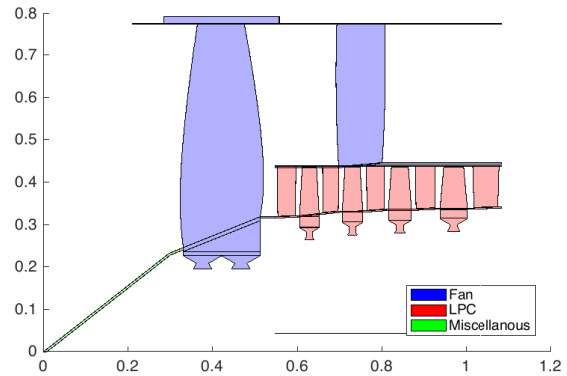
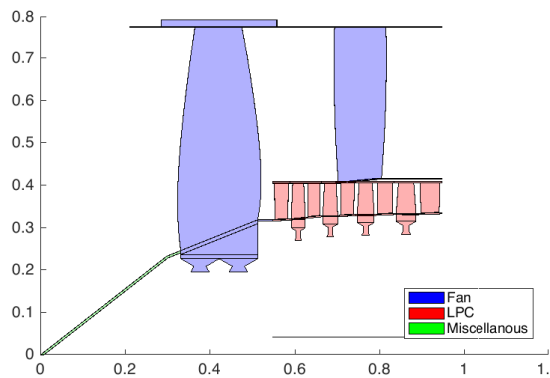
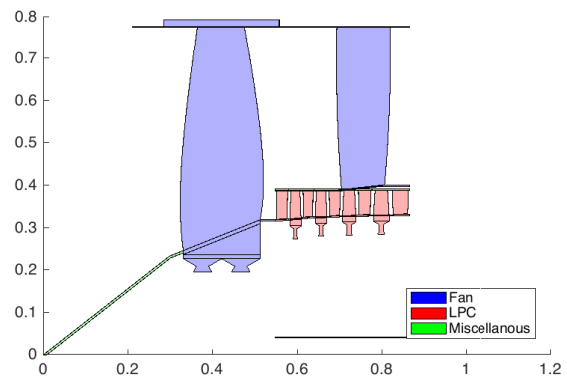
(a) Flowpath geometry at $BPR = 0.5$ (b) Flowpath geometry at $BPR = 1.0$ (c) Flowpath geometry at $BPR = 1.5$ (d) Flowpath geometry at $BPR = 2.0$

Figure 7.9: Effect of bypass ratio on the flow path geometry and component mass sizes at design spool speed.

As can be seen in figure 7.9a, the total fan length increases with lower bypass ratios. Although fewer LPC stages are required to achieve the desired total core pressure ratio, the LPC stage total length has increased since the blades are larger. Furthermore, the fan casing is extended at least up to the end of the compressor, since the weight carrying structure is located behind the rotative part of the LPC. This explains the trend of increasing fan length as seen in figure 7.8d.

To conclude, the increasing tip diameter effectively scales the engine, while the spool speed increases engine mass and decreases efficiency. The design and sizing tool can be applied to many design cases. The results shown here are just an example of the total output of the tool. More in-depth information on the separate components is also available from the output, but is not considered here.



Recommendations

In this chapter the points of improvement to the current work are treated, and areas that need further research are indicated. First some general recommendations regarding future work on this thesis topic are stated. Thereafter, recommendations are presented consistent to the structure of the report and code, and hence are treated per module.

In general, the ultimate goal of the thesis subject is arriving at a complete conceptual engine design and sizing tool. Several conceptual engine design and sizing thesis topics have been completed over the year, such as the conceptual study of contra rotating fans by Díez [5], and Boorsma's [19] work on the conceptual design of aeroengine gas generators, and this thesis on the conceptual design and sizing of the fan and low-pressure compressor. Design tools for the low pressure turbine and miscellaneous parts, such as interconnecting ducts between separate components and weight carrying structures, are still to be developed. To arrive at one single engine design and sizing tool, these separate tools should ultimately be combined.

Since the number of design variables in the engine design process is quite large and proper sharing of information between modules in the process is critical, the total engine design tool needs to be well structured. To ensure integration of the separate design tools is possible in the end, a recommendation would be to dedicate one research topic to the development of one proper structured module-based engine design tool. All currently developed design tools should be thoroughly analysed and updated where necessary to comply to the base module format, using one coding style format in the end.

8.1. Aerodynamics module

- In the LPC design module, include falling mean-line design without a fixed hub diameter for more realistic LPC modelling.
- Include a simplified equation of state model. The speed performance of the current high-level integrated `Matlab` interface of the `CoolProp` software is slowing down iterative solving process, due to numerous function calls in the conversion loop. Either the low-level DLL interaction could be used to speed up the calculation process, or the use of simplified equations of state dedicated to air gas property calculations could increase speed.
- Include design of nozzles and fan cowling.

8.2. Structural & analysis module

- More detailed design of fan casing, as it makes up for a large portion of the total engine weight.
- Use ribbed blade containment casing design and include structural analysis of such geometry.
- Include design and sizing of load carrying structure of the engine.
- Include calculations of blade stresses.
- Include basic vibration analysis for blades and disks.

8.3. Noise module

- Revision of the noise module. It was assumed that the noise module was readily available and fully functional. However, validation and application on design cases showed that the noise module shows inaccurate results. Further research is needed to inspect if this is a failure of the code or the wrong implementation here. Quick inspection of the design code however showed several errors, for example not considering the absolute value of the the cut-off correction factor δ , and the absence of some correction factor at the broad-band noise calculation at subsonic relative design tip Mach number. Due to time constraints a full revision of the code was not carried out here, but it is advised to look further into this.
- Vectorize the noise module for increased speed performance. This will prove especially useful when used inside an optimization routine. Since the noise prediction method output is non-linear and contains logical statements, a global optimization routine such as a genetic algorithm or a pattern search should be used for optimization purposes. These methods often have a high number of function evaluations before reaching a global optimum, and therefore speed increase of the code is an important criteria.
- Include other flight simulations such as landing approach and include thrust cut-back profiles.
- Inclusion of atmospheric attenuation effects in the perceived noise level calculations, as mentioned by Díez [5].

A

Loss coefficient correlations

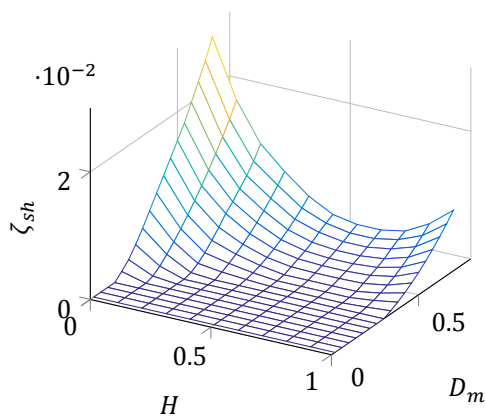


Figure A.1: Shock loss coefficient, ζ_{sh} , as a function of immersion ratio, H , and modified diffusion parameter, D_m .

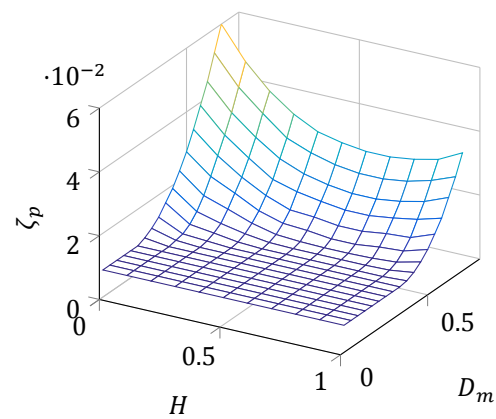


Figure A.2: Profile loss coefficient, ζ_p , as a function of immersion ratio, H , and modified diffusion parameter, D_m .

Bibliography

- [1] IATA, German Aerospace Center (DLR), and Georgia Institute of Technology, *IATA Technology Roadmap 2013*, (2013).
- [2] General Electric, *CF6-80C2 Airflows FADEC Control - Information poster C1010-FAD1*, .
- [3] L. R. Jenkinson, J. F. Marchman, L. Jenkinson, and J. Marchman, *Aircraft Design Projects* (Butterworth-Heinemann, 2003) p. 392.
- [4] C. Soares, *Gas Turbines: A Handbook of Air, Land and Sea Applications*, 2nd ed. (Elsevier Inc., Oxford, UK, 2014).
- [5] N. G. Díez and d. A. G. Rao, *Faculty of Aerospace Engineering*, Tech. Rep. (Delft University of Technology, Delft, 2009).
- [6] S. Farokhi, *Aircraft propulsion*, 2nd ed. (Wiley Publishing, Inc., Chichester, U.K., 1971) p. 1048.
- [7] M. Schobeiri, *Turbomachinery Flow Physics and Dynamic Performance* (Springer Berlin Heidelberg, Berlin, Heidelberg, 2005) pp. 1–522.
- [8] N. Falck, *Axial Flow Compressor Mean Line Design*, [Msc thesis](#), Lund University, Sweden (2008).
- [9] Y. Lee, J. Pan, R. Hathaway, and M. Barkey, *Fatigue Testing and Analysis* (Elsevier Inc., Oxford, UK, 2005) p. 417.
- [10] J. Kurzke, *GasTurb Details GasTurb Details 5*, (2007).
- [11] M. T. Tong, I. Halliwell, and L. J. Ghosn, *A Computer Code for Gas Turbine Engine Weight and Disk Life Estimation*, [Journal of Engineering for Gas Turbines and Power](#) **126**, 265 (2004).
- [12] CFM International, *Training Manual CFM56-6B (Basic Engine)*, January (CFM International, Melun Cedex, France, 1998).
- [13] M. D. Dahl, *Overview of Aircraft Noise Prediction Tools Assessment*, Tech. Rep. (NASA, Cleveland, OH, 2007).
- [14] J. Kurzke, *VKI LS 2013-04: Aeroengine design: From state of the art of turbofans towards innovative architectures*, Lecture series / Von Karman Institute for Fluid Dynamics (Karman Institute for Fluid Dynamics, 2013) Chap. 1.
- [15] K. Kyprianidis, *Multi-disciplinary conceptual design of future jet engine systems*, [Ph.D. thesis](#), Cranfield University (2010).
- [16] K. Kyprianidis and A. Dax, *Low pressure system component advancements and its impact on future turbofan engine emissions*, in *Paper No. ISABE-2009- ...*, November 2015 (2009) pp. 1–14.
- [17] E. Roux, *Turbofan and Turbojet Engines: Database Handbook* (Élodie Roux, 2007).
- [18] S. A. Korpela, *Principles of Turbomachinery*, 1st ed. (John Wiley & Sons, Inc., Hoboken, New Jersey, 2011) p. 476.
- [19] M. J. Boorsma and d. A. G. Rao, *Faculty of Aerospace Engineering*, Tech. Rep. (Delft University of Technology, Delft, 2015).
- [20] R. Boyer, G. Welsch, and E. W. Collings, *ASM Materials Properties Handbook: Titanium Alloys* (ASM International, Materials Park, OH, 1994) p. 1176.

- [21] R. L. Dreshfield, *Long Time Creep Rupture of Haynes(TM) Alloy 188*, Tech. Rep. (NASA, Cleveland, Ohio, 1996).
- [22] Airbus GMF, *Global Market Forecast 2015*, (2015).
- [23] ACARE Strategy Review Group, *Aeronautics and Air Transport: Beyond Vision 2020 (Towards 2050)*, Tech. Rep. (Advisory Council for Aeronautics Research in Europe (ACARE), Brussels, 2010).
- [24] High Level Group on Aviation Research, *Flightpath 2050*, (2011).
- [25] Air Transport Action Group, *A sustainable flightpath towards reducing emissions*, (2012).
- [26] T. Obrecht, *Aeroengine Design: From State of the Art of Turbofans Towards Innovative Architectures*, Lecture series / Von Karman Institute for Fluid Dynamics (Karman Institute for Fluid Dynamics, 2013) Chap. 3.
- [27] N. Smith, *Aeroengine Design: From State of the Art of Turbofans Towards Innovative Architectures*, Lecture series / Von Karman Institute for Fluid Dynamics (Karman Institute for Fluid Dynamics, 2013) Chap. 2.
- [28] A. Amato, J. Seitzman, and T. Lieuwen, *Gas Turbine Emissions*, timothy c. ed., edited by T. C. Lieuwen and V. Yang, Vol. 38 (Cambridge University Press, New York, NY, 2013) pp. 209–234.
- [29] R. Dénos and G. Paniagua, *Aeroengine Design: From State of the Art of Turbofans Towards Innovative Architectures*, Lecture series / Von Karman Institute for Fluid Dynamics (Karman Institute for Fluid Dynamics, 2013) Chap. 6.
- [30] R. Dénos and G. Paniagua, *Aeroengine Design: From State of the Art of Turbofans Towards Innovative Architectures*, Lecture series / Von Karman Institute for Fluid Dynamics (Karman Institute for Fluid Dynamics, 2013) Chap. 7.
- [31] J. D. Mattingly, *Aircraft Engine Design*, 2nd ed. (American Institute of Aeronautics and Astronautics, Inc., Reston, VA, 2002).
- [32] R. W. Koenig and L. H. Fishbach, *GENENG — A Program For Calculating Design and Off-Design Performance for Turbojet and Turbofan Engines*, Tech. Rep. February (NASA, Washington D.C., 1972).
- [33] L. H. Fishbach and R. W. Koenig, *GENENG II — A Program for Calculating Design and Off-Design Performance of Two- and Three-Spool Turbofans With As Many As Three Nozzles*, Tech. Rep. February (NADA, Washington D.C., 1972).
- [34] W. L. MacMillan and J. Palmer, *Development of a Modular Type Computer Program for the Calculation of Gas Turbine Off Design Performance*, Tech. Rep. (Cranfield Institute of Technology, Cranfield, UK, 1974).
- [35] J. R. Palmer and Y. Cheng-zhong, *TURBOTRANS: a Programming Language for the Performance Simulation of Arbitrary Gas Turbine Engines with Arbitrary Control Systems*, in *ASME 1982 International Gas Turbine Conference and Exhibit*, Vol. 5 (American Society of Mechanical Engineers, London, UK, 1982) p. 8.
- [36] W. P. J. Visser, *Gas Turbine Engine Simulation At NLR*, in *CEAS Symposium on Simulation Technology, "Making it Real"* (Delft, 1995).
- [37] W. P. J. Visser and M. J. Broomhead, *GSP — A Generic Object-Oriented Gas Turbine Simulation Environment*, Tech. Rep. (National Aerospace Laborator (NLR), 2000).
- [38] T. Grönstedt, *Development of Methods for Analysis and Optimization of Complex Jet Engine Systems*, Ph.D. thesis, Chalmers University of Technology (2000).

- [39] U. T. J. Grönstedt and P. Pilidis, *Control Optimization of the Transient Performance of the Selective Bleed Variable Cycle Engine During Mode Transition*, *Journal of Engineering for Gas Turbines and Power* **124**, 75 (2002).
- [40] R. W. Claus, A. L. Evans, J. K. Lytle, and L. D. Nichols, *Numerical Propulsion System Simulation*, *Computing Systems in Engineering* **2**, 357 (1991).
- [41] C. K. Drummond, G. J. Follen, and C. W. Putt, *Gas Turbine System Simulation: An Object-Oriented Approach*, Tech. Rep. (National Aeronautics and Space Administration (NASA), Cleveland, Ohio, 1992).
- [42] J. K. Lytle, *The Numerical Propulsion System Simulation: An Overview*, *CAS 2000 Workshop/The Ames Research Center* (2000).
- [43] A. Alexiou, E. H. Baalbergen, O. Kogenhop, K. Mathioudakis, and P. Arendsen, *Advanced Capabilities for Gas Turbine Engine Performance Simulations*, in *Volume 1: Turbo Expo 2007* (ASME, 2007) pp. 19–28.
- [44] A. Bala, V. Sethi, E. L. Gatto, V. Pachidis, and P. Pilidis, *PROOSIS – A Collaborative Venture for Gas Turbine Performance Simulation using an Object Oriented Programming Schema*, Power (2007).
- [45] P. Lolis, *Development of a Preliminary Weight Estimation Method for Advanced Turbofan Engines*, Phd, Cranfield University (2014).
- [46] D. a. Sagerser, S. Lieblein, R. P. Kkebs, N. Aeronautics, and T. Memorandum, *Emperical Expressions for Estimating Length and Weight of Axial-Flow Components of VTOL Powerplants*, Tech. Rep. (NASA, Washington D.C., 1971).
- [47] R. Pera, E. Onat, G. Klees, and E. Tjonneland, *A Method to Estimate Weight and Dimensions of Aircraft Gas Turbine Engines. Volume 1: Method of Analysis*, Tech. Rep. (NASA, Seattle, WA, 1977).
- [48] G. W. Klees and L. H. Fishbach, *Aircraft Engine Weight Estimation Method*, in *37th Annual Conference, Munich, West Germany, May 8-10*, Society of Allied Weight Engineers, Inc. (Society of Allied Weight Engineers, Inc., Munich, West Germany, 1978) p. 28.
- [49] E. Onat and G. Klees, *A Method to Estimate Weight and Dimensions of Large and Small Gas Turbine Engines*, Tech. Rep. (NASA, Seattle, WA, 1979).
- [50] P. L. Hale, *A Method to Estimate Weight and Dimensions of Small Aircraft Propulsion Gas Turbine Engines*, Tech. Rep. (NASA, Phoenix, Arizona, 1982).
- [51] V. Sanghi, S. K. Kumar, S. K. Sane, and V. Sundararajan, *Preliminary Estimation of Engine Gas-Flow-Path Size and Weight*, *Journal of Propulsion and Power* **14**, 208 (1998).
- [52] M. T. Tong and B. a. Naylor, *An Object-Oriented Computer Code for Aircraft Engine Weight Estimation, Volume 1: Aircraft Engine; Ceramics; Coal, Biomass and Alternative Fuels; Manufacturing, Materials and Metallurgy; Microturbines and Small Turbomachinery*, 1 (2008).
- [53] S. Bretschneider, O. Arago, and S. Staudacher, *Architecture of a Techno and Environmental Risk Assessment Tool Using a Multi-Modular Build Approach*, in *ISABE 2007 Proceedings* (2007) p. 1103.
- [54] M. F. Heidmann, *Interim Prediction Method for Fan and Compressor Source Noise*, *NASA Scientific and Technical Information Branch* (1979).
- [55] K. B. Kontos, R. E. Kraft, and P. R. Gliebe, *Improved NASA-ANOPP Noise Prediction Computer Code for Advanced Subsonic Propulsion Systems*, Tech. Rep. 24 (NASA, Cincinnati, Ohio, 1996).
- [56] J. R. Stone, E. A. Krejsa, and B. J. Clark, *Jet Noise Modeling for Coannular Nozzles Including the Effects of Chevrons*, National Aeronautics and Space Administration (2003).

- [57] Society of Automotive Engineers, *Gas Turbine Jet Exhaust Noise Prediction*, Aerospace recommended practice (Society of Automotive Engineering, 1994) p. 114.
- [58] E. A. Krejsa and M. F. Valerino, *Interim Prediction Method for Turbine Noise*, Tech. Rep. (NASA, Cleveland, Ohio, 1976).
- [59] M. Fink, *Airframe Noise Prediction Method*, Tech. Rep. (U.S. Department of Transportation, Washington D.C., 1977).
- [60] SAE. Comitee A-21, Aircraft Noise., *Standard values of atmospheric absorption as a function of temperature and humidity*, Tech. Rep. (Society of Automotive Engineers, 1975).
- [61] C. Chien and W. Soroka, *Sound propagation along an impedance plane*, *Journal of Sound and Vibration* **43**, 9 (1975).
- [62] SAE – Comitee A-21, Aircraft Noise., *Prediction Method of Lateral Attenuation of Airplane Noise During Takeoff and Landing*, Tech. Rep. (Society of Automotive Engineers, 1981).
- [63] A. Blackner and T. Bhat, *Installation effects on coaxial jet noise - An experimental study*, in *36th AIAA Aerospace Sciences Meeting and Exhibit*, Vol. 53 (American Institute of Aeronautics and Astronautics, Reston, Virginia, 1998) pp. 1–36, [arXiv:arXiv:1011.1669v3](https://arxiv.org/abs/1011.1669v3) .
- [64] D. B. Hanson, *Noise of counter-rotation propellers*, *Journal of Aircraft* **22**, 609 (1985).
- [65] C. E. Whitfield, R. Mani, and P. R. Glibe, *High Speed Turboprop Aeroacoustic Study (Counter-rotation) Volume I - Model Development*, Tech. Rep. (NASA, Cincinnati, Ohio, 1992).
- [66] S. Dixon and C. Hall, *Fluid Mechanics and Thermodynamics of Turbomachinery*, 7th ed. (Elsevier Inc., Oxford, UK, 1995) p. 536.
- [67] J.-M. Tournier and M. S. El-Genk, *Axial flow, multi-stage turbine and compressor models*, *Energy Conversion and Management* **51**, 16 (2010).
- [68] L. Reid and R. D. Moore, *Performance of Single-Stage Axial-Flow Transonic Compressor With Rotor and Stator Aspect Ratios of 1.19 and 1.26, Respectively, and With Design Pressure Ratio of 1.82*, Tech. Rep. November 1978 (NASA, Cleveland, OH, 1978).
- [69] R. D. Moore and L. Reid, *Performance of Single-Stage Axial-Flow Transonic Compressor with Rotor and Stator Aspect Ratios of 1.63 and 1.78, Respectively, and with Design Pressure Ratio of 1.82*, Tech. Rep. (NASA, Cleveland, OH, 1982).
- [70] R. D. Moore and L. Reid, *Performance of Single-Stage Axial-Flow Transonic Compressor With Rotor and Stator Aspect Ratios of 1.19 and 1.26, Respectively, and With Design Pressure Ratio of 2.05*, Tech. Rep. (NASA, Cleveland, OH, 1980).
- [71] W. M. Osborn and R. J. Steinke, *Performance of a 1.15-Pressure-Ratio Axial-Flow Fan Stage with a Blade Tip Solidity of 0.5*, Tech. Rep. (NASA, Cleveland, OH, 1974).
- [72] R. D. Moore and R. J. Steinke, *Aerodynamic Performance of a 1.25-Pressure-Ratio Axial-Flow Fan Stage*, Tech. Rep. (NASA, Cleveland, OH, 1974).
- [73] W. M. Osborn, R. D. Moore, and R. J. Steinke, *Aerodynamic Performance of a 1.35-Pressure-Ratio Axial-Flow Fan Stage*, Tech. Rep. (NASA, Cleveland, OH, 1978).
- [74] G. W. Lewis, R. D. Moore, and G. Kovich, *Performance of a 1.20-Pressure-Ratio STOL Fan Stage at Three Rotor Blade Setting Angles*, Tech. Rep. NASA TM X-2837 (NASA, 1973).
- [75] R. D. Moore and W. M. Osborn, *Aerodynamic Performance of 1.38-Pressure-Ratio, Variable-Pitch Fan Stage*, Tech. Rep. (NASA, Cleveland, OH, 1979).
- [76] D. C. Urasek, W. T. Gorrell, and W. S. Cunnann, *Performance of Two-Stage Fan Having Low-Aspect Ratio, First-Stage Rotor Blading*, Tech. Rep. (NASA, Cleveland, OH, 1979).

- [77] R. H. Aungier, *Axial-Flow Compressors* (ASME Press, New York, NY, 2003) p. 368.
- [78] A. R. Howell, *Fluid dynamics of axial compressors*, [ARCHIVE: Proceedings of the Institution of Mechanical Engineers 1847-1982 \(vols 1-196\)](#) **153**, 441 (1945).
- [79] I. Johnsen and R. Bullock, *Aerodynamic Design Of Axial-Flow Compressors* (NASA Lewis Research Center, Cleveland, Ohio, 1965).
- [80] S. Lieblein, F. Schwenk, and R. Broderick, *Diffusion factor for estimating losses and limiting blade loadings in axial-flow-compressor blade elements*, [NACA Research Memorandum](#) , **1** (1953).
- [81] M. T. Schobeiri, *Advanced Compressor Loss Correlations, Part II: Experimental Verifications*, [Int. J. Rotating Machinery](#) **3**, 179 (1997).
- [82] M. T. Schobeiri, *Advanced Compressor Loss Correlations, Part I: Theoretical Aspects*, [Int. J. Rotating Machinery](#) **3**, 179 (1997).
- [83] W. Jansen and W. C. Moffatt, *The Off-Design Analysis of Axial-Flow Compressors*, [Journal of Engineering for Gas Turbines and Power](#) **89**, 453 (1967).
- [84] M. Davis, *A stage-by-stage dual-spool compression system modeling technique*, [ASME International Gas Turbine Conference and Exhibi](#) , **1** (1982).
- [85] W. R. Davis, *A computer program for the analysis and design of turbomachinery – Revision*, Tech. Rep. (Division of Aerothermodynamics, Carleton University, Ottawa, Canada, 1971).
- [86] W. C. Swan, *A Practical Method of Predicting Transonic-Compressor Performance*, [Journal of Engineering for Power](#) **83**, 322 (1961).
- [87] L. Aleid, *Variable cycle propulsion systems for a supersonic civil transport*, , 275 (1997).
- [88] S. Lieblein, *Loss and Stall Analysis in Compressor Cascades*, [Journal of Basic Eng.](#) **81**, 387 (1959).
- [89] C. C. Koch and L. H. Smith, *Loss Sources and Magnitudes in Axial-Flow Compressors*, [Journal of Engineering for Power](#) **98**, 411 (1976).
- [90] R. H. Aungier, *Turbine Aerodynamics: Axial-Flow and Radial-Flow Turbine Design and Analysis* (ASME Press, New York, NY, 2005) p. 404.
- [91] M. I. Yaras and S. a. Sjolander, *Prediction of Tip-Leakage Losses in Axial Turbines*, [Journal of Turbomachinery](#) **114**, 204 (1992).
- [92] F. G. Pascual and W. Q. Meeker, *Estimating Fatigue Curves With the Random Fatigue-Limit Model*, [Technometrics](#) **41**, 277 (1999).
- [93] S. C. Armand, *Structural Optimization Methodology for Rotating Disks of Aircraft Engines*, Tech. Rep. November (NASA, Washington D.C., 1995).
- [94] D. Gutzwiller, *T-Axi Disk V2.2 User ' s Guide and Tutorial*, [Ewp.Rpi.Edu](#) , **1** (2009).
- [95] D. P. Gutzwiller and M. G. Turner, *Rapid low fidelity turbomachinery disk optimization*, [Advances in Engineering Software](#) **41**, 779 (2010).
- [96] M. C. Potter, J. L. Goldberg, and E. Aboufadel, *Advanced Engineering Mathematics*, 3rd ed. (Oxford University Press, 2005).
- [97] A. Mendelson and S. Manson, *Practical Solution of Plastic Deformation Problems in Elastic-Plastic Range*, Tech. Rep. (NASA, Cleveland, Ohio, 1957).
- [98] S. Bretschneider, F. Rothe, M. G. Rose, and S. Staudacher, *Compressor Casing Preliminary Design Based on Features*, in [Volume 5: Structures and Dynamics, Parts A and B](#) (ASME, 2008) pp. 1–9.
- [99] A. Carman, *Resistance of Tubes to Collapse*, [University of Illinois Bulletin](#) **3** (1906).

-
- [100] T. B. Dewhurst, *The Impact Load on Containment Rings During a Multiple Blade Shed in Aircraft Gas Turbine Engines*, [International Gas Turbine and Aeroengine Congress and Exposition \(1991\)](#), [10.1115/91-GT-163](#).
- [101] ESDU, *Prediction of Noise Generated by Fans and Compressors in Turbojet and Turbofan Engines* (ESDU International PLC, London, UK, 1998).
- [102] M. F. Heidmann and C. E. Feiler, *Noise comparisons from full-scale fan tests at NASA Lewis Research Center*, Tech. Rep. (NASA Lewis Research Center, Cleveland, OH, 1973).
- [103] Boeing Commercial Airplanes, *Boeing 767 Airplane Characteristics for Airport Planning*, Tech. Rep. (2005).
- [104] Federal Aviation Administration, *Noise Certification Standards for Subsonic Jet Airplanes and Subsonic Transport Category Large Airplanes*, Federal Register **65**, 1 (2000).
- [105] Federal Aviation Administration, *Estimated Airplane Noise Levels in A-Weighted Decibels*, Tech. Rep. January (U.S. Department of Transportation, 2012).